PHYSICAL REVIEW B **95**, 094422 (2017)

Theory of multiple-phase competition in pyrochlore magnets with anisotropic exchange with application to $Yb_2Ti_2O_7$, $Er_2Ti_2O_7$, and $Er_2Sn_2O_7$

Han Yan,[1,2] Owen Benton,[1,3] Ludovic Jaubert,[1,4] and Nic Shannon[1,2,3]
[1]*Okinawa Institute of Science and Technology Graduate University, Onna-son, Okinawa 904-0395, Japan*
[2]*Clarendon Laboratory, University of Oxford, Parks Rd., Oxford OX1 3PU, United Kingdom*
[3]*H. H. Wills Physics Laboratory, University of Bristol, Tyndall Av, Bristol BS8–1TL, United Kingdom*
[4]*Rudolf Peierls Centre for Theoretical Physics, University of Oxford, 1–6 Keeble Rd, Oxford OX1 3NP, United Kingdom*

(Received 20 December 2013; revised manuscript received 21 February 2017; published 17 March 2017)

The family of magnetic rare-earth pyrochlore oxides $R_2M_2O_7$ plays host to a diverse array of exotic phenomena, driven by the interplay between geometrical frustration and spin-orbit interaction, which leads to anisotropy in both magnetic moments and their interactions. In this article we establish a general, symmetry-based theory of pyrochlore magnets with anisotropic exchange interactions. Starting from a very general model of nearest-neighbor exchange between Kramers ions, we find four distinct classical ordered states, all with $\mathbf{q} = 0$, competing with a variety of spin liquids and unconventional forms of magnetic order. The finite-temperature phase diagram of this model is determined by Monte Carlo simulation, supported by classical spin-wave calculations. We pay particular attention to the region of parameter space relevant to the widely studied materials $Er_2Ti_2O_7$, $Yb_2Ti_2O_7$, and $Er_2Sn_2O_7$. We find that many of the most interesting properties of these materials can be traced back to the "accidental" degeneracies where phases with different symmetries meet. These include the ordered ground-state selection by fluctuations in $Er_2Ti_2O_7$, the dimensional reduction observed in $Yb_2Ti_2O_7$, and the lack of reported magnetic order in $Er_2Sn_2O_7$. We also discuss the application of this theory to other pyrochlore oxides.

DOI: 10.1103/PhysRevB.95.094422

I. INTRODUCTION

Like high-energy physics, condensed matter is dominated by the idea of symmetry. Any physical property which *cannot* be traced back to a broken symmetry is therefore of enormous fundamental interest. In this context, the spin-liquid phases found in frustrated magnets are a rich source of inspiration [1]. Perhaps the most widely studied examples are the "spin-ice" states in $Ho_2Ti_2O_7$ and $Dy_2Ti_2O_7$, classical spin liquids famous for their magnetic monopole excitations [2]. And there is now good reason to believe that a *quantum* spin-liquid phase, in which the magnetic monopoles are elevated to the role of "elementary" particles, could exist in spin-ice-like materials where quantum effects play a larger role [3–14].

The extraordinary physics of spin ice stems from the combination of the geometrical frustration inherent to the pyrochlore lattice on which the magnetic rare earth ions R^{3+} reside, and the strongly anisotropic nature of the interactions between rare-earth ions [15,16]. This mixture of geometrical frustration and strong spin anisotropy is common to many pyrochlore materials, and gives rise to a wide array of interesting physical behaviors [17].

The spin ices belong to a wider family of rare-earth pyrochlore oxides $R_2M_2O_7$ in which the magnetic ions have a doublet ground state, and highly anisotropic interactions. The physical properties of these materials depend on the choice of rare-earth R^{3+} and transition metal M^{4+}, and are fabulously diverse. In addition to spin ices, this family includes a wide range of systems that order magnetically, spin glasses and systems where local moments couple to itinerant electrons [17–19]. Materials of current interest include $Yb_2Ti_2O_7$, which exhibits striking "rodlike" features in neutron scattering [20–23], and has been argued to undergo a Higgs transition into a ferromagmetically ordered state [24]; $Er_2Ti_2O_7$, which appears to offer an elegant worked example of (quantum) order-by-disorder [25–29]; and $Er_2Sn_2O_7$, which has yet to been seen to order at *any* temperature [30–34]. Alongside continuing investigations into these materials, the last few years has seen the synthesis of a steady stream of new rare-earth pyrochlore oxides, exhibiting both ordered [35–39] and disordered [40] low temperature states.

Given this "embarrassment of riches," it seems reasonable to ask whether there is *any* common framework which can connect the properties of different rare-earth pyrochlore oxides, place new materials in context, and help guide the search for novel magnetic states. In this article we enlarge on the results in an earlier preprint [41] to develop a broad scenario for these materials, based on the concept of multiple-phase competition. We go on to show how this approach can be used to explain many of the interesting properties of $Yb_2Ti_2O_7$, $Er_2Ti_2O_7$, and $Er_2Sn_2O_7$.

Our starting point is the most general model of nearest-neighbor interactions compatible with the symmetries of the pyrochlore lattice [42–44]

$$\mathcal{H}_{\text{ex}} = \sum_{\langle ij \rangle} J_{ij}^{\mu\nu} S_i^{\mu} S_j^{\nu}, \qquad (1)$$

where the sum on $\langle ij \rangle$ runs over the nearest-neighbor bonds of the pyrochlore lattice, $\mathbf{S}_i = (S_i^x, S_i^y, S_i^z)$ describes the magnetic moment of the rare-earth ion, and the matrix $J_{ij}^{\mu\nu}$ is a function of four independent parameters. Following the notation of Ross *et al.* [44], we identify these as "X-Y" (J_1), "Ising" (J_2), "symmetric off-diagonal" (J_3), and "Dzyaloshinskii-Moriya" (J_4) interactions. This model encompasses an extremely rich variety of different magnetic physics, including an exchange-based "spin ice" ($J_1 = -J_2 = J_3 = J_4 < 0$), and the Heisenberg antiferromagnet on a pyrochlore lattice ($J_1 = J_2 > 0$, $J_3 = J_4 = 0$), both of which are believed to have spin-liquid ground states [15,45]. Nonetheless, materials such

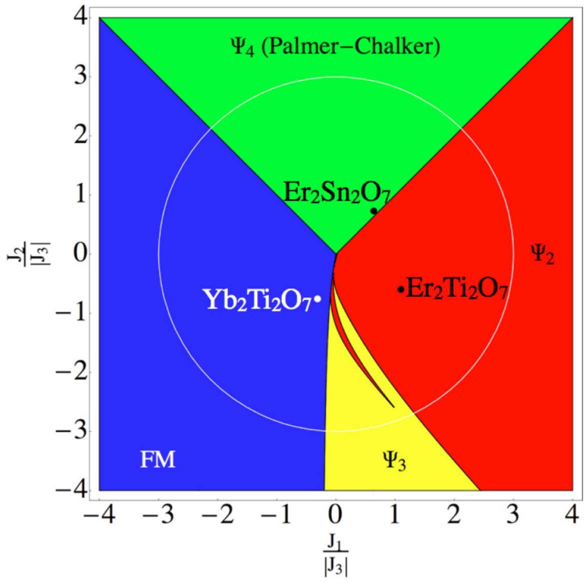

FIG. 1. Classical ground-state phase diagram for a pyrochlore magnet with anisotropic exchange interactions. The model considered is the most general nearest-neighbor exchange Hamiltonian on the pyrochlore lattice $\mathcal{H}_{\rm ex}$ [Eq. (1)], with symmetric off-diagonal exchange $J_3 < 0$, and vanishing Dzyaloshinskii-Moriya interactions ($J_4 = 0$). There are four distinct ordered phases, illustrated in the insets of Fig. 3. Points correspond to published estimates of parameters for $Yb_2Ti_2O_7$ [44], $Er_2Ti_2O_7$ [26], and $Er_2Sn_2O_7$ [34], setting $J_4 = 0$. The white circle corresponds to the path through parameter space shown in Fig. 3.

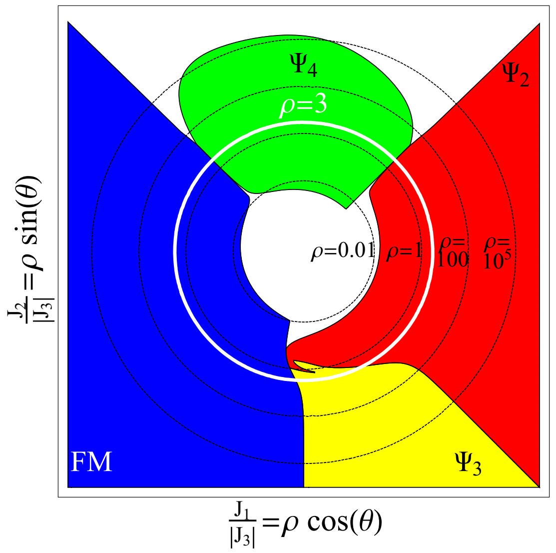

FIG. 2. Suppression of classical order by quantum fluctuations in pyrochlore magnets with anisotropic exchange interactions, as described by $\mathcal{H}_{\rm ex}$ [Eq. (1)], with $J_3 < 0$, $J_4 = 0$. Colored regions show the four ordered phases illustrated in Fig. 3. White regions indicate where quantum fluctuations eliminate conventional magnetic order, within a linear spin-wave theory. Parameters $J_1/|J_3| = \rho\cos\theta$, $J_2/|J_3| = \rho\sin\theta$ are shown on a log-polar scale with $0 < \rho \lesssim 10^6$. The white circle corresponds to the path through parameter space shown in Fig. 3.

as $Er_2Ti_2O_7$, which is extremely well described by a nearest-neighbor exchange model [25–27], *do* order magnetically [25].

The phase diagram of $\mathcal{H}_{\rm ex}$ [Eq. (1)] for a quantum spin-1/2 has previously been studied using mean-field and spin-wave approximations, with many papers emphasizing connections with spin ice [5,8,9,11,46]. In this article we take a different approach, starting from an analysis of the way in which different spin configurations break the point-group symmetries of the pyrochlore lattice. We show that, for classical spins, the problem of finding the ground state of $\mathcal{H}_{\rm ex}$ [Eq. (1)] can be neatly separated into two steps: (i) finding the ground state of a single tetrahedron and (ii) understanding how the spin configuration on that tetrahedron can be used to tile the pyrochlore lattice. The first step, in turn, reduces to understanding how the different interactions in the model transform under the symmetries T_d of a single tetrahedron. The second step, summarized in a simple set of "Lego-brick" rules, enables us to encompass both ordered ground states, which break lattice symmetries, and spin liquids, which do not.

This approach, augmented by spin-wave calculations and extensive classical Monte Carlo simulations, makes it possible both to establish a complete phase diagram for $\mathcal{H}_{\rm ex}$ [Eq. (1)] as a function (J_1, J_2, J_3, J_4), and to link ground-state properties to predictions for neutron-scattering experiments. In this article, taking our motivation from estimated parameters for $Yb_2Ti_2O_7$ [44], $Er_2Ti_2O_7$ [26], and $Er_2Sn_2O_7$ [34], we concentrate on ordered phases in the limit $J_3 < 0$, $J_4 = 0$. Here there is a competition between four different types of order: a Palmer-Chalker [47] phase (Ψ_4), a noncollinear ferromagnet (FM), a coplanar antiferromagnet (Ψ_3), and a noncoplanar antiferromagnet (Ψ_2). The way in which these phases relate to one another is illustrated in Figs. 1,2, and 3.

Crucially, the same symmetry-based approach used to find ordered ground states also permits us to explore the way in which these physically distinct states are connected by the "accidental" degeneracies arising at boundaries between phases with different symmetry. The enlarged ground-state manifolds at these phase boundaries have far-reaching consequences, once quantum and thermal fluctuations are taken into account. The common theme which emerges is of systems "living on the edge"—the physical properties of materials showing one type of magnetic order being dictated by the proximity of another, competing, ordered phase.

Thus, in $Yb_2Ti_2O_7$, we find ferromagnetic order proximate to competing, "Ψ_3" and "Ψ_2" phases, which manifest themselves in the "rods" seen in neutron scattering. Meanwhile, in $Er_2Ti_2O_7$, we discover that the reason fluctuations select the well-established Ψ_2 ground state [25–27] is proximity to a neighboring Palmer-Chalker phase, as illustrated in Fig. 4. And in the case of $Er_2Sn_2O_7$, we find that fluctuations of Palmer-Chalker order predominate, but that all forms of magnetic order are strongly suppressed by the proximity of a degenerate ground-state manifold connected to a neighboring Ψ_2 phase.

We note that the same approach of combining symmetry analysis and the Lego-brick rules can also be used to systematically search for unconventional ordered states and new (classical) spin-liquid phases on the pyrochlore lattice. This is a theme which will be developed elsewhere [48,49]. The remainder of the present article is structured as follows:

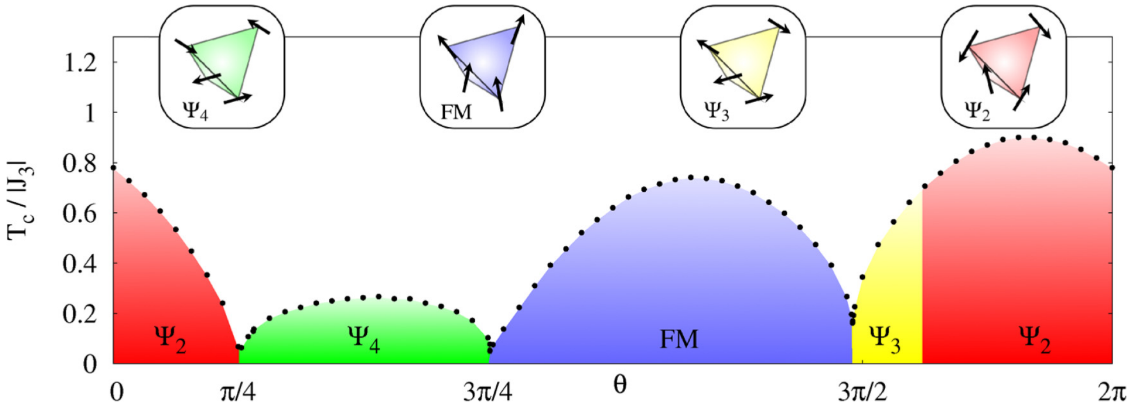

FIG. 3. Finite-temperature phase diagram for a pyrochlore magnet with anisotropic exchange interactions. The model considered is $\mathcal{H}_{\text{ex}}$ [Eq. (1)], with $J_1 = 3|J_3|\cos\theta$, $J_2 = 3|J_3|\sin\theta$, $J_3 < 0$, and $J_4 \equiv 0$, corresponding to the white circle in Fig. 1. Points show finite temperature phase transitions found from classical Monte Carlo simulations. The four ordered phases, Palmer-Chalker (Ψ_4), noncollinear ferromagnetic (FM), coplanar antiferromagnetic (Ψ_3), and noncoplanar antiferromagnetic (Ψ_2), are illustrated at the top of the figure. Each of these phases is sixfold degenerate, with zero crystal momentum, and is completely specified by the spin configuration in a single tetrahedron.

In Sec. II we introduce a general model of nearest-neighbor exchange interactions on a pyrochlore lattice and, restricting to classical spins, establish the conditions under which the model has a magnetically ordered ground state. We also provide a complete classification of possible ordered states in terms of the irreducible representations of the tetrahedral symmetry group T_d.

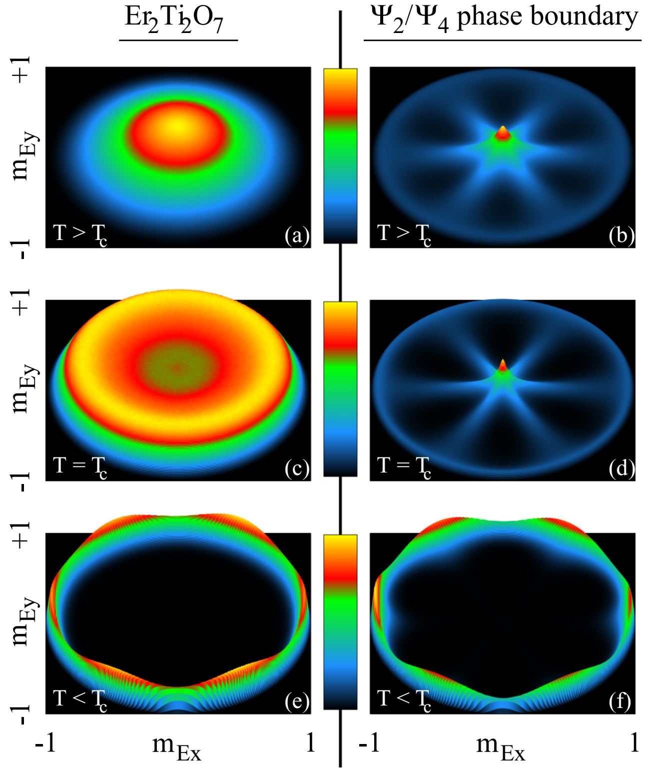

FIG. 4. Selection of an ordered ground state by thermal fluctuations in $Er_2Ti_2O_7$. For $T < T_c$, fluctuations select six states with noncoplanar antiferromagnetic order (Ψ_2) from a one-dimensional manifold of degenerate ground states. The entropic selection of these six states can be traced to an enlarged ground-state manifold found on the boundary with the Palmer-Chalker phase (Ψ_4). Plots show the probability distribution of the order parameter $\mathbf{m}_{\mathsf{E}} = (m_{\mathsf{E}_x}, m_{\mathsf{E}_y})$, as described in Sec. VI.

In Sec. III we show that this symmetry analysis can be used to determine the classical ground state of $\mathcal{H}_{\text{ex}}$ [Eq. (1)] for arbitrary parameters (J_1, J_2, J_3, J_4). The nature of the ground states in the limit $(J_3 < 0, J_4 = 0)$, which is of particular relevance to real materials, is explored in some detail, including analysis of the degenerate manifolds arising at the phase boundaries of the model.

In Sec. IV we explore the spin-wave excitations associated with these ordered phases. This enables us to make predictions for neutron scattering, and to develop a ground-state phase diagram for classical and semiclassical spins, focusing again on the limit $J_3 < 0$ and $J_4 = 0$, as illustrated in Fig. 1. It also enables us to identify regions of the phase diagram where strong quantum fluctuations are liable to eliminate classical order entirely, as illustrated in Fig. 2.

In Sec. V we use classical Monte Carlo simulation to explore the finite-temperature phase transitions which separate each of the ordered phases from the high-temperature paramagnet. The results of this analysis are summarized in Fig. 3.

In Sec. VI we study the finite-temperature consequences of the enlarged ground-state manifolds arising at the boundary between different ordered phases. This is illustrated in Fig. 4.

In Secs. VII, VIII, and IX we discuss the implications of these results for the rare-earth pyrochlore oxides $Er_2Ti_2O_7$, $Yb_2Ti_2O_7$, and $Er_2Sn_2O_7$, respectively. Other rare-earth pyrochlore magnets to which the theory might apply are discussed briefly in Sec. X.

We conclude in Sec. XI with a summary of our results, and an overview of some of the interesting open issues.

Technical details of calculations are reproduced in a short series of Appendixes at the end of the article: Appendix A provides details of the local coordinate frame throughout the article, and the associated form of the g tensor. Appendix B provides technical details of the linear spin-wave calculations described in Sec. IV. Appendix C provides technical details associated with the classical Monte Carlo simulations described in Sec. V.

As far as possible, we have endeavored to make Secs. VII–X, describing the application of the theory to experiments on rare-earth pyrochlores, self-contained. Readers chiefly interested in these materials may safely omit the theoretical development in Secs. III to VI of the article.

II. MICROSCOPIC MODEL OF ANISOTROPIC EXCHANGE

A. Magnetism at the level of a single ion

Pyrochlore oxides, $A_2B_2O_7$, are a ubiquitous feature of igneous rocks throughout the world. This broad family of materials takes its name from the mineral "pyrochlore" [$(Ca, Na)_2Nb_2O_6(OH,F)$], which burns with a green (χλωρὸς) fire (πῦρ), and shares its crystal structure with a great many other oxides, halides, and chalcogenides. Here we concentrate on those pyrochlore oxides in which the B cation is a nonmagnetic transition metal, such as Ti^{4+} or Sn^{4+}, while the remaining cation A^{3+} is a rare-earth ion with a magnetic doublet ground state. These magnetic ions form a *pyrochlore lattice*, built of corner-sharing tetrahedra, which shares the same cubic symmetry $Fd\bar{3}m$ as the parent material.

Even within this restricted group of rare-earth oxides, the interplay between strong spin-orbit coupling, and the crystal electric field (CEF) at the A-cation site, leads to a huge variation in the magnetic properties of the rare-earth ion. For example, Dy^{3+} provides the strong Ising moment in the spin-ice $Dy_2Ti_2O_7$, while Er^{3+} forms a moment with XY-like character in $Er_2Ti_2O_7$ [50].

The goal of this article is not to explore the intricate CEF ground states of rare-earth ions (see, e.g., Refs. [51,52] for a discussion on this topic), but rather to understand the way in which the anisotropic exchange interactions between them shape the magnetism of rare-earth pyrochlore oxides. We therefore concentrate on materials in which the ground state of the rare-earth ion is a Kramers doublet, with an odd number of electrons, like Yb^{3+} ($[Xe]4f^{13}$) or Er^{3+} ($[Xe]4f^{11}$).

In this case, as long as the temperature is small compared with the lowest-lying CEF excitation, the magnetic ion can be described by a pseudospin-1/2 degree of freedom

$$[S^{\mu},S^{\nu}] = i\epsilon_{\mu\nu\xi}S^{\xi}. \tag{2}$$

It is important to note that, even with the restriction to Kramers doublets, there is more than one possibility for how S^{μ} will transform under space-group operations [53]. In this article we will focus on the case where S^{μ} transforms like a magnetic dipole, which is the case appropriate to Yb^{3+} and Er^{3+} based pyrochlores. We note that an alternative "dipolar-octupolar" case may be realized in Dy^{3+}, Nd^{3+}, and Ce^{3+} based pyrochlores [40,53,54].

Where S^{μ} transforms like a magnetic dipole, it will be associated with an effective magnetic moment

$$m_i^{\mu} = \sum_{\nu=1}^{3} g_i^{\mu\nu} S_i^{\nu}, \tag{3}$$

where μ, $\nu = \{x,y,z\}$. Since the magnetic anisotropy of a rare-earth ion is determined by the local CEF, the g-tensor $g_i^{\mu\nu}$ is site dependent, as described in Appendix A. This has important consequences for the magnetic correlations measured in neutron scattering experiments, discussed below.

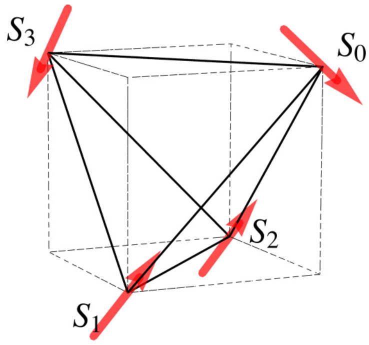

FIG. 5. A single tetrahedron within the pyrochlore lattice, showing the convention used in labeling sites. The positions of the magnetic sites relative to the center of the tetrahedron are defined in Appendix A.

B. Anisotropy in exchange interactions

The interplay between spin-orbit coupling and CEF leads to anisotropy in the interactions between rare-earth ions, just as it leads to anisotropy in the magnetic ground state of an individual ion [51]. It is possible to make estimates of exchange interactions in pyrochlore oxides from knowledge of the CEF ground state and low-lying excitations [52,55]. However for the purposes of this article it is sufficient to consider the constraints on these interactions imposed by the symmetry of the lattice.

In the case of Kramers ions on a pyrochlore lattice, the most general form of nearest-neighbor exchange can be broken down into a sum over tetrahedra t,

$$\mathcal{H}_{\text{ex}} = \sum_{\langle ij\rangle} J_{ij}^{\mu\nu} S_i^{\mu} S_j^{\nu} = \sum_{t} \mathcal{H}_{\text{ex}}^{\text{tet}}[t], \tag{4}$$

where

$$\mathcal{H}_{\text{ex}}^{\text{tet}}[t] = \sum_{i,j\in t} \mathbf{S}_i \mathbf{J}_{ij}^{[t]} \mathbf{S}_j. \tag{5}$$

Here $\mathbf{S}_i = (S_i^x, S_i^y, S_i^z)$, and $\mathbf{J}_{ij}^{[t]}$ is a 3×3 matrix specific to the bond ij, within tetrahedron t. The exchange interactions $\mathbf{J}_{ij}$ do not, in general, possess *any* continuous spin-rotation invariance. Nonetheless, the form of exchange $\mathbf{J}_{ij}$ *is* strongly constrained by the symmetry of the bond ij, and the interactions on different bonds must also be related by lattice symmetries.

Once these constraints are taken into account [42], $\mathbf{J}_{ij}$ is a function of just four independent parameters and, for the six bonds which make up the tetrahedron shown in Fig. 5, can be written

$$\mathbf{J}_{01} = \begin{pmatrix} J_2 & J_4 & J_4 \\ -J_4 & J_1 & J_3 \\ -J_4 & J_3 & J_1 \end{pmatrix}, \quad \mathbf{J}_{02} = \begin{pmatrix} J_1 & -J_4 & J_3 \\ J_4 & J_2 & J_4 \\ J_3 & -J_4 & J_1 \end{pmatrix},$$

$$\mathbf{J}_{03} = \begin{pmatrix} J_1 & J_3 & -J_4 \\ J_3 & J_1 & -J_4 \\ J_4 & J_4 & J_2 \end{pmatrix}, \quad \mathbf{J}_{12} = \begin{pmatrix} J_1 & -J_3 & J_4 \\ -J_3 & J_1 & -J_4 \\ -J_4 & J_4 & J_2 \end{pmatrix},$$

$$\mathbf{J}_{13} = \begin{pmatrix} J_1 & J_4 & -J_3 \\ -J_4 & J_2 & J_4 \\ -J_3 & -J_4 & J_1 \end{pmatrix},$$

$$\mathbf{J}_{23} = \begin{pmatrix} J_2 & -J_4 & J_4 \\ J_4 & J_1 & -J_3 \\ -J_4 & -J_3 & J_1 \end{pmatrix}, \tag{6}$$

where we label lattice sites and interactions following the conventions of Ross *et al.* [44]. The structure of these matrices imply that the different contributions to the interaction $\mathbf{J}_{ij}$ [Eq. (6)] can be approximately identified as

(i) $J_1 \rightarrow$ "XY" with respect to the local bond.
(ii) $J_2 \rightarrow$ "Ising" with respect to the local bond.
(iii) $J_3 \rightarrow$ symmetric off-diagonal exchange.
(iv) $J_4 \rightarrow$ Dzyaloshinskii-Moriya.

The anisotropic nearest-neighbor exchange model $\mathcal{H}_{\rm ex}$ [Eq. (1)] has been applied with considerable success to a number of pyrochlore oxides. In the case of $Yb_2Ti_2O_7$, $\mathcal{H}_{\rm ex}$ [Eq. (1)] has been shown to give an excellent description of spin-wave spectra measured in magnetic field [44]. Thermodynamic quantities, calculated from $\mathcal{H}_{\rm ex}$ [Eq. (1)] using the parameters from [44], also gave a very good description of experiments [56,57]. Parameters for $Er_2Ti_2O_7$ have been extracted from equivalent inelastic neutron scattering experiments [26], and from measurements of the field dependence of magnetization at low temperature [58]. The model $\mathcal{H}_{\rm ex}$ [Eq. (1)], using parameters taken from neutron scattering [26], has been shown to give good agreement with the observed spin-wave spectrum in $Er_2Ti_2O_7$, consistent with quantum order-by-disorder [26]. Anisotropic nearest-neighbor exchange parameters for $Er_2Sn_2O_7$ have also been estimated from measurements of the magnetization curve [34].

Representative estimates of the exchange parameters (J_1, J_2, J_3, J_4) taken from experiment on $Yb_2Ti_2O_7$ [44], $Er_2Ti_2O_7$ [26], and $Er_2Sn_2O_7$ [34], are shown in Table I. The typical scale of interactions is $|J| \sim 0.1$ meV (i.e., $|J| \sim 1$ K), with typical uncertainty in estimates of order $\delta J \sim 0.02$ meV (i.e., $\delta J \sim 0.2$ K) [26,34,44]. In all of these cases, the symmetric off-diagonal exchange interaction J_3 is negative, while the Dzyaloshinskii-Moriya interaction J_4 is relatively small [60].

TABLE I. Estimates of the parameters for anisotropic nearneighbor exchange, taken from experiments on $Yb_2Ti_2O_7$ [44], $Er_2Ti_2O_7$ [26], and $Er_2Sn_2O_7$ [34]. Values are quoted for exchange interactions in both the crystal coordinate frame $\mathcal{H}_{\rm ex}$ [Eq. (1)], and the local coordinate frame $\mathcal{H}_{\rm ex}^{\rm local}$ [Eq. (8)], following the notation of Ross *et al.* [44]. An alternative set of parameters for $Yb_2Ti_2O_7$ has recently been proposed by Robert *et al.* [73].

	$Yb_2Ti_2O_7$ [44]	$Er_2Ti_2O_7$ [26]	$Er_2Sn_2O_7$ [34]
J_1	−0.09 meV	0.11 meV	0.07 meV
J_2	−0.22 meV	−0.06 meV	0.08 meV
J_3	−0.29 meV	−0.10 meV	−0.11 meV
J_4	0.01 meV	−0.003 meV	0.04 meV
J_{zz}	0.17 meV	−0.025 meV	0
$J_{\pm}$	0.05 meV	0.065 meV	0.014 meV
$J_{\pm\pm}$	0.05 meV	0.042 meV	0.074 meV
$J_{z\pm}$	−0.14 meV	−0.009 meV	0

C. Anisotropic exchange in a local frame

Since both the anisotropy in magnetic ground state of the rare-earth ion, and the anisotropy in its interactions, are dictated by the local CEF field, it is often convenient to describe them in a local coordinate frame

$$\{\mathbf{x}_i^{\rm local}, \mathbf{y}_i^{\rm local}, \mathbf{z}_i^{\rm local}\},$$

such that the axis $\mathbf{z}_i^{\rm local}$ aligns with the C_3 symmetry axis of the local CEF on site i, as described in Appendix A. We introduce a SU(2) (pseudo)spin-1/2 in this local frame

$$[\mathsf{S}_i^\alpha, \mathsf{S}_i^\beta] = i\epsilon_{\alpha\beta\gamma}\mathsf{S}_i^\gamma, \tag{7}$$

where $\alpha, \beta, \gamma = \{\mathbf{x}_i^{\rm local}, \mathbf{y}_i^{\rm local}, \mathbf{z}_i^{\rm local}\}$. Note that throughout the paper S_i^α will refer to the spin components in this local frame, while S_i^α refers to the spin components in the global, crystal, coordinate system.

In the local coordinate frame, the most general form of exchange interactions between Kramers ions on the pyrochlore lattice can be written [44]

$$\begin{aligned} \mathcal{H}_{\rm ex}^{\rm local} = \sum_{\langle ij \rangle} \{ & J_{zz}\mathsf{S}_i^z\mathsf{S}_j^z - J_{\pm}(\mathsf{S}_i^+\mathsf{S}_j^- + \mathsf{S}_i^-\mathsf{S}_j^+) \\ & + J_{\pm\pm}[\gamma_{ij}\mathsf{S}_i^+\mathsf{S}_j^+ + \gamma_{ij}^*\mathsf{S}_i^-\mathsf{S}_j^-] \\ & + J_{z\pm}[\mathsf{S}_i^z(\zeta_{ij}\mathsf{S}_j^+ + \zeta_{ij}^*\mathsf{S}_j^-) + i \leftrightarrow j]\}, \end{aligned} \tag{8}$$

where the matrix

$$\zeta = \begin{pmatrix} 0 & -1 & e^{i\frac{\pi}{3}} & e^{-i\frac{\pi}{3}} \\ -1 & 0 & e^{-i\frac{\pi}{3}} & e^{i\frac{\pi}{3}} \\ e^{i\frac{\pi}{3}} & e^{-i\frac{\pi}{3}} & 0 & -1 \\ e^{-i\frac{\pi}{3}} & e^{i\frac{\pi}{3}} & -1 & 0 \end{pmatrix}, \quad \gamma = -\zeta^* \tag{9}$$

encode the change in coordinate frame between different sublattices.

The relationship between the parameters in this local frame, $(J_{zz}, J_{\pm}, J_{\pm\pm}, J_{z\pm})$, and exchange parameters in the global frame of the crystal axes (J_1, J_2, J_3, J_4), is given in Table II. Corresponding estimated parameters from experiment on $Yb_2Ti_2O_7$ [44], $Er_2Ti_2O_7$ [26], and $Er_2Sn_2O_7$ [34] are shown in Table I.

TABLE II. Relationship between the parameters of the anisotropic nearest-neighbor exchange model in the local coordinate frame $\mathcal{H}_{\rm ex}^{\rm local}$ [Eq. (8)], and the exchange parameters in the crystal coordinate frame $\mathcal{H}_{\rm ex}$ [Eq. (1)]. The notation used for the different components of the interaction follows Ross *et al.* [44].

Interaction in local coordinate frame	Exchange parameters in global frame
J_{zz}	$-\frac{1}{3}(2J_1 - J_2 + 2J_3 + 4J_4)$
$J_{\pm}$	$\frac{1}{6}(2J_1 - J_2 - J_3 - 2J_4)$
$J_{\pm\pm}$	$\frac{1}{6}(J_1 + J_2 - 2J_3 + 2J_4)$
$J_{z\pm}$	$\frac{1}{3\sqrt{2}}(J_1 + J_2 + J_3 - J_4)$

D. Proof of the existence of a classical ground state with $\mathbf{q} = 0$, 4-sublattice order

Finding the ground state of $\mathcal{H}_{\text{ex}}$ [Eq. (1)], for a quantum (pseudo)spin-1/2, and arbitrary exchange interactions (J_1, J_2, J_3, J_4), is a very difficult problem, in general only tractable as a mean-field theory [5,8,9,11,46]. However, many rare-earth pyrochlores are known to have relatively simple ground states, with vanishing crystal momentum $\mathbf{q} = 0$, implying a 4-sublattice magnetic order [17]. Here we show that, under the restriction that $\mathbf{S}_i$ is a classical variable, $\mathcal{H}_{\text{ex}}$ [Eq. (4)] *always* possesses a ground state of this type. In Sec. II E, below, we explore the conditions under which this classical ground state is unique.

We begin with the simple observation that, since $\mathcal{H}_{\text{ex}}$ [Eq. (1)] is expressed as a sum over individual tetrahedra, any state which minimizes the energy of each individual tetrahedron must be a ground state. It is convenient to split this sum into two pieces:

$$\mathcal{H}_{\text{ex}} = \sum_{t \in \mathsf{A}} \mathcal{H}^{\mathsf{A}}_{\text{ex}}[t] + \sum_{t' \in \mathsf{B}} \mathcal{H}^{\mathsf{B}}_{\text{ex}}[t'], \tag{10}$$

where A and B refer to the two distinct sublattices of tetrahedra, with

$$\mathcal{H}^{\mathsf{A}}_{\text{ex}}[t] = \sum_{i,j \in t} \mathbf{S}_i \mathbf{J}^{[\mathsf{A}]}_{ij} \mathbf{S}_j, \tag{11}$$

$$\mathcal{H}^{\mathsf{B}}_{\text{ex}}[t'] = \sum_{i,j \in t'} \mathbf{S}_i \mathbf{J}^{[\mathsf{B}]}_{ij} \mathbf{S}_j. \tag{12}$$

The interactions $\mathbf{J}^{[\mathsf{A}]}_{ij}$ and $\mathbf{J}^{[\mathsf{B}]}_{ij}$ are related by inversion about a single site $\mathcal{I}$,

$$\mathbf{J}^{[\mathsf{B}]}_{ij} = \mathcal{I} \cdot \mathbf{J}^{[\mathsf{A}]}_{ij} \cdot \mathcal{I}. \tag{13}$$

Since $\mathcal{I}^2 = 1$, we can write

$$\begin{aligned} \mathbf{S}_i \cdot \mathbf{J}^{[\mathsf{A}]}_{ij} \cdot \mathbf{S}_j &= \mathbf{S}_i \cdot \mathcal{I}^2 \cdot \mathbf{J}^{[\mathsf{A}]}_{ij} \cdot \mathcal{I}^2 \cdot \mathbf{S}_j \\ &= \mathbf{S}_i \cdot \mathcal{I} \cdot \mathbf{J}^{[\mathsf{A}]}_{ij} \cdot \mathcal{I} \cdot \mathbf{S}_j, \end{aligned} \tag{14}$$

where we have used the fact that the spin $\mathbf{S}_i$ is invariant under lattice inversion. This implies

$$\mathbf{J}^{[\mathsf{A}]}_{ij} = \mathcal{I} \cdot \mathbf{J}^{[\mathsf{A}]}_{ij} \cdot \mathcal{I} = \mathbf{J}^{[\mathsf{B}]}_{ij}. \tag{15}$$

It follows that interactions for *any* tetrahedron t is the same, regardless of which tetrahedral sublattice it belongs to, and we can safely write

$$\mathcal{H}^{\text{tet}}_{\text{ex}} = \sum_{i,j \in t} \mathbf{S}_i \mathbf{J}_{ij} \mathbf{S}_j, \tag{16}$$

where $\mathbf{J}_{ij}$ are given by Eq. (6) and the sum runs over all pairs of sites i, j in a given tetrahedron t, which may now be of either sublattice.

The proof we are seeking follows directly from this result [Eq. (16)]: for classical spins, $[\mathcal{H}^{\mathsf{A}}_{\text{ex}}, \mathcal{H}^{\mathsf{B}}_{\text{ex}}] = 0$, and we can construct a ground state of $\mathcal{H}_{\text{ex}}$ by choosing *any* state which minimizes the energy of a single tetrahedron, and repeating it across all A-sublattice (or B-sublattice) tetrahedra. Since every spin is shared between one A- and one B-sublattice tetrahedron, and the Hamiltonians for A or B sublattices are equivalent [Eq. (16)], any such classical spin configuration which minimizes the energy on one tetrahedral sublattice, simultaneously minimizes the energy on the other tetrahedral sublattice, and is a ground state of $\mathcal{H}_{\text{ex}}$ [Eq. (1)].

It follows that there *always* exists a classical, $\mathbf{q} = 0$ ground state of $\mathcal{H}_{\text{ex}}$ [Eq. (1)], with a 4-sublattice long-range magnetic order, for arbitrary exchange interactions (J_1, J_2, J_3, J_4). This is true *even* in the presence of finite Dzyaloshinskii-Moriya interaction J_4.

Such a $\mathbf{q} = 0$ ground state has a finite, discrete degeneracy associated with the breaking of point-group and time-reversal symmetries (in the case of classical spins, time-reversal corresponds to the inversion of all spins $\mathbf{S}_i \to -\mathbf{S}_i$). This degeneracy must be at least 2 (time reversal), and is typically 6 (C_3 rotations $\otimes$ time reversal), for the ordered phases considered in this article.

E. Conditions for the uniqueness of 4-sublattice order—The Lego-brick rules

The existence of a classical ground state of $\mathcal{H}_{\text{ex}}$ [Eq. (1)] with 4-sublattice magnetic order, for arbitrary exchange interactions (J_1, J_2, J_3, J_4) constitutes an enormous simplification, since it is much easier to determine the spin configuration which minimizes the energy of a single tetrahedron (as described in Sec. III, below) than to find the ground state of the entire lattice. However, as we shall see, many of interesting properties of rare-earth pyrochlores follow from the fact that while such a classical ground state must exist, it need not be unique.

Establishing the uniqueness of a 4-sublattice ground state, up to the discrete degeneracy of the state itself, amounts to determining the number of ways in which the spin configurations which minimize the energy of a single tetrahedron can be used to tile the entire lattice. For many purposes, it is convenient to think of these as a set of Lego-brick rules for fitting together spin configurations on a lattice (Fig. 6). These rules allow us to determine the degeneracy, and nature, of the ground states of the whole lattice, using the ground states of a single tetrahedron.

The rules can be stated as follows:

(1) If the spin on every site of the tetrahedron points in a different direction, in each of its classical ground states, then the 4-sublattice ground state of the lattice is unique (up to global symmetry operations). In this case, the degeneracy of the ground state of the lattice is the same as that of a single tetrahedron.

(2) If, within the set of ground states for a single tetrahedron, there are two states in which a single site has the same spin orientation, the 4-sublattice ground state of the lattice is not unique. In this case, the system undergoes a dimensional reduction into independent kagome planes, and the number of classical ground states is at least $O(2^L)$, where L is the linear size of the system.

(3) If, within the set of ground states for a single tetrahedron, there is a pair of states which have the same spin orientation on *two* sites, the 4-sublattice ground state is also not unique. However, in this case, the number of classical ground states must grow as *at least* $O(2^{L^2})$, corresponding to dimensional reduction into independent chains of spins. In the special case of spin ice, the corresponding classical ground-state degeneracy is extensive.

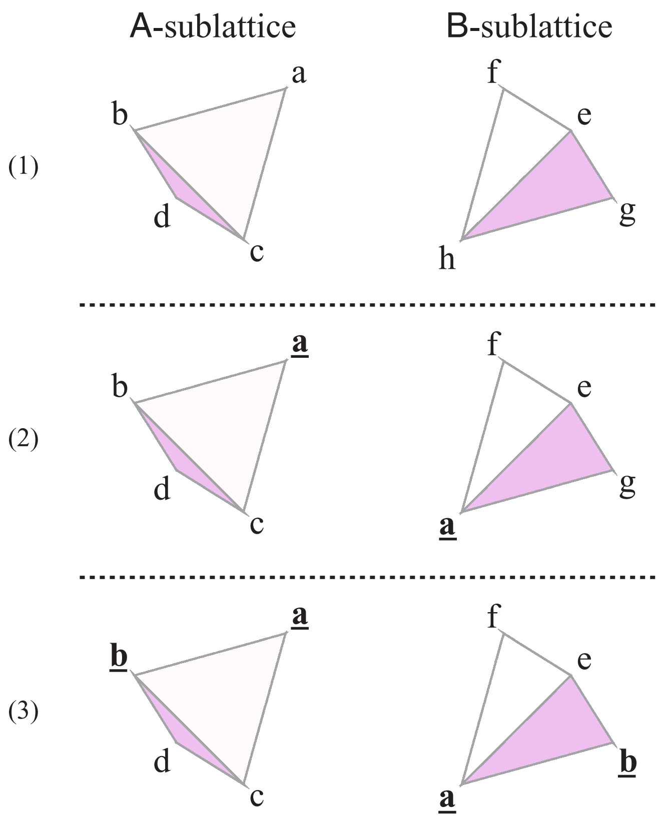

FIG. 6. The Lego-brick rules describing how the ground states of a single tetrahedron can be connected to tile the pyrochlore lattice. The two tetrahedra in the left and right panels represent a pair of tetrahedra in distinct ground-state configurations. Distinct spin orientations on the sites of each tetrahedron are denoted by letters **a**–**h**. Three cases are shown. In case (1) all of the ground states for a single tetrahedron have different spin orientations for any given site. This means that two tetrahedra in distinct ground states cannot be joined together because they do not share a common spin orientation on any site. In this case the 4-sublattice ground state of the lattice is unique with $q = 0$ order, up to global symmetry operations. In case (2) there are two ground-state configurations for a tetrahedron which share a common spin orientation on a single site, here denoted **a**. These tetrahedra can be joined together by sharing the spin in orientation **a**. In this case the ground state of the lattice has a degeneracy of at least $O(2^L)$. Indeed, successive kagome layers of spins can be independent in BDC or FEG configurations. In case (3) there is a pair of ground states which share common spin orientations on two sites, here denoted **a** and **b**. These tetrahedra can be joined together by sharing the spin in orientation **a** or the spin in orientation **b**. In this case the ground state of the lattice has a degeneracy of at least $O(2^{L^2})$.

The first rule guarantees the uniqueness of a 4-sublattice ground state, where the spin on every site of the tetrahedron points in a different direction in each of the ground states of a single tetrahedron. Away from phase boundaries, this is true for *all* of the 4-sublattice $\mathbf{q} = 0$ ordered phases discussed in this article. However, it is clear from rules 2 and 3 that if two of the ground states of a single tetrahedron share a common spin—i.e., the spin on a given site points in the same direction in more than one ground state—then it is *always* possible to construct other ground states, with finite $\mathbf{q}$.

To give a concrete example of how these Lego-brick rules work, let us assume that two different ground states for a single tetrahedron have identical orientation of the spin on site 0, but different orientation of the spins on sites 1, 2, and 3. In this case it is possible to divide the pyrochlore lattice into a set of parallel kagome planes, containing spins associated with sites 1, 2, and 3 of a tetrahedron, separated by triangular-lattice planes associated with site 0. Since each successive kagome plane can take on one of two different spin configurations, the number of such ground states grows as $2^{\mathsf{N}_{\mathsf{K}}}$, where N_{K} is the number of kagome planes, and encompasses all possible $\mathbf{q} \parallel [111]$. Dimensional reduction of this type occurs on the classical phase boundary between ordered FM and Palmer-Chalker phases discussed in Sec. III I of this article.

An example where rule 3 applies, and a set of independent chains emerges in the ground-state manifold, is the phase boundary between the Palmer-Chalker phase and the non-coplanar antiferromagnet discussed in Sec. III G. However, the Lego-brick rules permit even larger ground-state degeneracies, as is known from the "two-in, two-out" states, made famous by the spin-ice problem. In this case there are a total of six possible ground states for a single tetrahedron, but each possible spin orientation, on each site, belongs to three different ground states. According to rule 3, the 4-sublattice classical ground state—a ferromagnet—should not be unique, and the total number of classical grounds states must grow as *at least* $O(2^{L^2})$. In fact, the ground-state degeneracy of spin ice is extensive, scaling as $\Omega_{\mathsf{ice}} \sim (3/2)^{N/2}$, where N is the total number of sites in the lattice [62]. This manifold of spin-ice states includes ground states with all possible $\mathbf{q}$.

F. Representation theory

Except in very specific limits, such as the Heisenberg model ($J_1 = J_2 = J$, $J_3 = J_4 = 0$), Hamiltonian $\mathcal{H}_{\mathsf{ex}}$ [Eq. (1)] does not possess *any* continuous spin-rotation symmetry. The key to unlocking its properties, therefore, is to understand how different ordered states, and indeed different spin fluctuations, break the space-group symmetries of the pyrochlore lattice. This task is made easier by the realization that a classical ground state with $\mathbf{q} = 0$ exists for all possible (J_1, J_2, J_3, J_4), as discussed in Sec. II D. It is therefore possible to restrict discussion to the point-group symmetries of the lattice.

In what follows, we explore the consequences of applying representation theory for these point-group operations to a general model of anisotropic nearest-neighbor exchange on the pyrochlore lattice $\mathcal{H}_{\mathsf{ex}}$ [Eq. (1)]. This analysis serves a twofold purpose: it reduces the Hamiltonian for a single tetrahedron $\mathcal{H}_{\mathsf{ex}}^{\mathsf{tet}}$ [Eq. (16)] to a diagonal form, and it provides a set of order parameters with which to characterize the $\mathbf{q} = 0$, 4-sublattice ordered phases found in real materials.

The point-group symmetry of the pyrochlore lattice is the cubic symmetry group $\mathsf{O}_h = \mathsf{T}_d \times \mathsf{I}$. Here T_d is symmetry group of a single tetrahedron, and $\mathsf{I} = \{\epsilon, \mathcal{I}\}$, where ϵ is the identity and $\mathcal{I}$ corresponds to the lattice inversion introduced in Eq. (13). For classical spins, lattice inversion plays a benign role (cf. Sec. II D), and it is sufficient to consider T_d alone. The group T_d has 24 elements [63], corresponding to the symmetries of the tetrahedron: 8 × C_3—$\frac{2\pi}{3}$ rotation around a [111] axis; 3 × C_2—π rotation around [100] axis; 6 × S_4—$\frac{\pi}{2}$

TABLE III. Order parameters $\mathbf{m}_\lambda$, describing how the point-group symmetry of a single tetrahedron within the pyrochlore lattice is broken by magnetic order. Order parameters transform according to irreducible representations of the point-group T_d, and are expressed in terms of linear combinations of spin-components $\mathbf{S}_i = (S_i^x, S_i^y, S_i^z)$, in the global frame of the crystal axes—cf. $\mathcal{H}_{\mathsf{ex}}$ [Eq. (1)]. Labeling of spins within the tetrahedron follows the convention of Ross *et al.* [44]—cf. Fig. 5. The notation Ψ_i for ordered phases is taken from [65].

Order parameter	Definition in terms of spin components	Associated ordered phases
m_{A_2}	$\frac{1}{2\sqrt{3}}(S_0^x + S_0^y + S_0^z + S_1^x - S_1^y - S_1^z - S_2^x + S_2^y - S_2^z - S_3^x - S_3^y + S_3^z)$	all in-all out
$\mathbf{m}_{\mathsf{E}}$	$\begin{pmatrix} \frac{1}{2\sqrt{6}}(-2S_0^x + S_0^y + S_0^z - 2S_1^x - S_1^y - S_1^z + 2S_2^x + S_2^y - S_2^z + 2S_3^x - S_3^y + S_3^z) \\ \frac{1}{2\sqrt{2}}(-S_0^y + S_0^z + S_1^y - S_1^z - S_2^y - S_2^z + S_3^y + S_3^z) \end{pmatrix}$	Ψ_2 and Ψ_3
$\mathbf{m}_{\mathsf{T}_{1,\mathsf{A}}}$	$\begin{pmatrix} \frac{1}{2}(S_0^x + S_1^x + S_2^x + S_3^x) \\ \frac{1}{2}(S_0^y + S_1^y + S_2^y + S_3^y) \\ \frac{1}{2}(S_0^z + S_1^z + S_2^z + S_3^z) \end{pmatrix}$	collinear FM
$\mathbf{m}_{\mathsf{T}_{1,\mathsf{B}}}$	$\begin{pmatrix} \frac{-1}{2\sqrt{2}}(S_0^y + S_0^z - S_1^y - S_1^z - S_2^y + S_2^z + S_3^y - S_3^z) \\ \frac{-1}{2\sqrt{2}}(S_0^x + S_0^z - S_1^x + S_1^z - S_2^x - S_2^z + S_3^x - S_3^z) \\ \frac{-1}{2\sqrt{2}}(S_0^x + S_0^y - S_1^x + S_1^y + S_2^x - S_2^y - S_3^x - S_3^y) \end{pmatrix}$	noncollinear FM
$\mathbf{m}_{\mathsf{T}_2}$	$\begin{pmatrix} \frac{1}{2\sqrt{2}}(-S_0^y + S_0^z + S_1^y - S_1^z + S_2^y + S_2^z - S_3^y - S_3^z) \\ \frac{1}{2\sqrt{2}}(S_0^x - S_0^z - S_1^x - S_1^z - S_2^x + S_2^z + S_3^x + S_3^z) \\ \frac{1}{2\sqrt{2}}(-S_0^x + S_0^y + S_1^x + S_1^y - S_2^x - S_2^y + S_3^x - S_3^y) \end{pmatrix}$	Palmer-Chalker (Ψ_4)

rotation around a [100] axis followed by reflection in the same [100] plane; $6 \times \sigma_d$—reflection in [011] plane; and ϵ—the identity [64].

The different ways in which classical ground states with $\mathbf{q} = 0$ break the symmetries of a tetrahedron can be fully characterized by introducing order parameters $\mathbf{m}_\lambda$ which transform with the nontrivial irreducible representations $\lambda = \{\mathsf{A}_2,\ \mathsf{E},\ \mathsf{T}_1,\ \mathsf{T}_2\}$ of T_d. These order parameters are formed by linear combinations of spin components, and can be expressed in either global coordinate frame of $\mathcal{H}_{\mathsf{ex}}$ [Eq. (1)]—cf. Table III—or in the local coordinate frame of $\mathcal{H}_{\mathsf{ex}}^{\mathsf{local}}$ [Eq. (8)]—cf. Table IV.

The anisotropic exchange Hamiltonian $\mathcal{H}_{\mathsf{ex}}^{\mathsf{tet}}$ [Eq. (16)] can be transcribed exactly in terms of same set of irreps:

$$\begin{aligned} \mathcal{H}_{\mathsf{ex}}^{\mathsf{tet}} \equiv \tfrac{1}{2}\big[& a_{\mathsf{A}_2}\, m_{\mathsf{A}_2}^2 + a_{\mathsf{E}}\, \mathbf{m}_{\mathsf{E}}^2 + a_{\mathsf{T}_2}\, \mathbf{m}_{\mathsf{T}_2}^2 + a_{\mathsf{T}_{1,\mathsf{A}}}\, \mathbf{m}_{\mathsf{T}_{1,\mathsf{A}}}^2 \\ &+ a_{\mathsf{T}_{1,\mathsf{B}}}\, \mathbf{m}_{\mathsf{T}_{1,\mathsf{B}}}^2 + a_{\mathsf{T}_{1,\mathsf{AB}}}\, \mathbf{m}_{\mathsf{T}_{1,\mathsf{A}}} \cdot \mathbf{m}_{\mathsf{T}_{1,\mathsf{B}}}\big], \end{aligned} \tag{17}$$

TABLE IV. Order parameters $\mathbf{m}_\lambda$, describing how the point-group symmetry of a single tetrahedron within the pyrochlore lattice is broken by magnetic order. Order parameters are irreducible representations of the point-group T_d, and are expressed in terms of linear combinations of spin-components $\mathsf{S}_i = (\mathsf{S}_i^x, \mathsf{S}_i^y, \mathsf{S}_i^z)$, in the local frame of the magnetic ions—cf. $\mathcal{H}_{\mathsf{ex}}^{\mathsf{local}}$ [Eq. (8)]. For convenience, in this table, the local axes $(x^{\mathsf{local}}, y^{\mathsf{local}}, z^{\mathsf{local}})$ are simply written (x, y, z). Labeling of spins within the tetrahedron follows the convention of Ross *et al.* [44]—cf. Fig. 5.

Order parameter	Definition in terms of local spin components
m_{A_2}	$\frac{1}{2}(\mathsf{S}_0^z + \mathsf{S}_1^z + \mathsf{S}_2^z + \mathsf{S}_3^z)$
$\mathbf{m}_{\mathsf{E}}$	$\frac{1}{2}\begin{pmatrix} \mathsf{S}_0^x + \mathsf{S}_1^x + \mathsf{S}_2^x + \mathsf{S}_3^x \\ \mathsf{S}_0^y + \mathsf{S}_1^y + \mathsf{S}_2^y + \mathsf{S}_3^y \end{pmatrix}$
$\mathbf{m}_{\mathsf{T}_{1,\mathsf{A}}}$	$\begin{pmatrix} \frac{1}{2\sqrt{3}}(-\sqrt{2}\mathsf{S}_0^x + \mathsf{S}_0^z - \sqrt{2}\mathsf{S}_1^x + \mathsf{S}_1^z + \sqrt{2}\mathsf{S}_2^x - \mathsf{S}_2^z + \sqrt{2}\mathsf{S}_3^x - \mathsf{S}_3^z) \\ \frac{1}{12}(\sqrt{6}\mathsf{S}_0^x - 3\sqrt{2}\mathsf{S}_0^y + 2\sqrt{3}\mathsf{S}_0^z - \sqrt{6}\mathsf{S}_1^x + 3\sqrt{2}\mathsf{S}_1^y - 2\sqrt{3}\mathsf{S}_1^z + \sqrt{6}\mathsf{S}_2^x - 3\sqrt{2}\mathsf{S}_2^y + 2\sqrt{3}\mathsf{S}_2^z - \sqrt{6}\mathsf{S}_3^x + 3\sqrt{2}\mathsf{S}_3^y - 2\sqrt{3}\mathsf{S}_3^z) \\ \frac{1}{12}(\sqrt{6}\mathsf{S}_0^x + 3\sqrt{2}\mathsf{S}_0^y + 2\sqrt{3}\mathsf{S}_0^z - \sqrt{6}\mathsf{S}_1^x - 3\sqrt{2}\mathsf{S}_1^y - 2\sqrt{3}\mathsf{S}_1^z - \sqrt{6}\mathsf{S}_2^x - 3\sqrt{2}\mathsf{S}_2^y - 2\sqrt{3}\mathsf{S}_2^z + \sqrt{6}\mathsf{S}_3^x + 3\sqrt{2}\mathsf{S}_3^y + 2\sqrt{3}\mathsf{S}_3^z) \end{pmatrix}$
$\mathbf{m}_{\mathsf{T}_{1,\mathsf{B}}}$	$\begin{pmatrix} \frac{1}{2\sqrt{3}}(-\sqrt{2}\mathsf{S}_0^x - \mathsf{S}_0^z - \sqrt{2}\mathsf{S}_1^x - \mathsf{S}_1^z + \sqrt{2}\mathsf{S}_2^x + \mathsf{S}_2^z + \sqrt{2}\mathsf{S}_3^x + \mathsf{S}_3^z) \\ \frac{1}{12}(\sqrt{6}\mathsf{S}_0^x - 3\sqrt{2}\mathsf{S}_0^y - 2\sqrt{3}\mathsf{S}_0^z - \sqrt{6}\mathsf{S}_1^x + 3\sqrt{2}\mathsf{S}_1^y + 2\sqrt{3}\mathsf{S}_1^z + \sqrt{6}\mathsf{S}_2^x - 3\sqrt{2}\mathsf{S}_2^y - 2\sqrt{3}\mathsf{S}_2^z - \sqrt{6}\mathsf{S}_3^x + 3\sqrt{2}\mathsf{S}_3^y + 2\sqrt{3}\mathsf{S}_3^z) \\ \frac{1}{12}(\sqrt{6}\mathsf{S}_0^x + 3\sqrt{2}\mathsf{S}_0^y - 2\sqrt{3}\mathsf{S}_0^z - \sqrt{6}\mathsf{S}_1^x - 3\sqrt{2}\mathsf{S}_1^y + 2\sqrt{3}\mathsf{S}_1^z - \sqrt{6}\mathsf{S}_2^x - 3\sqrt{2}\mathsf{S}_2^y + 2\sqrt{3}\mathsf{S}_2^z + \sqrt{6}\mathsf{S}_3^x + 3\sqrt{2}\mathsf{S}_3^y - 2\sqrt{3}\mathsf{S}_3^z) \end{pmatrix}$
$\mathbf{m}_{\mathsf{T}_2}$	$\begin{pmatrix} \frac{1}{2}(-\mathsf{S}_0^y - \mathsf{S}_1^y + \mathsf{S}_2^y + \mathsf{S}_3^y) \\ \frac{1}{4}(\sqrt{3}\mathsf{S}_0^x + \mathsf{S}_0^y - \sqrt{3}\mathsf{S}_1^x - \mathsf{S}_1^y + \sqrt{3}\mathsf{S}_2^x + \mathsf{S}_2^y - \sqrt{3}\mathsf{S}_3^x - \mathsf{S}_3^y) \\ \frac{1}{4}(-\sqrt{3}\mathsf{S}_0^x + \mathsf{S}_0^y + \sqrt{3}\mathsf{S}_1^x - \mathsf{S}_1^y + \sqrt{3}\mathsf{S}_2^x - \mathsf{S}_2^y - \sqrt{3}\mathsf{S}_3^x + \mathsf{S}_3^y) \end{pmatrix}$

TABLE V. Coefficients a_λ of the scalar invariants $|\mathbf{m}_\lambda|^2$ appearing in $\mathcal{H}_{\mathsf{ex}}^{[\mathsf{T_d}]}$ [Eq. (21)]. Coefficients are expressed as a function of (J_1, J_2, J_3, J_4), the parameters of $\mathcal{H}_{\mathsf{ex}}$ [Eq. (1)]; and $(J_{zz}, J_\pm, J_{\pm\pm}, J_{z\pm})$, the parameters of $\mathcal{H}_{\mathsf{ex}}^{\mathsf{local}}$ [Eq. (8)], with the canting angle $\theta_{\mathsf{T_1}}$ defined in Eq. (20). The classical ground states of $\mathcal{H}_{\mathsf{ex}}$ [Eq. (4)] can be found by identifying the coefficient(s) a_λ with the lowest value, and imposing the constraint of fixed spin length, Eq. (24), on the associated $\mathbf{m}_\lambda$.

Coefficient of $\lvert\mathbf{m}_\lambda\rvert^2$	Definition in terms of parameters of $\mathcal{H}_{\mathsf{ex}}$ [Eq. (1)]	Definition in terms of parameters of $\mathcal{H}_{\mathsf{ex}}^{\mathsf{local}}$ [Eq. (8)]
$a_{\mathsf{A_2}}$	$-2J_1 + J_2 - 2(J_3 + 2J_4)$	$3J_{zz}$
a_{E}	$-2J_1 + J_2 + J_3 + 2J_4$	$-6J_\pm$
$a_{\mathsf{T_2}}$	$-J_2 + J_3 - 2J_4$	$2J_\pm - 4J_{\pm\pm}$
$a_{\mathsf{T_{1,A'}}}$	$(2J_1 + J_2)\cos^2(\theta_{\mathsf{T_1}}) - (J_2 + J_3 - 2J_4)\sin^2(\theta_{\mathsf{T_1}})$ $+\sqrt{2}J_3\sin(2\theta_{\mathsf{T_1}})$	$\frac{1}{3}(4J_\pm + 8J_{\pm\pm} + 8\sqrt{2}J_{z\pm} - J_{zz})\cos^2(\theta_{\mathsf{T_1}})$ $+\frac{2}{3}(1J_\pm + 2J_{\pm\pm} - 4\sqrt{2}J_{z\pm} - J_{zz})\sin^2(\theta_{\mathsf{T_1}})$ $+\frac{\sqrt{2}}{3}(-2J_\pm - 4J_{\pm\pm} + 2\sqrt{2}J_{z\pm} - J_{zz})\sin(2\theta_{\mathsf{T_1}})$
$a_{\mathsf{T_{1,B'}}}$	$(2J_1 + J_2)\sin^2(\theta_{\mathsf{T_1}}) - (J_2 + J_3 - 2J_4)\cos^2(\theta_{\mathsf{T_1}})$ $-\sqrt{2}J_3\sin(2\theta_{\mathsf{T_1}})$	$\frac{1}{3}(4J_\pm + 8J_{\pm\pm} + 8\sqrt{2}J_{z\pm} - J_{zz})\sin^2(\theta_{\mathsf{T_1}})$ $-\frac{2}{3}(1J_\pm + 2J_{\pm\pm} - 4\sqrt{2}J_{z\pm} - J_{zz})\cos^2(\theta_{\mathsf{T_1}})$ $-\frac{\sqrt{2}}{3}(-2J_\pm - 4J_{\pm\pm} + 2\sqrt{2}J_{z\pm} - J_{zz})\sin(2\theta_{\mathsf{T_1}})$

where the coefficients

$$\begin{aligned} a_{\mathsf{A_2}} &= -2J_1 + J_2 - 2(J_3 + 2J_4), \\ a_{\mathsf{E}} &= -2J_1 + J_2 + J_3 + 2J_4, \\ a_{\mathsf{T_2}} &= -J_2 + J_3 - 2J_4, \\ a_{\mathsf{T_{1,A}}} &= 2J_1 + J_2, \\ a_{\mathsf{T_{1,B}}} &= -J_2 - J_3 + 2J_4, \\ a_{\mathsf{T_{1,AB}}} &= -\sqrt{8}J_3 \end{aligned} \tag{18}$$

are completely determined by the parameters of $\mathcal{H}_{\mathsf{ex}}$ [Eq. (1)]. Equivalent expressions for a_λ can be found in terms of the parameters of $\mathcal{H}_{\mathsf{ex}}^{\mathsf{local}}$ [Eq. (8)]. We note that a similar analysis, applied to $Er_2Ti_2O_7$, appears in Ref. [43], with a different choice of basis for the two appearances of the $\mathsf{T_1}$ irrep. Note that this is entirely different from the analysis appearing in Ref. [42] which classifies wave functions for spin-1/2 on a tetrahedron according to the irreps of T_d, not linear combinations of spin operators.

Symmetry permits a finite coupling $a_{\mathsf{T_{1,AB}}} \neq 0$ between the two distinct $\mathsf{T_1}$ irreps $\mathbf{m}_{\mathsf{T_{1,A}}}$ and $\mathbf{m}_{\mathsf{T_{1,B}}}$. This can be eliminated from $\mathcal{H}_{\mathsf{ex}}^{\mathsf{tet}}$ by a coordinate transformation

$$\begin{aligned} \mathbf{m}_{\mathsf{T_{1,A'}}} &= \cos\theta_{\mathsf{T_1}}\,\mathbf{m}_{\mathsf{T_{1,A}}} - \sin\theta_{\mathsf{T_1}}\,\mathbf{m}_{\mathsf{T_{1,B}}}, \\ \mathbf{m}_{\mathsf{T_{1,B'}}} &= \sin\theta_{\mathsf{T_1}}\,\mathbf{m}_{\mathsf{T_{1,A}}} + \cos\theta_{\mathsf{T_1}}\,\mathbf{m}_{\mathsf{T_{1,B}}}, \end{aligned} \tag{19}$$

where

$$\theta_{\mathsf{T_1}} = \frac{1}{2}\arctan\left(\frac{\sqrt{8}J_3}{2J_1 + 2J_2 + J_3 - 2J_4}\right) \tag{20}$$

is the canting angle between spins and the relevant [100] axis in the ferromagnetic ground state. The Hamiltonian $\mathcal{H}_{\mathsf{ex}}^{\mathsf{tet}}$ then becomes

$$\begin{aligned} \mathcal{H}_{\mathsf{ex}}^{[\mathsf{T_d}]} = \tfrac{1}{2}\big[&a_{\mathsf{A_2}} m_{\mathsf{A_2}}^2 + a_{\mathsf{E}}\mathbf{m}_{\mathsf{E}}^2 + a_{\mathsf{T_2}}\mathbf{m}_{\mathsf{T_2}}^2 \\ &+ a_{\mathsf{T_{1,A'}}}\mathbf{m}_{\mathsf{T_{1,A'}}}^2 + a_{\mathsf{T_{1,B'}}}\mathbf{m}_{\mathsf{T_{1,B'}}}^2\big], \end{aligned} \tag{21}$$

with coefficients given in Table V. We wish to emphasize that $\mathcal{H}_{\mathsf{ex}}^{[\mathsf{T_d}]}$ [Eq. (21)] is an *exact transcription* of $\mathcal{H}_{\mathsf{ex}}^{\mathsf{tet}}$ [Eq. (16)] and *not* a phenomenological Landau theory. As such, $\mathcal{H}_{\mathsf{ex}}^{[\mathsf{T_d}]}$ [Eq. (21)] is subject to the constraint that every spin has fixed length.

For the majority of the discussion in this article, we shall be concerned with classical vectors $\mathbf{S}_i$ representing a (pseudo)spin-1/2, with

$$S = 1/2, \tag{22}$$

in which case

$$|\mathbf{S}_i|^2 = 1/4. \tag{23}$$

For spins belonging to a single tetrahedron, we can use symmetry [67] to express this constraint as

$$\begin{aligned} \mathbf{S}_0^2 + \mathbf{S}_1^2 + \mathbf{S}_2^2 + \mathbf{S}_3^2 &= 1, \\ \mathbf{S}_0^2 + \mathbf{S}_1^2 - \mathbf{S}_2^2 - \mathbf{S}_3^2 &= 0, \\ \mathbf{S}_0^2 - \mathbf{S}_1^2 + \mathbf{S}_2^2 - \mathbf{S}_3^2 &= 0, \\ \mathbf{S}_0^2 - \mathbf{S}_1^2 - \mathbf{S}_2^2 + \mathbf{S}_3^2 &= 0. \end{aligned} \tag{24}$$

The constraint of fixed spin length, Eq. (24), plays a central role in determining the allowed classical ground states, below.

We note in passing that the addition of a single-ion anisotropy term $-D(\mathbf{S}\cdot\mathbf{z}_i^{\mathsf{local}})^2$ can easily be included in the analysis by a simple modification of the coefficients a_λ in $\mathcal{H}_{\mathsf{ex}}^{[\mathsf{T_d}]}$ [Eq. (21)], and so do not affect any of the conclusions reached about ground states, below. However, since interactions of this form contribute only to a trivial energy constant for a Kramers doublet, we will not pursue this point further here.

III. ANALYSIS OF CLASSICAL PHASE DIAGRAM FOR $T = 0$

A. General considerations

Given the existence of a classical ground state with $\mathbf{q} = 0$, 4-sublattice order, it is easy to determine a ground-state phase diagram directly from the Hamiltonian $\mathcal{H}_{\mathsf{ex}}^{[\mathsf{T_d}]}$ [Eq. (21)]. The method developed below is quite general and can be applied for arbitrary (J_1, J_2, J_3, J_4). However, for concreteness, we concentrate on the limit

$$J_3 < 0, \quad J_4 \equiv 0, \tag{25}$$

which is of particular relevance to known pyrochlore materials, leading to the phases shown in Figs. 1–3.

The classical ground state of $\mathcal{H}_{\text{ex}}^{[\text{T}_\text{d}]}$ [Eq. (21)] can be found by first identifying the irrep λ^* for which a_{λ^*} takes on the minimum value, and then imposing the constraint on the total length of the spin [Eq. (24)] on $\mathbf{m}_{\lambda^*}$, which implies that

$$m_{\mathsf{A}_2}^2 + \mathbf{m}_{\mathsf{E}}^2 + \mathbf{m}_{\mathsf{T}_2}^2 + \mathbf{m}_{\mathsf{T}_{1,A'}}^2 + \mathbf{m}_{\mathsf{T}_{1,B'}}^2 \equiv \sum_\lambda \mathbf{m}_\lambda^2 = 1. \tag{26}$$

Such an approach is possible because each individual order parameter $\mathbf{m}_\lambda$ can reach a maximum value of unity within physical spin configurations

$$\max \mathbf{m}_\lambda^2 = 1. \tag{27}$$

This method of determining the classical ground state is completely general and, once generalized to the lattice, is not restricted to conventionally ordered states [48,49].

In the limit $J_3 < 0$, $J_4 \equiv 0$, the coefficients a_λ with the lowest values are a_{E}, $a_{\mathsf{T}_{1A'}}$, or a_{T_2}, and the corresponding $\mathbf{q} = 0$ ordered ground states found have E, T_1, and T_2 symmetry. The boundaries between these phases occur where

$$\begin{aligned} a_{\mathsf{T}_2} &= a_{\mathsf{E}} < a_{\mathsf{T}_2},\, a_{\mathsf{T}_{1B'}},\, a_{\mathsf{A}_2} \\ \Rightarrow J_2 &= J_1 > 0, \end{aligned} \tag{28}$$

$$\begin{aligned} a_{\mathsf{T}_2} &= a_{\mathsf{T}_{1,A'}} < a_{\mathsf{E}},\, a_{\mathsf{T}_{1B'}},\, a_{\mathsf{A}_2} \\ \Rightarrow J_2 &= -J_1 > 0, \end{aligned} \tag{29}$$

$$\begin{aligned} a_{\mathsf{E}} &= a_{\mathsf{T}_{1,A'}} < a_{\mathsf{T}_2},\, a_{\mathsf{T}_{1B'}},\, a_{\mathsf{A}_2} \\ \Rightarrow J_2 &= \frac{J_1(4J_1 - 5J_3)}{4J_1 - J_3} < 0, \end{aligned} \tag{30}$$

as illustrated in Fig. 7.

In what follows, we explore the classical ground states with E, T_1, and T_2 symmetry in some detail, paying particular attention to what happens on phase boundaries where more than one order parameter can take on a finite value. We will not consider the all-in, all-out ground state, a simple Ising-type order with two degenerate ground states. All-in, all-out order has a finite value of the order parameter m_{A_2} (cf. Table IV), which requires a_{A_2} to be the lowest coefficient. This only occurs for $J_4 > 0$ and/or $J_3 > 0$, and so falls outside the scope of this article.

B. Noncollinear FM with T_1 symmetry

We begin by considering what happens where interactions are predominantly ferromagnetic (i.e., $J_1, J_2 < 0$), as in $\text{Yb}_2\text{Ti}_2\text{O}_7$ [44]—cf. Table I. For most of this region, as might be expected, the classical configuration with the lowest energy is a state with a finite magnetization. This is the ground state throughout the region bounded by $a_{\mathsf{T}_{1,A'}} = a_{\mathsf{T}_2}$ [Eq. (29)], and $a_{\mathsf{T}_{1,A'}} = a_{\mathsf{E}}$ [Eq. (30)]—cf. Fig. 7. Here the energy is minimized by setting

$$\mathbf{m}_{\mathsf{T}_{1,A'}}^2 = 1 \tag{31}$$

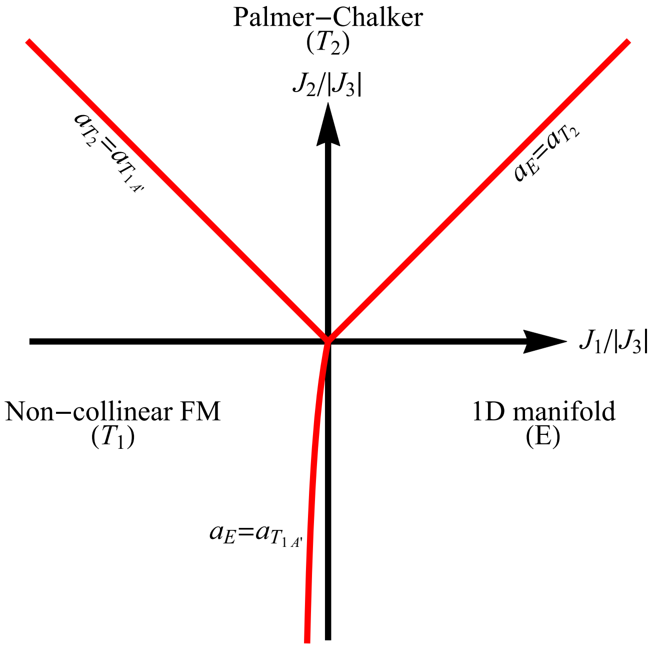

FIG. 7. Classical ground-state phase diagram of $\mathcal{H}_{\text{ex}}$ [Eq. (4)] for $J_3 < 0$, $J_4 = 0$, as a function of $(J_1, J_2)/|J_3|$. In the absence of fluctuations, the ground states are a noncollinear FM transforming with the T_1 irrep of T_d; a one-dimensional manifold of states transforming with the E irrep of T_d; and the Palmer-Chalker phase, a coplanar antiferromagnet transforming with the T_2 irrep of T_d. All three phases have long-range 4-sublattice order. Analytical expressions for the boundaries between phases are given in Eqs. (28)–(30), with coefficients a_λ defined in Table V.

and

$$m_{\mathsf{A}_2} = \mathbf{m}_{\mathsf{E}} = \mathbf{m}_{\mathsf{T}_2} = \mathbf{m}_{\mathsf{T}_{1B'}} = 0. \tag{32}$$

The constraints on the spin lengths [Eq. (24)] further imply that

$$\begin{aligned} m^y_{\mathsf{T}_{1A'}} m^z_{\mathsf{T}_{1A'}} &= 0. \\ m^x_{\mathsf{T}_{1A'}} m^z_{\mathsf{T}_{1A'}} &= 0. \\ m^x_{\mathsf{T}_{1A'}} m^y_{\mathsf{T}_{1A'}} &= 0. \end{aligned} \tag{33}$$

It follows that there are six possible ground states

$$\mathbf{m}_{\mathsf{T}_{1A'}} = \begin{pmatrix} \pm 1 \\ 0 \\ 0 \end{pmatrix}, \begin{pmatrix} 0 \\ \pm 1 \\ 0 \end{pmatrix}, \begin{pmatrix} 0 \\ 0 \\ \pm 1 \end{pmatrix}. \tag{34}$$

Written in terms of spins, these are six, noncollinear ferromagnetic (FM) ground states, with typical spin configuration

$$\begin{aligned} \mathbf{S}_0 &= S\big(\sin\theta_{\mathsf{T}_1}/\sqrt{2}, \sin\theta_{\mathsf{T}_1}/\sqrt{2}, \cos\theta_{\mathsf{T}_1}\big), \\ \mathbf{S}_1 &= S\big(-\sin\theta_{\mathsf{T}_1}/\sqrt{2}, \sin\theta_{\mathsf{T}_1}/\sqrt{2}, \cos\theta_{\mathsf{T}_1}\big), \\ \mathbf{S}_2 &= S\big(\sin\theta_{\mathsf{T}_1}/\sqrt{2}, -\sin\theta_{\mathsf{T}_1}/\sqrt{2}, \cos\theta_{\mathsf{T}_1}\big), \\ \mathbf{S}_3 &= S\big(-\sin\theta_{\mathsf{T}_1}/\sqrt{2}, -\sin\theta_{\mathsf{T}_1}/\sqrt{2}, \cos\theta_{\mathsf{T}_1}\big), \end{aligned} \tag{35}$$

where θ_{T_1} is given by Eq. (20) and, following Eq. (22), $S = 1/2$.

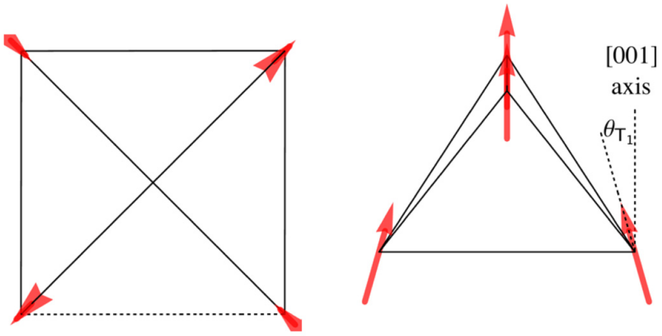

(a) (b)

FIG. 8. Spin configuration in the 4-sublattice noncollinear FM phase, transforming with the T_1 irrep of T_d: (a) viewed along the [001] axis; and (b) viewed slightly off the [110] axis. The magnetization is aligned with the [001] axis. Spins are canted into the plane perpendicular to this, with canting angle θ_{T_1}. The canting is of an icelike form such that the projection of the spin configuration onto a [001] plane has two spins oriented into the tetrahedron and two oriented out, as shown in (a).

The magnetization of this FM ground state, illustrated in Fig. 8, is parallel to a [001] axis, with spins canted away from this axis, in an icelike manner. This state has been identified as the ground state in $Yb_2Sn_2O_7$, where it was referred to as a "splayed FM" [36], and in most samples of $Yb_2Ti_2O_7$ which order at low temperature [24,66,68–73] although a different form of canting has recently been claimed in Ref. [74]. It is also the observed ordered state of the Tb based pyrochlore $Tb_2Sn_2O_7$ [75,76].

C. One-dimensional manifold of states with E symmetry

For a wide range of parameters, predominantly with antiferromagnetic XY interactions $J_1 > 0$, the classical ground state of $\mathcal{H}_{\mathsf{ex}}^{[\mathsf{T_d}]}$ [Eq. (21)] is a one-dimensional manifold of states which transforms with the E irrep of T_d (Fig. 9). These ground states occur in a region bounded by $a_{\mathsf{E}} = a_{\mathsf{T}_{1,A'}}$ [Eq. (30)] and $a_{\mathsf{E}} = a_{\mathsf{T}_2}$ [Eq. (28)]—cf. Fig. 7—and is characterized by spins lying in the XY plane normal to the local [111] axis on each site [cf. Eqs. (A2)–(A4)].

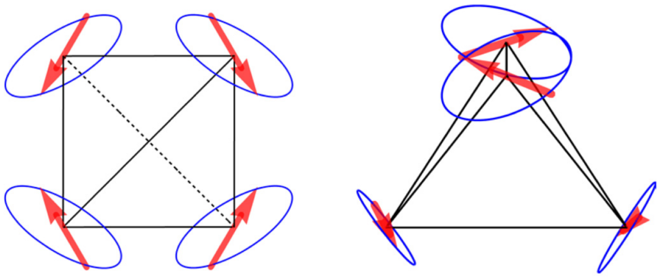

(a) (b)

FIG. 9. Example of a spin configuration within the one-dimensional manifold of states transforming with the E irrep of T_d: (a) viewed along [001] axis; and (b) viewed slightly off the [110] axis. The manifold possesses 4-sublattice long-range order, with spins lying in the "XY" plane perpendicular to the local [111] axis at each site. The manifold is continuous, and can be parametrized with a single angle θ_{E}. The manifold can be generated by a clockwise rotation of all spins around their respective local axes.

For this range of parameters, the classical ground state energy can be minimized by setting

$$\mathbf{m}_{\mathsf{E}}^2 = 1 \tag{36}$$

and

$$m_{\mathsf{A}_2} = \mathbf{m}_{\mathsf{T}_2} = \mathbf{m}_{\mathsf{T}_{1A'}} = \mathbf{m}_{\mathsf{T}_{1B'}} = 0. \tag{37}$$

These solutions *automatically* satisfy the constraint on the total length of the spin Eq. (24) and are conveniently characterized by writing

$$\mathbf{m}_{\mathsf{E}} = (\cos\theta_{\mathsf{E}},\ \sin\theta_{\mathsf{E}}). \tag{38}$$

It follows that the ground state is a continuous, one-dimensional manifold of states parametrized by the single angle $0 \leqslant \theta_{\mathsf{E}} < 2\pi$. The spin configuration in this manifold is given by

$$\begin{aligned}
\mathbf{S}_0 &= S\left[\sqrt{\frac{2}{3}}\cos(\theta_{\mathsf{E}}), \sqrt{\frac{2}{3}}\cos\left(\theta_{\mathsf{E}} + \frac{2\pi}{3}\right),\right.\\
&\qquad\left.\sqrt{\frac{2}{3}}\cos\left(\theta_{\mathsf{E}} - \frac{2\pi}{3}\right)\right]\\
\mathbf{S}_1 &= S\left[\sqrt{\frac{2}{3}}\cos(\theta_{\mathsf{E}}),\ -\sqrt{\frac{2}{3}}\cos\left(\theta_{\mathsf{E}} + \frac{2\pi}{3}\right),\right.\\
&\qquad\left.-\sqrt{\frac{2}{3}}\cos\left(\theta_{\mathsf{E}} - \frac{2\pi}{3}\right)\right]\\
\mathbf{S}_2 &= S\left[-\sqrt{\frac{2}{3}}\cos(\theta_{\mathsf{E}}), \sqrt{\frac{2}{3}}\cos\left(\theta_{\mathsf{E}} + \frac{2\pi}{3}\right),\right.\\
&\qquad\left.-\sqrt{\frac{2}{3}}\cos\left(\theta_{\mathsf{E}} - \frac{2\pi}{3}\right)\right]\\
\mathbf{S}_3 &= S\left[-\sqrt{\frac{2}{3}}\cos(\theta_{\mathsf{E}}),\ -\sqrt{\frac{2}{3}}\cos\left(\theta_{\mathsf{E}} + \frac{2\pi}{3}\right),\right.\\
&\qquad\left.\sqrt{\frac{2}{3}}\cos\left(\theta_{\mathsf{E}} - \frac{2\pi}{3}\right)\right],
\end{aligned} \tag{39}$$

with spins lying in the local XY plane [cf. Eqs. (A3) and (A4)].

D. Noncoplanar antiferromagnet Ψ_2 with E symmetry

It is now well established that in $Er_2Ti_2O_7$ quantum fluctuations [26,27,46], classical thermal fluctuations at low temperature [25] and thermal fluctuations near the ordering temperature [28,77] fluctuations all act within the one-dimensional manifold of classical ground states described in Sec. III C, to select a noncoplanar antiferromagnet Ψ_2, illustrated in Fig. 10. Structural disorder, meanwhile, favors the coplanar antiferromagnet Ψ_3 [78,79], illustrated in Fig. 11. Together, this pair of states form a basis for the E irrep of T_d [65].

The Ψ_2 ground state is sixfold degenerate, with spins canted symmetrically out of the [100] plane. The six spin configurations for Ψ_2 states are given by Eq. (39) with $\theta_{\mathsf{E}} = \frac{n\pi}{3}$, $n = 0,1,2,\ldots,5$. The Ψ_2 state is characterized by the primary order parameter $\mathbf{m}_{\mathsf{E}}$ (cf. Table III), and by $c_{\mathsf{E}} > 0$,

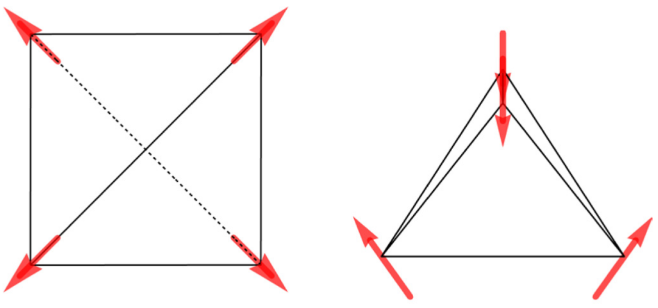
(a) (b)

FIG. 10. Spin configuration in the 4-sublattice noncoplanar antiferromagnet Ψ_2, selected by fluctuations from the one-dimensional manifold of states transforming with E: (a) viewed along [001] axis; and (b) viewed slightly off the [110] axis. At the phase boundary with the Palmer-Chalker phase, each of the six Ψ_2 ground states can be transformed continuously into a Palmer-Chalker state without leaving the ground-state manifold.

where (cf. Refs. [77,80])

$$c_{\mathsf{E}} = \langle \cos 6\theta_{\mathsf{E}} \rangle. \tag{40}$$

Symmetry allows for fluctuations to induce a finite value of m_{A_2} in the Ψ_2 state [81], but classically this must vanish as $T \to 0$ since the energy is minimized by $m_{\mathsf{A}_2} = 0$ within the region of phase diagram which favors the Ψ_2 state.

E. Coplanar antiferromagnet Ψ_3 with E symmetry

For parameters bordering on the noncollinear FM phase, fluctuations select a coplanar antiferromagnet Ψ_3 from the one-dimensional manifold of states transforming with E. The Ψ_3 ground state is sixfold degenerate, with spins lying in a common [100] plane.

The six spin configurations for Ψ_3 states are given by Eq. (39) with $\theta_{\mathsf{E}} = \frac{(2n+1)\pi}{6}$, $n = 0,1,2,\ldots,5$. These states are characterized by a finite value of the order parameter $\mathbf{m}_{\mathsf{E}}$ (cf Table III), and by $c_{\mathsf{E}} < 0$ [cf. Eq. (40)]. An example of a typical spin configuration is shown in Fig. 11.

Taken together Ψ_2 and Ψ_3 form a complete basis for the E irrep of T_d.

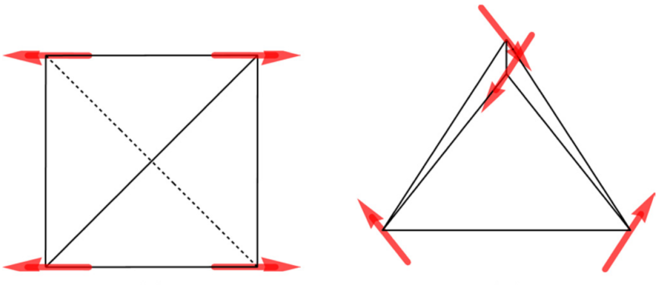
(a) (b)

FIG. 11. Spin configuration in the 4-sublattice coplanar antiferromagnet Ψ_3, selected by fluctuations from the one-dimensional manifold of states transforming with E: (a) viewed along [001] axis; and (b) viewed slightly off the [110] axis. At the phase boundary with the noncollinear FM phase, each of the six Ψ_3 ground states can be transformed continuously into a noncollinear FM state, without leaving the ground-state manifold.

F. Palmer-Chalker phase Ψ_4 with T_2 symmetry

In a region bounded by $a_{\mathsf{T}_2} = a_{\mathsf{T}_{1,\mathsf{A}'}}$ [Eq. (29)] and $a_{\mathsf{T}_2} = a_{\mathsf{E}}$ [Eq. (28)]—cf. Fig. 7—the energy is minimized by setting

$$\mathbf{m}_{\mathsf{T}_2}^2 = 1 \tag{41}$$

and

$$m_{\mathsf{A}_2} = \mathbf{m}_{\mathsf{E}} = \mathbf{m}_{\mathsf{T}_{1\mathsf{A}'}} = \mathbf{m}_{\mathsf{T}_{1\mathsf{B}'}} = 0. \tag{42}$$

The constraints on the total length of the spin, Eq. (24), further imply that

$$\mathbf{m}_{\mathsf{T}_2}^2 = 1, \tag{43}$$

$$m_{\mathsf{T}_2}^y m_{\mathsf{T}_2}^z = 0, \tag{44}$$

$$m_{\mathsf{T}_2}^x m_{\mathsf{T}_2}^z = 0, \tag{45}$$

$$m_{\mathsf{T}_2}^x m_{\mathsf{T}_2}^y = 0, \tag{46}$$

giving us a set of six ground states

$$\mathbf{m}_{\mathsf{T}_2} = \begin{pmatrix} \pm 1 \\ 0 \\ 0 \end{pmatrix}, \begin{pmatrix} 0 \\ \pm 1 \\ 0 \end{pmatrix}, \begin{pmatrix} 0 \\ 0 \\ \pm 1 \end{pmatrix}. \tag{47}$$

Within these ground states, spins are arranged in helical manner in a common [100] plane, with a typical spin configuration given by (see Fig. 12)

$$\begin{aligned}
\mathbf{S}_0 &= S\left(\frac{1}{\sqrt{2}},-\frac{1}{\sqrt{2}},0\right),\\
\mathbf{S}_1 &= S\left(-\frac{1}{\sqrt{2}},-\frac{1}{\sqrt{2}},0\right),\\
\mathbf{S}_2 &= S\left(\frac{1}{\sqrt{2}},\frac{1}{\sqrt{2}},0\right),\\
\mathbf{S}_3 &= S\left(-\frac{1}{\sqrt{2}},\frac{1}{\sqrt{2}},0\right).
\end{aligned} \tag{48}$$

This phase is the "Palmer-Chalker" phase, first identified as the ground state of a model with antiferromagnetic nearest-neighbor Heisenberg interactions and long-range dipolar interactions on the pyrochlore lattice [47]. The six degenerate

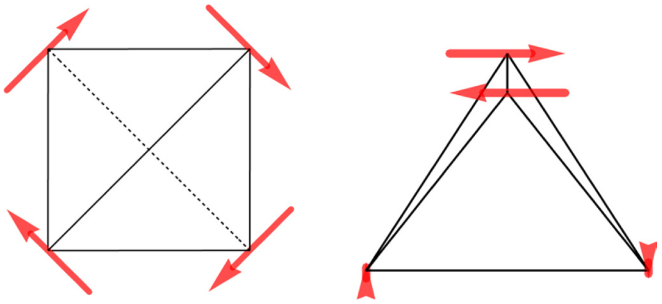
(a) (b)

FIG. 12. Spin configuration in the 4-sublattice Palmer-Chalker phase Ψ_4 transforming with the T_2 irrep of T_d: (a) viewed along [001] axis; and (b) viewed slightly off the [110] axis. At the phase boundary with the Ψ_2 phase, each of the six Palmer-Chalker ground states can be transformed continuously into a Ψ_2 state.

ground states in this phase are described by the basis vectors $\Psi_{4,5,6}$ [65], which are all equivalent by symmetry. For brevity we refer to this phase as Ψ_4, but it should be remembered that all three basis vectors $\Psi_{4,5,6}$ are equivalent ground states.

The Palmer-Chalker states are superficially similar to the Ψ_3 states (Sec. III E), being coplanar, antiferromagnet configurations with all spins lying in a [100] plane. However, their symmetry properties are quite different (as is expressed in the fact that they transform according to different irreps of T_d). A simple example of these different symmetry properties is their behavior under the three C_2 rotations around $\langle 100\rangle$ axes. The Ψ_3 configurations are invariant under all such rotations. The PC states are invariant under one such rotation (the one around the axis normal to all the spins), but reverse all spin orientations under the other two.

G. Boundary between Palmer-Chalker phase and the one-dimensional manifold of states with E symmetry

The boundary between the Palmer-Chalker phase and the one-dimensional manifold of states with E symmetry occurs when $a_{\mathsf{E}} = a_{\mathsf{T}_2}$ [cf. Eq. (28)]. In this case, $\mathcal{H}^{[\mathsf{T_d}]}_{\mathsf{ex}}$ [Eq. (21)] is minimized by setting

$$\mathbf{m}^2_{\mathsf{E}} + \mathbf{m}^2_{\mathsf{T}_2} = 1 \tag{49}$$

and

$$m_{\mathsf{A}_2} = \mathbf{m}_{\mathsf{T}_{1A'}} = \mathbf{m}_{\mathsf{T}_{1B'}} = 0. \tag{50}$$

Substituting

$$\mathbf{m}_{\mathsf{E}} = m_{\mathsf{E}}(\cos\theta_{\mathsf{E}},\ \sin\theta_{\mathsf{E}}), \tag{51}$$

and imposing the constraint Eq. (24), we find

$$\begin{aligned}2m_{\mathsf{E}}m^x_{\mathsf{T}_2}\sin(\theta_{\mathsf{E}}) - m^y_{\mathsf{T}_2}m^z_{\mathsf{T}_2} &= 0,\\ 2m_{\mathsf{E}}m^y_{\mathsf{T}_2}\sin\left(\theta_{\mathsf{E}} - \frac{2\pi}{3}\right) - m^x_{\mathsf{T}_2}m^z_{\mathsf{T}_2} &= 0,\\ 2m_{\mathsf{E}}m^z_{\mathsf{T}_2}\sin\left(\theta_{\mathsf{E}} + \frac{2\pi}{3}\right) - m^x_{\mathsf{T}_2}m^y_{\mathsf{T}_2} &= 0.\end{aligned} \tag{52}$$

It is easy to show that there are no solutions to Eqs. (52) where more than one component of $\mathbf{m}_{\mathsf{T}_2}$ is finite. There are, however, three distinct one-dimensional manifolds which connect pairs of Palmer-Chalker states to the one-dimensional manifold of E-symmetry states:

$$\mathbf{m}_{\mathsf{E}} = \cos(\alpha)\begin{pmatrix}1\\0\end{pmatrix},\quad \mathbf{m}_{\mathsf{T}_2} = \sin(\alpha)\begin{pmatrix}1\\0\\0\end{pmatrix}, \tag{53}$$

$$\mathbf{m}_{\mathsf{E}} = \cos(\beta)\begin{pmatrix}-\frac{1}{2}\\ \frac{\sqrt{3}}{2}\end{pmatrix},\quad \mathbf{m}_{\mathsf{T}_2} = \sin(\beta)\begin{pmatrix}0\\1\\0\end{pmatrix}, \tag{54}$$

$$\mathbf{m}_{\mathsf{E}} = \cos(\gamma)\begin{pmatrix}-\frac{1}{2}\\ -\frac{\sqrt{3}}{2}\end{pmatrix},\quad \mathbf{m}_{\mathsf{T}_2} = \sin(\gamma)\begin{pmatrix}0\\0\\1\end{pmatrix}, \tag{55}$$

where the angles α, β, and γ run from 0 to 2π.

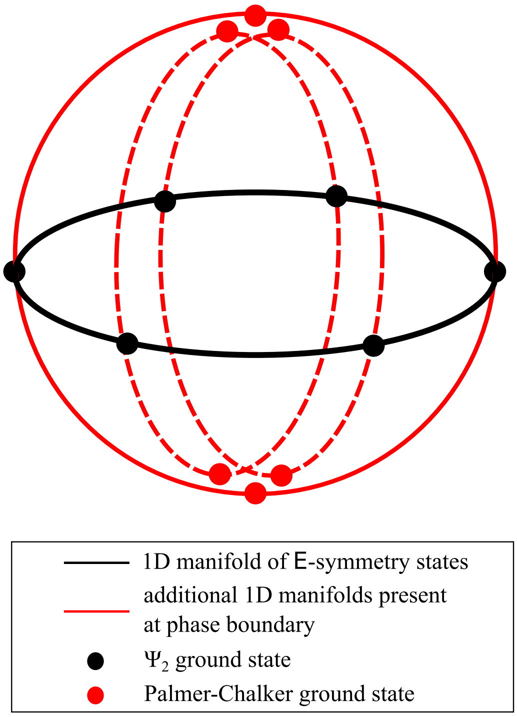

FIG. 13. Structure of the ground-state manifold at the boundary between the Palmer-Chalker (PC) phase and the one-dimensional manifold of states with E symmetry. The black circle denotes the manifold of E-symmetry ground states, including the six Ψ_2 ground states (black dots). At the boundary with the PC phase, this manifold branches at the Ψ_2 states, to connect with three, additional, one-dimensional manifolds. These manifolds in turn interpolate to the six Palmer-Chalker ground states with T_2 symmetry (red dots). An exactly equivalent picture holds on the boundary between the noncollinear ferromagnet (FM), and the one-dimensional manifold of states with E symmetry. However, in this case the different manifolds intersect at the Ψ_3 states.

A typical spin configuration for one of the three connecting manifolds is

$$\begin{aligned}\mathbf{S}_0 &= S\sqrt{\frac{2}{3}}\left[-\cos(\alpha),\ \cos\left(\alpha+\frac{\pi}{3}\right),\ \cos\left(\alpha-\frac{\pi}{3}\right)\right],\\ \mathbf{S}_1 &= S\sqrt{\frac{2}{3}}\left[-\cos(\alpha),\ -\cos\left(\alpha+\frac{\pi}{3}\right),\ -\cos\left(\alpha-\frac{\pi}{3}\right)\right],\\ \mathbf{S}_2 &= S\sqrt{\frac{2}{3}}\left[\cos(\alpha),\ \cos\left(\alpha-\frac{\pi}{3}\right),\ -\cos\left(\alpha+\frac{\pi}{3}\right)\right],\\ \mathbf{S}_3 &= S\sqrt{\frac{2}{3}}\left[\cos(\alpha),\ -\cos\left(\alpha-\frac{\pi}{3}\right),\ \cos\left(\alpha+\frac{\pi}{3}\right)\right],\end{aligned} \tag{56}$$

where $\alpha = 0,\ \pi$ correspond to the Ψ_2 ground states with $\theta_{\mathsf{E}} = 0,\ \pi$, and $\alpha = \pi/2,\ 3\pi/2$ correspond to two of the six Palmer-Chalker ground states. These manifolds are illustrated in Fig. 13.

By application of the Lego-brick rules given in Sec. II E, the ground-state degeneracy on this phase boundary must be at least $O(2^{L^2})$. This follows from the fact that, on the boundary, the Palmer-Chalker ground states Ψ_4 share two spin orientations with the neighboring Ψ_3 configuration.

This, in turn, is connected with the $O(L^2)$ number of zero modes appearing in spin-wave expansions around the Ψ_2 configurations at this boundary (cf. Sec. IV B).

We note that a special case of this phase boundary is studied for pure XY spins (i.e., with infinite easy-plane anisotropy) in Ref. [82], finding the same structure of ground-state manifolds.

H. Boundary between the noncollinear ferromagnet and the one-dimensional manifold of states with E symmetry

The boundary between the noncollinear ferromagnet and the one-dimensional manifold of states with E symmetry occurs when $a_{\mathsf{E}} = a_{\mathsf{T}_{1,\mathsf{A}'}}$ [cf. Eq. (30)]. In this case, $\mathcal{H}_{\mathsf{ex}}^{[\mathsf{T_d}]}$ [Eq. (21)] is minimized by setting

$$\mathbf{m}^2_{\mathsf{T}_{1,\mathsf{A}'}} + \mathbf{m}^2_{\mathsf{E}} = 1 \tag{57}$$

and

$$m_{\mathsf{A}_2} = \mathbf{m}_{\mathsf{T}_{1,\mathsf{B}'}} = \mathbf{m}_{\mathsf{T}_2} = 0. \tag{58}$$

Defining, for the sake of brevity, the quantities

$$\begin{aligned}\mu(\theta_{\mathsf{T}_1}) &= \left[\sqrt{2}\cos\left(\theta_{\mathsf{T}_1}\right) - \sin\left(\theta_{\mathsf{T}_1}\right)\right],\\ \nu(\theta_{\mathsf{T}_1}) &= \left[\,\sin\left(\theta_{\mathsf{T}_1}\right)^2 + \sqrt{2}\sin\left(2\theta_{\mathsf{T}_1}\right)\right],\end{aligned} \tag{59}$$

and imposing the constraint Eq. (24) we obtain

$$\begin{aligned}2m_{\mathsf{E}}m^x_{\mathsf{T}_{1,\mathsf{A}'}}\cos(\theta_{\mathsf{E}}) &= -\frac{\mu\left(\theta_{\mathsf{T}_{1,\mathsf{A}'}}\right)}{\nu\left(\theta_{\mathsf{T}_{1,\mathsf{A}'}}\right)}m^y_{\mathsf{T}_{1,\mathsf{A}'}}m^z_{\mathsf{T}_{1,\mathsf{A}'}},\\ 2m_{\mathsf{E}}m^y_{\mathsf{T}_{1,\mathsf{A}'}}\cos\left(\theta_{\mathsf{E}} - \frac{2\pi}{3}\right) &= -\frac{\mu\left(\theta_{\mathsf{T}_{1,\mathsf{A}'}}\right)}{\nu\left(\theta_{\mathsf{T}_{1,\mathsf{A}'}}\right)}m^x_{\mathsf{T}_{1,\mathsf{A}'}}m^z_{\mathsf{T}_{1,\mathsf{A}'}},\\ 2m_{\mathsf{E}}m^z_{\mathsf{T}_{1,\mathsf{A}'}}\cos\left(\theta_{\mathsf{E}} + \frac{2\pi}{3}\right) &= -\frac{\mu\left(\theta_{\mathsf{T}_{1,\mathsf{A}'}}\right)}{\nu\left(\theta_{\mathsf{T}_{1,\mathsf{A}'}}\right)}m^x_{\mathsf{T}_{1,\mathsf{A}'}}m^y_{\mathsf{T}_{1,\mathsf{A}'}},\end{aligned} \tag{60}$$

where θ_{T_1} is the (fixed) canting angle [Eq. (20)] and θ_{E} is the (variable) angle within the $U(1)$ manifold [Eq. (38)]. For the parameters considered here, the quantities $\mu(\theta_{\mathsf{T}_1})$ and $\nu(\theta_{\mathsf{T}_1})$ are always finite.

Arguments identical to those developed for the boundary with the Palmer-Chalker phase, give us three further 1D manifolds in addition to that associated with the E phase. However the intersections of the manifolds are now located at $\theta_{\mathsf{E}} = \frac{(2n+1)\pi}{6}$, corresponding to the Ψ_3 states. This explains the model's general entropic preference for Ψ_3 states in the region proximate to the ferromagnetic phase.

A typical spin configuration for one of the three connecting manifolds, parametrized by an angle η is

$$\begin{aligned}\mathbf{S}_0 = S\Bigg(&\cos\left(\theta_{\mathsf{T}_1}\right)\sin(\eta),\ \frac{1}{\sqrt{2}}\left[-\cos(\eta) + \sin(\eta)\sin\left(\theta_{\mathsf{T}_1}\right)\right],\\ &\frac{1}{\sqrt{2}}\left[\,\cos(\eta) + \sin(\eta)\sin\left(\theta_{\mathsf{T}_1}\right)\right]\Bigg),\\ \mathbf{S}_1 = S\Bigg(&\cos\left(\theta_{\mathsf{T}_1}\right)\sin(\eta),\ \frac{1}{\sqrt{2}}\left[\,\cos(\eta) - \sin(\eta)\sin\left(\theta_{\mathsf{T}_1}\right)\right],\\ &\frac{1}{\sqrt{2}}\left[-\cos(\eta) - \sin(\eta)\sin\left(\theta_{\mathsf{T}_1}\right)\right]\Bigg),\\ \mathbf{S}_2 = S\Bigg(&\cos\left(\theta_{\mathsf{T}_1}\right)\sin(\eta),\ \frac{1}{\sqrt{2}}\left[-\cos(\eta) - \sin(\eta)\sin\left(\theta_{\mathsf{T}_1}\right)\right],\\ &\frac{1}{\sqrt{2}}\left[-\cos(\eta) + \sin(\eta)\sin\left(\theta_{\mathsf{T}_1}\right)\right]\Bigg),\\ \mathbf{S}_3 = S\Bigg(&\cos\left(\theta_{\mathsf{T}_1}\right)\sin(\eta),\ \frac{1}{\sqrt{2}}\left[\,\cos(\eta) + \sin(\eta)\sin\left(\theta_{\mathsf{T}_1}\right)\right],\\ &\frac{1}{\sqrt{2}}\left[\,\cos(\eta) - \sin(\eta)\sin\left(\theta_{\mathsf{T}_1}\right)\right]\Bigg).\end{aligned} \tag{61}$$

Here $\eta = 0$ corresponds to the Ψ_3 ground state with $\theta_{\mathsf{E}} = \pi/2$, and $\eta = \pi/2$ to one of the six FM ground states.

We note that an equivalent ground-state manifold was discussed by Canals and co-authors [83], and later by Chern [80], in the context the Heisenberg antiferromagnet with Dzyaloshinskii-Moriya interactions on the pyrochlore lattice. This case corresponds to a single point on the phase boundary considered here.

I. Boundary between the Palmer-Chalker phase and the noncollinear ferromagnet

The boundary between the Palmer-Chalker phase and the noncollinear ferromagnet occurs when $a_{\mathsf{T}_2} = a_{\mathsf{T}_{1,\mathsf{A}'}}$ [cf. Eq. (29)]. In this case, $\mathcal{H}_{\mathsf{ex}}^{[\mathsf{T_d}]}$ [Eq. (21)] is minimized by setting

$$\mathbf{m}^2_{\mathsf{T}_2} + \mathbf{m}^2_{\mathsf{T}_{1,\mathsf{A}'}} = 1 \tag{62}$$

and

$$m_{\mathsf{A}_2} = \mathbf{m}_{\mathsf{E}} = \mathbf{m}_{\mathsf{T}_{1,\mathsf{B}'}} = 0. \tag{63}$$

Imposing the constraint Eq. (24) we obtain

$$\begin{aligned}&-m^y_{\mathsf{T}_2}m^z_{\mathsf{T}_2} + \left[\,\sin\left(\theta_{\mathsf{T}_1}\right)^2 + \sqrt{2}\sin\left(2\theta_{\mathsf{T}_1}\right)\right]m^y_{\mathsf{T}_{1\mathsf{A}'}}m^z_{\mathsf{T}_{1\mathsf{A}'}}\\ &+\left[\sqrt{2}\cos\left(\theta_{\mathsf{T}_1}\right) - \sin\left(\theta_{\mathsf{T}_1}\right)\right]\left(\mathbf{m}_{\mathsf{T}_{1\mathsf{A}'}} \times \mathbf{m}_{\mathsf{T}_2}\right)_x = 0\\ &-m^x_{\mathsf{T}_2}m^z_{\mathsf{T}_2} + \left[\,\sin\left(\theta_{\mathsf{T}_1}\right)^2 + \sqrt{2}\sin\left(2\theta_{\mathsf{T}_1}\right)\right]m^x_{\mathsf{T}_{1\mathsf{A}'}}m^z_{\mathsf{T}_{1\mathsf{A}'}}\\ &+\left[(\sqrt{2}\cos\left(\theta_{\mathsf{T}_1}\right) - \sin\left(\theta_{\mathsf{T}_1}\right)\right]\left(\mathbf{m}_{\mathsf{T}_{1\mathsf{A}'}} \times \mathbf{m}_{\mathsf{T}_2}\right)_y = 0\\ &-m^x_{\mathsf{T}_2}m^y_{\mathsf{T}_2} + \left[\,\sin\left(\theta_{\mathsf{T}_1}\right)^2 + \sqrt{2}\sin\left(2\theta_{\mathsf{T}_1}\right)\right]m^x_{\mathsf{T}_{1\mathsf{A}'}}m^y_{\mathsf{T}_{1\mathsf{A}'}}\\ &+\left[(\sqrt{2}\cos\left(\theta_{\mathsf{T}_1}\right) - \sin\left(\theta_{\mathsf{T}_1}\right)\right]\left(\mathbf{m}_{\mathsf{T}_{1\mathsf{A}'}} \times \mathbf{m}_{\mathsf{T}_2}\right)_z = 0.\end{aligned} \tag{64}$$

where θ_{T_1} is defined in Eq. (20).

In general, the ground-state manifold on the boundary of the Palmer-Chalker phase is locally two dimensional. To establish this, we consider small deviations from a given solution

$$\begin{aligned}\mathbf{m}_{\mathsf{T}_2} &= \mathbf{m}^0_{\mathsf{T}_2} + \delta\mathbf{m}_{\mathsf{T}_2},\\ \mathbf{m}_{\mathsf{T}_{1\mathsf{A}'}} &= \mathbf{m}^0_{\mathsf{T}_{1\mathsf{A}'}} + \delta\mathbf{m}_{\mathsf{T}_{1\mathsf{A}'}},\end{aligned} \tag{65}$$

and expand the constraint Eq. (64) to linear order in $\delta\mathbf{m}$. Generally, we find two linearly independent solutions for $(\delta\mathbf{m}_{\mathsf{T}_2},\delta\mathbf{m}_{\mathsf{T}_{1\mathsf{A}'}})$, and the manifold in the vicinity of $(\mathbf{m}^0_{\mathsf{T}_2},\mathbf{m}^0_{\mathsf{T}_{1\mathsf{A}'}})$ is two dimensional.

However if we expand around a state $(\tilde{\mathbf{m}}^0_{\mathsf{T}_2},\tilde{\mathbf{m}}^0_{\mathsf{T}_{1\mathsf{A}'}})$ where *both* order parameters are aligned with the same cubic axis, e.g.,

$$\tilde{m}^{0y}_{\mathsf{T}_2} = \tilde{m}^{0z}_{\mathsf{T}_2} = \tilde{m}^{0y}_{\mathsf{T}_{1\mathsf{A}'}} = \tilde{m}^{0z}_{\mathsf{T}_{1\mathsf{A}'}} = 0, \tag{66}$$

one of the Eqs. (64) is satisfied trivially, leaving only three constraints on six variables. It follows that the manifold is locally three dimensional in the vicinity of $(\tilde{\mathbf{m}}^0_{\mathsf{T}_2}, \tilde{\mathbf{m}}^0_{\mathsf{T}_{1\mathsf{A}'}})$.

This set of ground states on the tetrahedron includes multiple states where one of the spins has the same direction. Applying the Lego-brick rules, described in Sec. II E, this means that neighboring kagome planes can be effectively decoupled in the ground state and there is a ground-state degeneracy on the lattice of at least $O(2^L)$.

J. All-in, all-out order with A_2 symmetry

In Secs. III B–III F we have explicitly discussed the different types of ordered, classical ground state which occur for $J_3 < 0, J_4 = 0$. For a more general choice of parameters, with $J_4 > 0$ or $J_3 > 0$, it is possible to find situations where the lowest parameter in $\mathcal{H}^{\mathsf{tet}}_{\mathsf{ex}}$ [Eq. (21)] is a_{A_2}. In this case, the ground state will have 4-sublattice order with a finite value of the order parameter m_{A_2} (Table III). As can be seen from the definition of the order parameter, this type of order is particularly simple, with all spins aligned along the local [111] axes, and all spins pointing either into, or out of, tetrahedra on the A sublattice. This type of order is commonly referred to as all-in, all-out and is observed in some pyrochlore magnets, including $\mathrm{Nd_2Zr_2O_7}$ [84].

Since this type of order does not occur for $J_3 < 0, J_4 = 0$, we will not discuss it further here. However, we note that the order parameter m_{A_2} is a scalar, and that finite-temperature phase transitions are therefore expected to fall into the Ising universality class, in the absence of a first order phase transition.

IV. THEORY OF CLASSICAL AND QUANTUM SPIN-WAVE EXCITATIONS

In order to complete the classical phase diagram described in Sec. III, it is necessary to understand how quantum and/or classical fluctuations select between the one-dimensional manifold of states described by $\mathbf{m}_{\mathsf{E}}$. At low temperatures, this can be accomplished by exploring the way in which spin-wave excitations contribute to the free energy. Knowledge of the spin-wave excitations also makes it possible to make predictions for inelastic neutron scattering, discussed below, and to benchmark the results of the classical Monte Carlo simulations described in Sec. V.

In what follows, we describe a general theory of classical and quantum spin-wave excitations about the different ordered states described in Sec. III. In Sec. IV A we establish a classical, low-temperature spin-wave expansion, which makes it possible to determine the boundary between the Ψ_2 and Ψ_3 ground states for classical spins in the limit $T \to 0$ (cf. Fig. 1). In Sec. IV C we develop an equivalent quantum theory, within the linear spin-wave approximation, which allows us to estimate the boundary between the Ψ_2 and Ψ_3 ground states for quantum spins in the limit $T \to 0$ (cf. Fig. 2). We find that the high degeneracies at classical phase boundaries, described in Sec. III, strongly enhance quantum fluctuations, and in some cases eliminate the ordered moment entirely. In Sec. IV D we show how both classical and quantum spin-wave theories can be used to make predictions for inelastic neutron scattering. Readers interested in the relationship between classical and quantum spin-wave theories are referred to the discussion in Ref. [85].

A. Classical spin-wave expansion

To obtain the low-energy excitations around the ordered ground states of $\mathcal{H}_{\mathsf{ex}}$ [Eq. (4)] we use a description in terms of classical spin waves, analogous to that described in Ref. [86]. We begin by defining a local coordinate system by introducing a set of orthogonal unit vectors $\{\mathbf{u}_i, \mathbf{v}_i, \mathbf{w}_i\}$ for each of the four sublattices $i = 0,1,2,3$ (cf. Fig. 5). The local "z-axis" $\mathbf{w}_i$ is chosen to be aligned with the spins in a given 4-sublattice ground state

$$\mathbf{S}_i = S\mathbf{w}_i \quad \forall\, i. \tag{67}$$

The remaining unit vectors $\mathbf{u}_i$ and $\mathbf{v}_i$ are only determined up to a rotation about $\mathbf{w}_i$, and any convenient choice can be made.

Using this basis, the fluctuations of the spin $\mathbf{S}_{ik}$ on sublattice i of tetrahedron k can be parametrized as

$$\mathbf{S}_{ik} = \begin{pmatrix} \sqrt{S}\delta u_{ik} \\ \sqrt{S}\delta v_{ik} \\ \sqrt{S^2 - S\delta u_{ik}^2 - S\delta v_{ik}^2} \end{pmatrix} \approx \begin{pmatrix} \sqrt{S}\delta u_{ik} \\ \sqrt{S}\delta v_{\vec{i}k} \\ S - \frac{1}{2}\delta u_{ik}^2 - \frac{1}{2}\delta v_{ik}^2 \end{pmatrix}. \tag{68}$$

Substituting Eq. (68) into $\mathcal{H}_{\mathsf{ex}}$ [Eq. (4)] we obtain

$$\mathcal{H}_{\mathsf{ex}} = \sum_{\mathsf{tet}\ k} \sum_{i<j} \mathbf{S}_{ik} \cdot \mathbf{J}_{ij} \cdot \mathbf{S}_{jk} = \mathcal{E}_0 + \mathcal{H}^{\mathsf{CSW}}_{\mathsf{ex}} + \cdots, \tag{69}$$

where

$$\mathcal{E}_0 = \frac{NS^2}{4} \sum_{i,j=0}^{3} \mathbf{w}_i \cdot \mathbf{J}_{ij} \cdot \mathbf{w}_j \tag{70}$$

is the classical ground-state energy of the chosen 4-sublattice state, and

$$\mathcal{H}^{\mathsf{CSW}}_{\mathsf{ex}} = \frac{S}{2} \sum_{k} \sum_{i,j=0}^{3} \times \Big[-\frac{1}{2}(\delta u_{ik}^2 + \delta u_{jk}^2 + \delta v_{ik}^2 + \delta v_{jk}^2)(\mathbf{w}_i \cdot \mathbf{J}_{ij} \cdot \mathbf{w}_j) + \delta u_{ik}\delta u_{jk}(\mathbf{u}_i \cdot \mathbf{J}_{ij} \cdot \mathbf{u}_j) + \delta v_{ik}\delta v_{jk}(\mathbf{v}_i \cdot \mathbf{J}_{ij} \cdot \mathbf{v}_j) + \delta u_{ik}\delta v_{jk}(\mathbf{u}_i \cdot \mathbf{J}_{ij} \cdot \mathbf{v}_j) + \delta v_{ik}\delta u_{jk}(\mathbf{v}_i \cdot \mathbf{J}_{ij} \cdot \mathbf{u}_j) \Big] \tag{71}$$

describes the leading effect of (classical) fluctuations about this state. Performing a Fourier transformation we find

$$\mathcal{H}_{\mathsf{ex}} = \frac{NS^2}{4} \sum_{i,j=0}^{3} \mathbf{w}_i \cdot \mathbf{J}_{ij} \cdot \mathbf{w}_j + \frac{1}{2} \sum_{\mathbf{q}} \tilde{u}(-\mathbf{q})^T \cdot \mathbf{M}(\mathbf{q}) \cdot \tilde{u}(\mathbf{q}). \tag{72}$$

Here $\tilde{u}(\mathbf{q})$ is the vector

$$\begin{aligned}\tilde{u}(\mathbf{q}) = (&\delta u_0(\mathbf{q}),\delta u_1(\mathbf{q}),\delta u_2(\mathbf{q}),\delta u_3(\mathbf{q}),\\ &\delta v_0(\mathbf{q}),\delta v_1(\mathbf{q}),\delta v_2(\mathbf{q}),\delta v_3(\mathbf{q}))^T,\end{aligned} \tag{73}$$

and $\mathbf{M}(\mathbf{q})$ the 8×8 matrix

$$\mathbf{M}(\mathbf{q}) = 2S\begin{pmatrix}\mathbf{M}^{11}(\mathbf{q}) & \mathbf{M}^{12}(\mathbf{q})\\ \mathbf{M}^{21}(\mathbf{q}) & \mathbf{M}^{22}(\mathbf{q})\end{pmatrix} \tag{74}$$

built from 4×4 blocks

$$\begin{aligned}\mathbf{M}^{11}_{ij}(\mathbf{q}) &= \cos(\mathbf{q}\cdot\mathbf{r}_{ij})\\ &\quad\times\left(\mathbf{u}_i\cdot\mathbf{J}_{ij}\cdot\mathbf{u}_j - \delta_{ij}\sum_l(\mathbf{w}_l\cdot\mathbf{J}_{lj}\cdot\mathbf{w}_j)\right),\end{aligned} \tag{75}$$

$$\mathbf{M}^{12}_{ij}(\mathbf{q}) = \mathbf{M}^{21}_{ji}(\mathbf{q}) = \cos(\mathbf{q}\cdot\mathbf{r}_{ij})(\mathbf{v}_i\cdot\mathbf{J}_{ij}\cdot\mathbf{u}_j), \tag{76}$$

$$\begin{aligned}\mathbf{M}^{22}_{ij}(\mathbf{q}) &= \cos(\mathbf{q}\cdot\mathbf{r}_{ij})\\ &\quad\times\left(\mathbf{v}_i\cdot\mathbf{J}_{ij}\cdot\mathbf{v}_j - \delta_{ij}\sum_l(\mathbf{w}_l\cdot\mathbf{J}_{lj}\cdot\mathbf{w}_j)\right),\end{aligned} \tag{77}$$

where $i,j \in \{0,1,2,3\}$ and $\mathbf{r}_{ij} = \mathbf{r}_j - \mathbf{r}_i$ [cf. Eq. (A1)].

The matrix $\mathbf{M}(\mathbf{q})$ [Eq. (74)] can be diagonalized by a suitable orthogonal transformation $\mathbf{U} = (\mathbf{U}^T)^{-1}$ to give

$$\mathcal{H}^{\mathsf{CSW}}_{\mathsf{ex}} = \frac{1}{2}\sum_{\mathbf{q}}\sum_{\nu=1}^{8}\kappa_{\nu\mathbf{q}}\upsilon_{\nu\mathbf{q}}\upsilon_{\nu-\mathbf{q}}, \tag{78}$$

where the eight normal modes of the system are given by

$$\upsilon(\mathbf{q}) = \mathbf{U}\cdot\tilde{u}(\mathbf{q}), \tag{79}$$

with associated eigenvalues $\kappa_\nu(\mathbf{q})$. Since $\mathcal{H}^{\mathsf{CSW}}_{\mathsf{ex}}$ [Eq. (78)] is quadratic in $\upsilon_{\nu\mathbf{q}}$, the associated partition function can be calculated exactly

$$\begin{aligned}\mathcal{Z}^{\mathsf{CSW}}_{\mathsf{ex}} &= \left(\frac{1}{\sqrt{2\pi}}\right)^{2N}\exp\left(\frac{-\mathcal{E}_0}{T}\right)\int\left[\prod_{\nu=1}^{8}\prod_{\mathbf{q}}d\upsilon_{\nu\mathbf{q}}\right]\\ &\quad\times\exp\left(-\frac{1}{2}\frac{\sum_{\nu=1}^{8}\sum_{\mathbf{q}}\kappa_{\nu\mathbf{q}}\upsilon_{\nu\mathbf{q}}\upsilon_{\nu-\mathbf{q}}}{T}\right)\\ &= \exp\left(\frac{-\mathcal{E}_0}{T}\right)\prod_{\nu=1}^{8}\prod_{\mathbf{q}}\left(\sqrt{\frac{T}{\kappa_{\nu\mathbf{q}}}}\right).\end{aligned} \tag{80}$$

It follows that, for $T \to 0$, the free energy of the system is given by

$$\mathcal{F}^{\mathsf{low-T}}_{\mathsf{ex}} = \mathcal{E}_0 + \frac{T}{2}\sum_{\nu\mathbf{q}}\ln\kappa_{\nu\mathbf{q}} - NT\ln T + O(T^2). \tag{81}$$

Where the $O(T^2)$ corrections arise from the higher order, spin-wave interaction, terms neglected in Eq. (69).

Within this classical, low-T expansion, the eigenvalues $\kappa_\nu(\mathbf{q})$ correspond to independent, low-energy modes, which determine the physical properties of the states, and have the interpretation of a classical spin-wave spectrum. However the classical spectrum $\kappa_\nu(\mathbf{q})$ should *not* be confused with the quantum spin-wave dispersion $\omega_\nu(\mathbf{q})$, measured in inelastic neutron scattering experiments and discussed in Sec. IV C.

B. Ground-state selection within the one-dimensional manifold of states with E symmetry

Energy alone does not select between the one-dimensional manifold of states with E symmetry [25,87]. However quantum fluctuations [26,27,46], thermal fluctuations at low temperature [25,87], thermal fluctuations near the ordering temperature [28,77], structural disorder [78,79], and structural distortion [78] *are* effective in selecting an ordered ground state. In what follows, we use knowledge of the free energy within a classical spin-wave theory $\mathcal{F}^{\mathsf{low-T}}_{\mathsf{ex}}$ [Eq. (81)] to determine which of the possible E-symmetry ground states is selected by thermal fluctuations in the limit $T \to 0$. A parallel treatment of the quantum problem is given in Ref. [46] and a classical analysis applied to the limiting case of pure XY spins (i.e., with infinite easy plane anisotropy) is given in Ref. [82].

As a first step, it is helpful to write down a minimal, symmetry allowed, form for the free energy in terms of the components of

$$\mathbf{m}_{\mathsf{E}} = \begin{pmatrix}m_{\mathsf{E}}\cos(\theta_{\mathsf{E}})\\ m_{\mathsf{E}}\sin(\theta_{\mathsf{E}})\end{pmatrix} \tag{82}$$

(cf. [81]). Keeping only those terms which respect the lattice symmetries, and going up to sixth order in m_{E},

$$\begin{aligned}\mathcal{F}_{\mathsf{E}} = \mathcal{F}_0 &+ \tfrac{1}{2}\,a\,m_{\mathsf{E}}^2 + \tfrac{1}{4}\,b\,m_{\mathsf{E}}^4 + \tfrac{1}{6}\,c\,m_{\mathsf{E}}^6\\ &+ \tfrac{1}{6}\,d\,m_{\mathsf{E}}^6\,\cos(6\,\theta_{\mathsf{E}}) + O\big(m_{\mathsf{E}}^8\big),\end{aligned} \tag{83}$$

where $\mathcal{F}_0$ is an unimportant constant.

Note that Eq. (83) does not contain the symmetry allowed coupling to m_{A_2}:

$$m_{\mathsf{A}_2}m_{\mathsf{E}}^3\cos(3\theta_{\mathsf{E}}),$$

which appears in [81]. This is for two reasons: (i) we are considering the $T \to 0^+$ limit where a finite value of m_{A_2} is energetically unfavorable and will be very small; and (ii) m_{A_2} can, in any case, be integrated out to arrive at Eq. (83) with renormalized coefficients for the sixth order terms.

It follows from Eq. (83) that (i) a suitable order parameter for symmetry breaking within this manifold is $c_{\mathsf{E}} = \cos 6\theta_{\mathsf{E}}$ [77,80], cf. Eq. (40), and that (ii) the two states spanning $\mathbf{m}_{\mathsf{E}}$, Ψ_2, and Ψ_3 are distinguished only at sixth order (and higher) in m_{E} [43]. The quantity c_E is a secondary order parameter, in the sense that a finite expectation value of c_{E} is induced by coupling to the primary order parameter $\mathbf{m}_{\mathsf{E}}$. These facts have important consequences for the finite temperature phase transition into the paramagnet, as discussed below.

For $T \to 0$, we can parametrize $\mathcal{F}_{\mathsf{E}}$ [Eq. (83)] from $\mathcal{F}^{\mathsf{low-T}}_{\mathsf{ex}}$ [Eq. (81)]. Since $\mathcal{H}^{[\mathsf{T_d}]}_{\mathsf{ex}}$ [Eq. (21)] is quadratic in $\mathbf{m}_{\mathsf{E}}$, all other terms in the free energy must be of purely entropic origin. Moreover, symmetry requires that the entropy associated with the E-symmetry states will vary as

$$\mathcal{S}_{\mathsf{E}}(\theta_{\mathsf{E}}) = N\sum_{n=0,1,2,\ldots}s_n\cos(6n\theta_{\mathsf{E}}). \tag{84}$$

The sign of the coefficients s_n then determines the ground state selected by fluctuations. Taking the derivative of Eq. (81) with

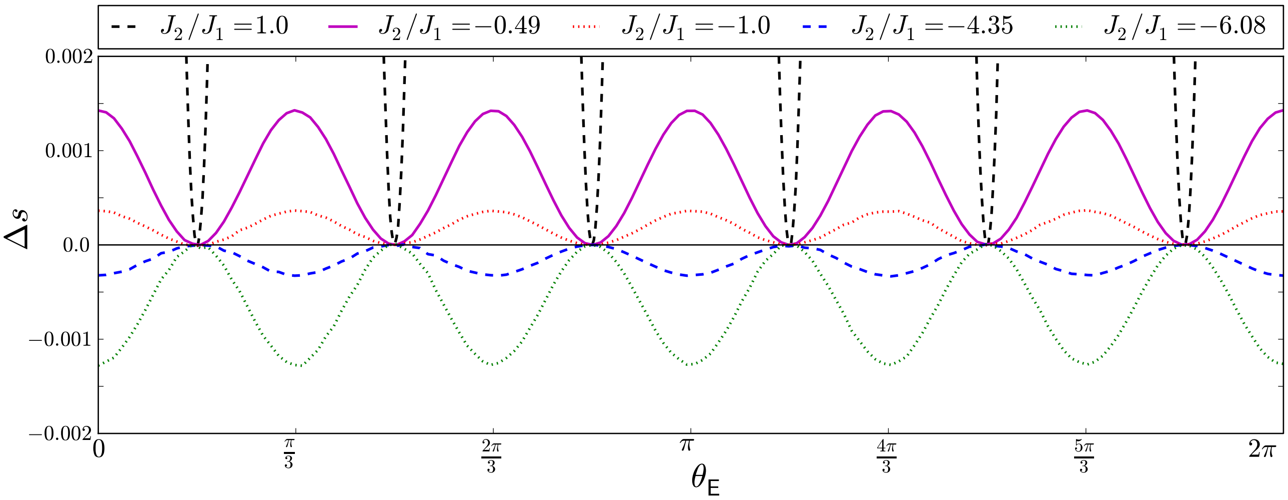

FIG. 14. Variation of entropy per spin within the one-dimensional manifold of states with symmetry E. Entropy $\mathcal{S}(\theta_{\mathsf{E}})$ has been estimated using the low-temperature expansion [Eq. (85)], for a range of values of J_2, with the entropy of the Ψ_3 state subtracted as a reference, i.e., $\Delta s_{\theta_{\mathsf{E}}} = [\mathcal{S}(\theta_{\mathsf{E}}) - \mathcal{S}(\pi/6)]/N$. The parameters $J_1 = 0.115$ meV and $J_3 = -0.099$ meV were fixed at values appropriate to $Er_2Ti_2O_7$ [26], setting $J_4 \equiv 0$. In all cases, $\Delta s_{\theta_{\mathsf{E}}}$ repeats with period $\pi/3$. For a choice of J_2 appropriate to $Er_2Ti_2O_7$ ($J_2/J_1 = -0.49$—solid purple line), entropy takes on its maximum value for $\theta_{\mathsf{E}} = \frac{n\pi}{3}$, with $n = 0,1,2,3,4,5$, corresponding to the six Ψ_2 ground states. The extreme variation in entropy at the boundary of the Palmer-Chalker phase ($J_1 = J_2$—dashed black line), reflects the presence of an $O(L^2)$ set of zero modes in the spectrum of Ψ_2 ground state. Nonetheless, the entropy difference between Ψ_2 and Ψ_3, $\Delta s_{\pi/3} \approx 0.18$, remains finite. For sufficiently negative J_2 (dashed blue line, dotted green line) $\Delta s_{\pi/3} < 0$, and fluctuations select the Ψ_3 state. All results have been calculated from Eq. (85), with the sum evaluated numerically by a Monte Carlo method. Statistical errors are smaller than the point size.

respect to T allows us to explicitly calculate $\mathcal{S}_{\mathsf{E}}(\theta_{\mathsf{E}})$:

$$\frac{\mathcal{S}_{\mathsf{E}}(\theta_{\mathsf{E}})}{N} = -\frac{1}{N}\frac{\partial \mathcal{F}_{\mathsf{ex}}^{\mathsf{low-T}}}{\partial T}$$
$$= \ln T + 1 - \frac{1}{2N}\sum_{\mathbf{q}} \ln\{\det[\mathbf{M}_{\theta_{\mathsf{E}}}(\mathbf{q})]\} \qquad (85)$$

(cf. Ref. [86]), where $\mathbf{M}_{\theta_{\mathsf{E}}}(\mathbf{q})$ is the 8×8 matrix defined in Eq. (74), calculated by expanding around a state with a particular value of θ_{E}. These results are illustrated in Fig. 14. Equivalent calculations, carried out numerically for all parameters associated with E-symmetry ground states, lead to the phase boundary between Ψ_2 and Ψ_3 shown in Fig. 1. For parameters appropriate to $Er_2Ti_2O_7$ [26], we find that fluctuations select a Ψ_2 ground state, in keeping with published work [26,27,43,87].

We can now learn more about how ground-state selection works by realizing that, for some choices of parameters, the operation connecting different E-symmetry ground states becomes an *exact* symmetry of the Hamiltonian. This is most easily seen in a coordinate frame tied to the local [111] axis, as described in Sec. II C. Considering $\mathcal{H}_{\mathsf{ex}}^{\mathsf{local}}$ [Eq. (8)], for the simple choice of parameters

$$(J_{zz},\ J_{\pm},\ J_{\pm\pm},\ J_{z\pm}) = (0,\ J,\ 0,\ 0), \quad J > 0$$

the ground state belongs to E and the Hamiltonian reduces to that of an XY ferromagnet. In this case the entire one-dimensional manifold of E-symmetry states are connected by an explicit symmetry of the Hamiltonian (rotation around the local $\langle 111\rangle$ axes). It follows that order-by-disorder is ineffective, and the ground state retains its $U(1)$ symmetry—for a related discussion, see [46].

To gain insight into the phase diagram for $J_3 < 0,\ J_4 \equiv 0$ (cf. Fig. 1), we expand about a point in parameter space

$$(J_{zz},\ J_{\pm},\ J_{\pm\pm},\ J_{z\pm}) = (-2J,\ J,\ 0,\ 0) \quad J > 0$$
$$\Rightarrow (J_1, J_2, J_3, J_4) = (2J, -2J, 0, 0).$$

At this point the ground-state manifold is formed from linear combinations of E and A_2 symmetry states and the entire ground-state manifold is connected by an exact symmetry of the Hamiltonian, so once again there is no order-by-disorder. For $J_3 < 0$, states with a finite value of m_{A_2} are removed from the ground-state manifold and fluctuations select a ground state from among the E states. It follows that, for $J_3 \to 0^-$, $J_4 \equiv 0$, the phase boundary between the Ψ_2 and Ψ_3 states should tend to the line $J_2/|J_3| = -J_1/|J_3|$ (cf. Fig. 1).

To see which phase is preferred for finite J_3, we expand the difference in entropy $\mathcal{S}_{\mathsf{E}}(\theta_{\mathsf{E}})$ between the Ψ_2 and Ψ_3 ground states

$$\Delta s_{\pi/3} = \frac{\mathcal{S}_{\mathsf{E}}(\pi/3) - \mathcal{S}_{\mathsf{E}}(\pi/6)}{N} \qquad (86)$$

in powers of $J_{\pm\pm}$ and $J_{z\pm}$. We do this by writing the matrix $\mathbf{M}(\mathbf{q})$ [Eq. (74)] as

$$\mathbf{M}(\mathbf{q}) = \mathbf{M}_0(\mathbf{q}) + \epsilon\mathbf{X}(\mathbf{q}), \qquad (87)$$

where $\mathbf{M}_0(\mathbf{q})$ is the matrix associated with the high-symmetry point, and $\mathbf{X}(\mathbf{q})$ is that associated with the perturbation, and noting that

$$\ln[\det(\mathbf{M}_0 + \epsilon\mathbf{X})]$$
$$= \ln[\det(\mathbf{M}_0)] + \sum_{n=1}^{\infty}(-1)^{(n+1)}\frac{\epsilon^n}{n}\,\mathrm{Tr}\left[\left(\mathbf{X}\cdot\mathbf{M}_0^{-1}\right)^n\right]. \qquad (88)$$

We then expand in powers of $J_{\pm\pm}$ and $J_{z\pm}$.

We find that the leading correction to $\Delta s_{\pi/3}$ is

$$\Delta s_{\pi/3} \approx a\left(\frac{J_{\pm\pm}}{J_{\pm}}\right)^3, \tag{89}$$

where $a = 0.0045$. It follows that, for sufficiently small J_3, the phase boundary between Ψ_2 and Ψ_3 should tend to the line $J_{\pm\pm} = 0$, with the Ψ_2 phase favored for $J_{\pm\pm} > 0$ and Ψ_3 favored for $J_{\pm\pm} < 0$. Numerical evaluation of Eq. (85), in the limit $J_3 \to 0$, yields results in agreement with these arguments (cf. Fig. 1).

On the line $J_{\pm\pm} = 0$ itself, we find that the leading correction to the difference in entropy is

$$\Delta s_{\pi/3} \approx b\left(\frac{J_{z\pm}}{J_{\pm}}\right)^6, \tag{90}$$

with $b = -5.3 \times 10^{-5}$. Hence the Ψ_3 state is weakly preferred, and the phase boundary will bend towards positive $J_2/|J_3|$, as observed in Fig. 1. Since $J_{z\pm}$ is a term which drives ferromagnetic out-of-plane fluctuations, a negative sign for b is consistent with the argument that Ψ_3 is better connected to the ferromagnetic phase, and hence has a softer spectrum for ferromagnetic out-of-plane fluctuations. On the other hand, symmetries of the Ψ_2 states have been shown to allow for small antiferromagnetic out-of-plane ordering, of the all-in, all-out type [81].

In the limit $|J_3| \gtrsim (|J_1|,|J_2|)$, numerical evaluation of Eq. (85) yields the more complex, reentrant behavior, as seen in Fig. 1. This behavior occurs over a very narrow region of parameter space, and is discussed in detail in Ref. [46] for the case of quantum, as opposed to thermal, order-by-disorder.

C. Quantum spin-wave theory

Quantum spin-wave theories for $\mathbf{q} = 0$, 4-sublattice classical ground states of $\mathcal{H}_{\text{ex}}$ [Eq. (1)] have been discussed by a number of authors, with attention focused on comparison with inelastic neutron scattering in applied magnetic field [26,44], and the way in which quantum fluctuations select between the one-dimensional manifold of states with E symmetry [26,27,46]. To date, all calculations have been carried out in the linear spin-wave approximation

$$\mathcal{H}_{\text{ex}} \approx \mathcal{E}_0\left(1+\frac{1}{S}\right) + \sum_{\mathbf{q}}\sum_{\nu=0}^{3}\omega_\nu(\mathbf{q}) \times \left(b^\dagger_\nu(\mathbf{q})b_\nu(\mathbf{q}) + \frac{1}{2}\right) + \cdots, \tag{91}$$

where $\mathcal{E}_0$ is the classical ground-state energy defined in Eq. (70), $\omega_\nu(\mathbf{q})$ is the spin-wave dispersion, and b_ν is a set of noninteracting bosons describing spin-wave modes with band index $\nu = 0,1,2,3$.

Since the anisotropic exchange model $\mathcal{H}_{\text{ex}}$ [Eq. (1)] does not, in general, posses any continuous symmetry, spin-wave excitations about a 4-sublattice classical ground states will generally be gapped, and quantum effects are small. However, the enlarged ground-state manifolds occurring where different symmetry ground states meet can lead to "accidental" degeneracies in the spin-wave spectrum, and large quantum fluctuations about the ordered state. The effect of these fluctuations on classical order may be estimated by calculating the correction to the ordered moment on sublattice i, $\langle S_i^w\rangle$ defined in Eq. (B1). Details of calculations are given in Appendix B. In all of the 4-sublattice phases described in this text, $\langle S_i^w\rangle$ is the same for all sublattices $i = 0,1,2,3$.

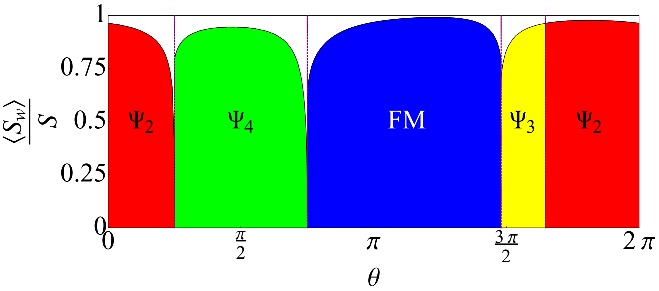

FIG. 15. Fraction of the classical moment achieved in ordered phases of a pyrochlore magnet with anisotropic exchange interactions, within linear spin-wave theory. Away from the phase boundaries, the ordered moment is close to its full classical value. All results are obtained within a linear spin-wave analysis of $\mathcal{H}_{\text{ex}}$ [Eq. (1)]—cf. Appendix B—with $J_1/|J_3| = 3\cos\theta$, $J_2/|J_3| = 3\cos\theta$, $J_3 < 0$, $J_4 \equiv 0$, corresponding to the white circle in Figs. 1 and 2.

In Fig. 15 we show the effect of quantum fluctuations on the classical, zero-temperature ground states of $\mathcal{H}_{\text{ex}}$ [Eq. (1)]. For parameters which are deep within the ordered phases, the ordered moment approaches its full classical value. However, the enlarged ground-state degeneracies on classical phase boundaries lead to additional zero modes in the spin-wave spectrum, and correspondingly larger corrections. Corrections to the ordered moment diverge logarithmically approaching the boundary with the Palmer-Chalker phase from Ψ_2, where there are entire planes of zero modes, and approaching the boundary with the ferromagnetic phases from the Palmer-Chalker phase.

In Fig. 2 (Sec. I) we show the quantum phase diagram of $\mathcal{H}_{\text{ex}}$ [Eq. (1)], within linear spin-wave theory. Regions where quantum fluctuations eliminate the ordered moment entirely, are shaded white. The effect is strongest where the degeneracy of the classical ground state is highest, i.e., approaching the Heisenberg line

$$J_1/|J_3| = J_2/|J_3| \to \infty,$$

and in the vicinity of the special point [48]

$$J_1/|J_3|\ ,\ J_2/|J_3| \to 0.$$

The absence of an ordered moment within linear spin-wave theory can indicate a region where conventional magnetic order breaks down entirely, and typically underestimates the extent of any unconventional order [88–91]. It therefore seems reasonable to suggest that the vicinity of these phase boundaries will be favorable places to find novel quantum ground states and quantum spin liquids. We will return to this point in our discussion of $Er_2Sn_2O_7$, in Sec. IX.

D. Cross section in neutron scattering

Inelastic neutron scattering experiments measure the dynamical structure factor

$$S(\mathbf{q},\omega) = \sum_{\alpha,\beta=1}^{3}\sum_{i,j=0}^{3}\left(\delta_{\alpha\beta} - \frac{q_\alpha q_\beta}{q^2}\right) \times \left\langle m_\alpha^i(-\mathbf{q},-\omega) m_\beta^j(\mathbf{q},\omega)\right\rangle, \tag{92}$$

where the projection operator

$$\left(\delta_{\alpha\beta} - \frac{q_\alpha q_\beta}{q^2}\right)$$

reflects the fact the neutron interacts with the components of the spin transverse to the momentum transfer $\mathbf{q}$, and

$$m_\alpha^i(\mathbf{q}) = \frac{1}{\sqrt{2\pi}}\sqrt{\frac{4}{N}}\sum_{\beta=1}^{3} g_i^{\alpha\beta} \times \int dt \left(\sum_{\mathbf{R}_i} e^{-i\omega t} e^{i\mathbf{q}\cdot\mathbf{R}_i} S_i^\beta(\mathbf{R}_i,t)\right) \tag{93}$$

is the Fourier transform of the magnetic moment associated with the rare-earth ions, for a given sublattice $i = 0,1,2,3$. The associated g-tensor $g_i^{\alpha\beta}$ is defined in Appendix A.

The equal-time structure factor measured in energy-integrated, quasielastic neutron scattering, is given by

$$S(\mathbf{q},t=0) = \frac{1}{\sqrt{2\pi}}\int_{-\infty}^{\infty} d\omega\, S(\mathbf{q},\omega) = \sum_{\alpha,\beta=1}^{3}\sum_{i,j=0}^{3}\left(\delta_{\alpha\beta} - \frac{q_\alpha q_\beta}{q^2}\right) \times \left\langle m_\alpha^i(-\mathbf{q},t=0) m_\beta^j(\mathbf{q},t=0)\right\rangle. \tag{94}$$

For many purposes it is also convenient to resolve the equal-time structure factor $S(\mathbf{q}) = S(\mathbf{q},t=0)$ into spin-flip (SF) and nonspin flip (NSF) components, or comparison with experiments carried out using polarized neutrons. For neutrons with polarization along a direction $\hat{\mathbf{n}} \perp \mathbf{q}$, these are given by

$$S^{\mathsf{NSF}}(\mathbf{q}) = \sum_{i,j=0}^{3}\langle[\mathbf{m}^i(-\mathbf{q})\cdot\hat{\mathbf{n}}](\mathbf{m}^j(\mathbf{q})\cdot\hat{\mathbf{n}}]\rangle, \tag{95}$$

$$S^{\mathsf{SF}}(\mathbf{q}) = \sum_{i,j=0}^{3}\frac{1}{q^2}\langle[\mathbf{m}^i(-\mathbf{q})\cdot(\hat{\mathbf{n}}\times\mathbf{q})] \times [\mathbf{m}^j(\mathbf{q})\cdot(\hat{\mathbf{n}}\times\mathbf{q})]\rangle. \tag{96}$$

In this article, where we quote results for SF and NSF components of $S(\mathbf{q})$, we follow the conventions of Fennell *et al.* [92] and consider $\hat{\mathbf{n}} = (1,-1,0)/\sqrt{2}$.

Connection to theory is made by using simulation or spin-wave theory to evaluate the correlations of the magnetic moments $m_\alpha^i(\mathbf{q},t)$. Equal-time correlations $S(\mathbf{q})$ [Eqs. (94)–(96)] can be calculated directly using classical Monte Carlo simulation described in Sec. V, or using the classical spin-wave theory described in Sec. IV A. The quantum spin-wave theory described in Sec. IV C and Appendix B gives access to the full dynamical structure factor $S(\mathbf{q},\omega)$ [Eq. (92)], as measured by inelastic neutron scattering.

In the case of the classical spin-wave theory discussed in Sec. IV A, equal time correlations $\langle m_\alpha^i(-\mathbf{q})m_\beta^j(\mathbf{q})\rangle$ are expressed in terms of the correlations of the spin-wave modes $\upsilon_\nu(\mathbf{q})$ using Eqs. (68) and (79). The required correlation functions $\langle\upsilon_{\nu\mathbf{q}}\upsilon_{\lambda-\mathbf{q}}\rangle$ can then be obtained directly from Eq. (80):

$$\langle\upsilon_{\nu\mathbf{q}}\upsilon_{\lambda-\mathbf{q}}\rangle = \delta_{\nu\lambda}\frac{T}{\kappa_{\nu\mathbf{q}}}. \tag{97}$$

In Figs. 20, 21, and 22, explicit comparison is made between the equal-time structure factor $S(\mathbf{q})$ calculated within classical Monte Carlo simulation, and from a low-temperature classical spin-wave theory. We find excellent, quantitative agreement between the two approaches. This confirms classical spin-wave theory as a useful link between the exact analytical zero-temperature theory developed in Secs. II and III and the finite-temperature simulations presented in Sec. V.

In the case of the quantum spin-wave theory described in Sec. IV C and Appendix B, it is necessary to reexpress the spin correlation functions $\langle S_i^\alpha S_j^\beta\rangle$ in terms of the spin-wave operators $b_\nu^\dagger, b_\nu$ [cf. Eq. (91)]. This can be accomplished using the Bogoliubov transformations described in Appendix B. Within linear spin-wave theory, the correlations of b_ν take on a simple form

$$\langle b_\nu^\dagger(\mathbf{q},\omega)b_{\nu'}^\dagger(-\mathbf{q},-\omega)\rangle = \langle b_\nu(\mathbf{q},\omega)b_{\nu'}(-\mathbf{q},-\omega)\rangle = 0, \tag{98}$$

$$\langle b_\nu(\mathbf{q},\omega)b_{\nu'}^\dagger(\mathbf{q},\omega)\rangle = \delta_{\nu\nu'}\delta[\omega-\omega_\nu(\mathbf{q})] + \langle b_\nu^\dagger(\mathbf{q},\omega)b_{\nu'}(\mathbf{q},\omega)\rangle = \delta_{\nu\nu'}\delta[\omega-\omega_\nu(\mathbf{q})]\{1+n_B[\omega_\nu(\mathbf{q})]\}, \tag{99}$$

where $\delta[\omega-\omega_\nu(\mathbf{q})]$ is the Dirac delta function enforcing conservation of energy and $n_B(\omega)$ is the Bose-Einstein distribution

$$n_B(\omega) = \frac{1}{\exp\left(\frac{\omega}{T}\right)-1}. \tag{100}$$

V. FINITE-TEMPERATURE PROPERTIES

The symmetry analysis and Lego-brick rules described in Sec. II, analysis of ground-state energy described in Sec. III, and spin-wave theory described in Sec. IV, together make it possible to determine the ordered ground states of the anisotropic exchange model $\mathcal{H}_{\mathsf{ex}}$ [Eq. (1)], in the limit $T \to 0$. The resulting classical ground-state phase diagram is shown in phase diagram Fig. 1. However the interesting and unusual properties of rare-earth pyrochlore oxides all come from experiments carried out at finite temperature, and often relate to paramagnetic, rather than ordered phases. We have therefore used classical Monte Carlo simulations to explore the physics of $\mathcal{H}_{\mathsf{ex}}$ at finite temperature. The main conclusions of these simulations are summarized in the finite-temperature phase diagram Fig. 3.

We note that, although the systems we wish to describe are fundamentally quantum in nature, the classical simulations can be expected to give a qualitatively correct description of the physics in the high temperature, paramagnetic phase, where thermal fluctuations destroy quantum coherence. The classical description should also work, at least in some respects, at low temperature as long as the ground state of the quantum system is in a classically ordered phase. Ultimately, the best justification for our approach will come *a posteriori* from agreement with neutron scattering experiments (cf. Fig. 24).

In what follows we document the nature of phase transitions from the paramagnet into each of the ordered phases (Secs. V A–V D), and explore how the enlarged ground-state degeneracies at classical phase boundaries manifest themselves at finite temperature (Sec. VI). Technical details of simulations are given in Appendix C.

A. Finite-temperature transition from the paramagnet into the Palmer-Chalker phase

The most revealing feature of any broken-symmetry state is usually its finite-temperature phase transition. In Fig. 16 we show simulation results for the finite-temperature phase transition from the paramagnet into the Palmer-Chalker phase with T_2 symmetry. Simulations were carried out for parameters

$$(J_1,\ J_2,\ J_3,\ J_4) = (0,0.3,-0.1,0) \quad \text{meV}$$

deep within the Palmer-Chalker phase. Clear evidence for a phase transition can be found in the anomalies in both the specific heat $c_h(T)$ [Fig. 16(a)], and the order-parameter susceptibility $\chi_{\mathsf{T}_2}(T)$ [Fig. 16(b)] at $T_{\mathsf{T}_2} = 305 \pm 5$ mK.

Symmetry permits a continuous phase transition between the paramagnet and the Palmer-Chalker phase. However for this parameter set, fluctuations drive the transition first order, as is evident from the discontinuity in the value of the order parameter $\mathbf{m}_{\mathsf{T}_2}$ for $T = T_{\mathsf{T}_2}$ [Fig. 16(c)], and the double peak in the probability distribution for the energy [Fig. 16(d)].

B. Transition from the paramagnet into the noncolinear ferromagnetic phase

In Fig. 17 we show simulation results for the finite-temperature phase transition from the paramagnet into the noncollinear ferromagnet, for parameters appropriate to $\mathrm{Yb_2Ti_2O_7}$ [44], setting $J_4 = 0$,

$$(J_1,\ J_2,\ J_3,\ J_4) = (-0.09,-0.22,-0.29,0) \quad \text{meV}.$$

Anomalies in both the specific heat $c_h(T)$ [Fig. 17(a)] and order-parameter susceptibility $\chi_{\mathsf{T}_1}(T)$ [Fig. 17(b)] at $T_{\mathsf{T}_1} = 455 \pm 5$ mK, provide clear evidence of a phase transition.

At low temperatures, the temperature dependence of the order parameters $\mathbf{m}_{\mathsf{T}_{1,\mathsf{A}}}$ and $\mathbf{m}_{\mathsf{T}_{1,\mathsf{B}}}$ [Figs. 17(c) and 17(d)] converges on the values expected from the zero-temperature analysis of Sec. III B, and with a slope predicted by a low-temperature expansion about the FM ground state (not shown).

The single peak in the probability distribution for the energy [Fig. 17(e)] suggests that for these parameters, the thermal phase transition from paramagnet to noncollinear FM in a classical model is probably continuous and at most very weakly first order.

C. Transition from the paramagnet into the Ψ_2 phase

In Fig. 18 we show simulation results for the finite-temperature phase transition from the paramagnet into the Ψ_2 phase, for parameters appropriate to $\mathrm{Er_2Ti_2O_7}$ [26], setting $J_4 = 0$,

$$(J_1,\ J_2,\ J_3,\ J_4) = (0.11,-0.06,-0.1,0) \quad \text{meV}.$$

This shows a number of interesting features.

Anomalies in both the specific heat $c_h(T)$ [Fig. 18(a)] and order-parameter susceptibility $\chi_{\mathsf{E}}(T)$ [Fig. 18(b)] at $T_{\mathsf{E}} = 505 \pm 5$ mK offer clear evidence of a phase transition.

Both the smooth evolution of the primary order parameter $\mathbf{m}_{\mathsf{E}}$ [Fig. 18(c)] and the single peak in the probability distribution for the energy [Fig. 18(e)] suggests that the phase transition seen in simulation is at most weakly first order. For

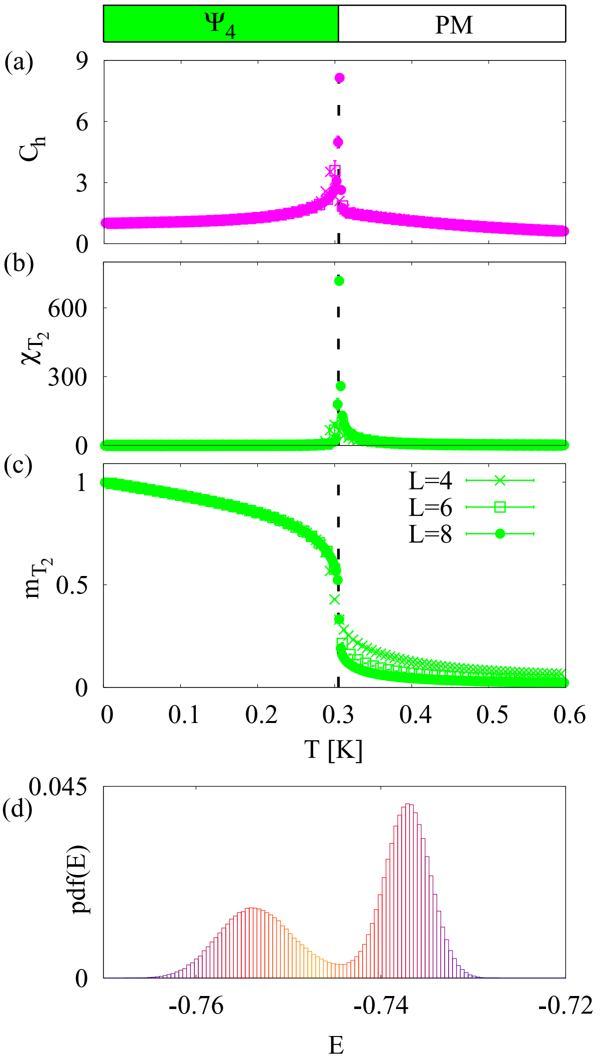

FIG. 16. Finite-temperature phase transition from the paramagnet into the Palmer-Chalker phase (Ψ_4), as determined by classical Monte Carlo simulation of $\mathcal{H}_{\mathsf{ex}}$ [Eq. (1)], for parameters $J_1 = 0$ meV, $J_2 = 0.3$ meV, $J_3 = -0.1$ meV, $J_4 = 0$ meV. (a) Temperature dependence of the specific heat $c_h(T)$. (b) Temperature dependence of the order-parameter susceptibility $\chi_{\mathsf{T}_2}(T)$. (c) Temperature dependence of the order parameter $|\mathbf{m}_{\mathsf{T}_2}(T)|$. (d) Probability distribution of the energy E evaluated at the transition temperature for a cluster of size $L = 12$. The black dashed lines in (a)–(c) indicates a first-order phase transition at $T_{\mathsf{T}_2} = 305 \pm 5$ mK. Simulations were performed for clusters of $N = 16L^3$ spins, with $L = 4,6,8,12$.

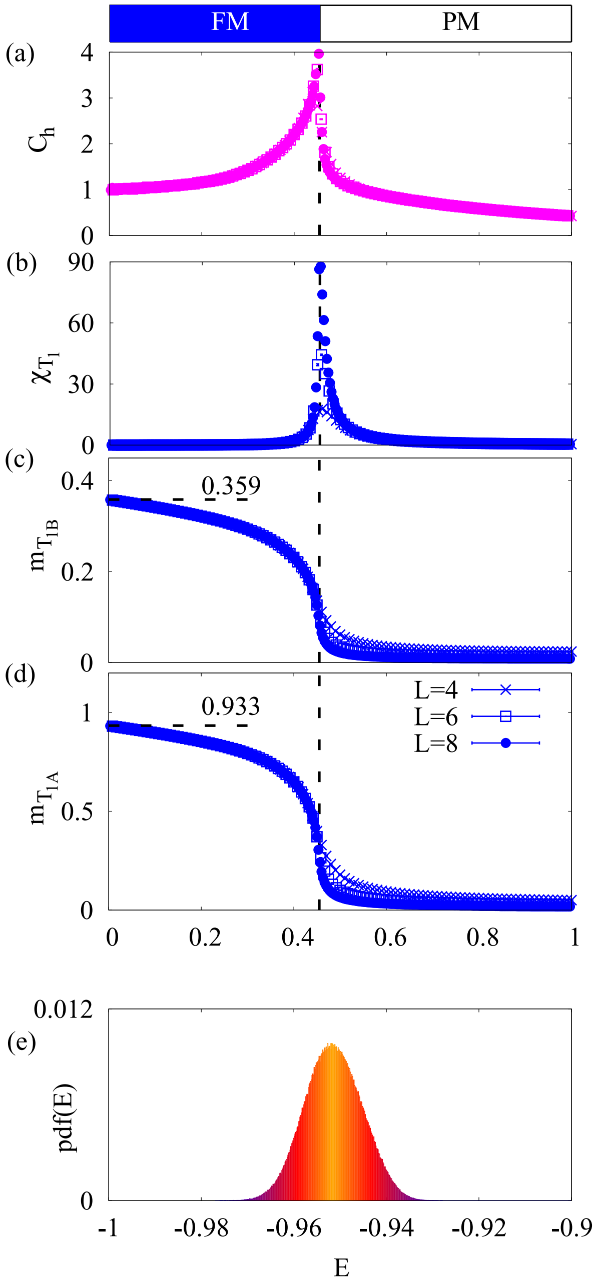

FIG. 17. Finite-temperature phase transition from the paramagnet into the noncollinear ferromagnet (FM), as determined by classical Monte Carlo simulation of $\mathcal{H}_{\rm ex}$ [Eq. (1)], for parameters appropriate to $Yb_2Ti_2O_7$ [44], i.e., $J_1 = -0.09$ meV, $J_2 = -0.22$ meV, $J_3 = -0.29$ meV setting $J_4 = 0$ meV. (a) Temperature dependence of the specific heat $c_h(T)$. (b) Temperature dependence of the order-parameter susceptibility $\chi_{\mathsf{T}_1}(T)$. (c) Temperature dependence of the order parameter $|\mathbf{m}_{\mathsf{T}_{1,\mathsf{B}}}(T)|$. (d) Temperature dependence of the order parameter $|\mathbf{m}_{\mathsf{T}_{1,\mathsf{A}}}(T)|$. (e) Probability distribution of the energy E evaluated at the transition for a system of size $L = 12$. The black dashed lines in (a)–(d) indicates a phase transition at $T_{\mathsf{T}_1} = 455 \pm 5$ mK. Simulations were performed for clusters of $N = 16L^3$ spins, with $L = 4,6,8,12$.

the clusters simulated, we confirm that it is possible to obtain a fairly good collapse of data for $\chi_{\mathsf{E}}(T)$ [Fig. 18(b)] using 3D XY exponents [77].

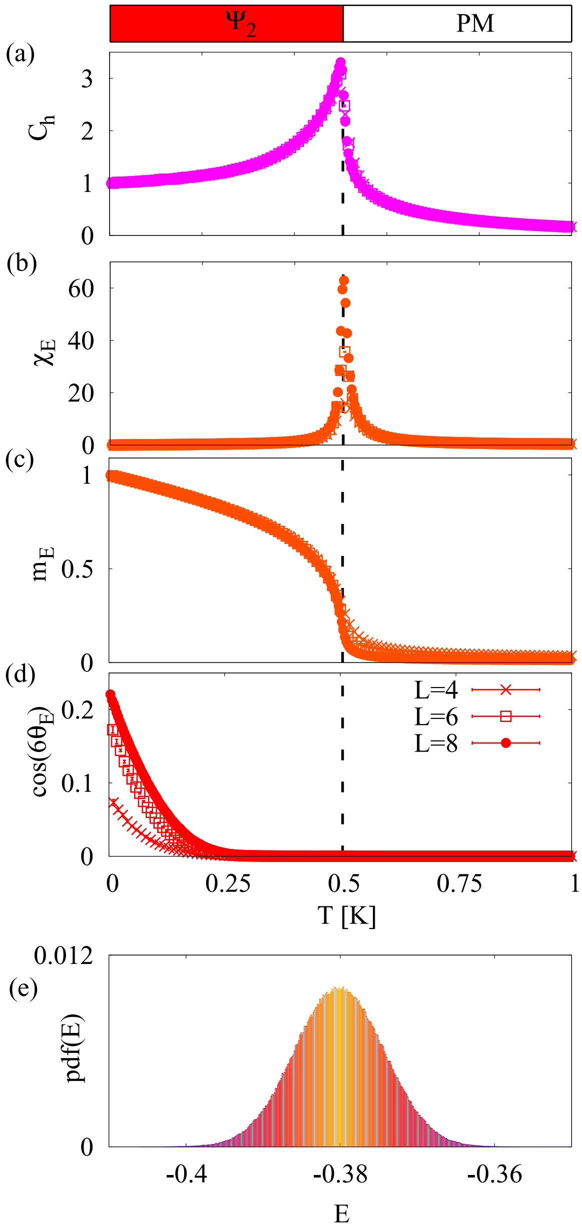

FIG. 18. Finite-temperature phase transition from the paramagnet into the noncoplanar antiferromagnet Ψ_2, as determined by classical Monte Carlo simulation of $\mathcal{H}_{\rm ex}$ [Eq. (1)], for parameters appropriate to $Er_2Ti_2O_7$ [26], i.e., $J_1 = 0.11$ meV, $J_2 = -0.06$ meV, $J_3 = -0.1$ meV setting $J_4 = 0$ meV. (a) Temperature dependence of the specific heat $c_h(T)$. (b) Temperature dependence of the order-parameter susceptibility $\chi_{\mathsf{E}}(T)$. (c) Temperature dependence of the order parameter $|\mathbf{m}_{\mathsf{E}}(T)|$. (d) Temperature dependence of the secondary order parameter $\cos 6\theta_{\mathsf{E}}$. (e) Probability distribution of the energy E evaluated at the transition temperature for a system of size $L = 12$. The black dashed line indicates a continuous phase transition at $T_N = 505 \pm 5$ mK. Simulations were performed for clusters of $N = 16L^3$ spins, with $L = 4,6,8,12$.

However, there are only a discrete number of Ψ_2 ground states, and a finite value of $|\mathbf{m}_{\mathsf{E}}|$ alone does not imply Ψ_2 order. Evidence for the Ψ_2 ground state comes from the secondary order parameter $c_{\mathsf{E}} = \cos 6\theta_{\mathsf{E}} > 0$ [Fig. 18(d)]. Here simulation results are strongly size dependent, but suggest a slow crossover into the Ψ_2 state, occurring at a $T^* \ll T_{\mathsf{E}}$, without any accompanying feature in $c_h(T)$ [Fig. 18(a)].

On the basis of Landau theory we anticipate that *any* finite value of $m_{\mathsf{E}} = |\mathbf{m}_{\mathsf{E}}|$ will induce degeneracy breaking in θ_{E}, and that the entropic selection within the E manifold should therefore occur concurrently with the onset of magnetic order. Depending on the sign of the relevant coupling,

$$\delta\mathcal{F}_{\mathsf{E}} = \tfrac{1}{6}\, d\, m_{\mathsf{E}}^6 \cos 6\theta_{\mathsf{E}}, \qquad (101)$$

the system will then enter either a Ψ_2 or a Ψ_3 ground state.

However, the free-energy barrier separating the Ψ_2 and Ψ_3 ground states is very small, and this in turn sets a very large length scale for the selection of the Ψ_2 ground state. Based on the low-temperature expansion $\mathcal{F}_{\text{ex}}^{\text{low}-\text{T}}$ [Eq. (81)], we estimate that clusters of $N \sim 10^9$ sites should be able to clearly resolve which state is selected at the magnetic ordering temperature.

D. Transition from the paramagnet into the Ψ_3 phase

In Fig. 19 we show simulation results for the finite-temperature phase transition from the paramagnet into the Ψ_3 phase, for parameters

$$(J_1,\ J_2,\ J_3,\ J_4) = (0, -0.3, -0.1, 0) \quad \text{meV}$$

close to the border with the noncollinear ferromagnet. Anomalies in both the specific heat $c_h(T)$ [Fig. 19(a)] and order-parameter susceptibility $\chi_{\mathsf{E}}(T)$ [Fig. 19(b)] at $T_{\mathsf{E}} = 395 \pm 5$ mK offer clear evidence of a phase transition. Both the smooth evolution of the primary order parameter $\mathbf{m}_{\mathsf{E}}$ [Fig. 19(c)], and the single peak in the probability distribution for the energy [Fig. 19(e)], suggest that this phase transition is continuous.

Evidence for the Ψ_3 ground state comes from the finite value of the secondary order parameter $c_{\mathsf{E}} = \cos 6\theta_{\mathsf{E}} < 0$ [Fig. 19(d)]. This secondary order parameter shows only a slow onset, consistent with a crossover into the Ψ_3 state, and is *very* strongly size dependent. As with the Ψ_2 state considered above, we infer that, with increasing system size, the temperature associated with this crossover scales towards $T = T_N$, and that in the thermodynamic limit, a single phase transition takes place from the paramagnet into the Ψ_3 state.

E. Comparison between Monte Carlo simulation and classical spin-wave theory

Here, to demonstrate the validity of our theory, we compare the structure factors, as calculated from the classical spin-wave theory $\mathcal{H}_{\text{ex}}^{\text{CSW}}$ [Eq. (78)] and Monte Carlo simulation, for three different parameter sets: the parameters of $Yb_2Ti_2O_7$ as found in Ref. [44] where the classical ground state is ferromagnetic, the parameters of $Er_2Ti_2O_7$ as found in Ref. [26] where we expect the order-by-disorder mechanism to favor the Ψ_2 states, and one set of parameters where the order-by-disorder mechanism favors the Ψ_3 states. We find excellent, quantitative agreement between the two methods.

In Fig. 20 we show the structure factor $S(\mathbf{q})$ calculated both from classical spin-wave theory and from Monte Carlo simulation at $T = 0.05$ K, in the NSF, SF, and total scattering channels [see Eqs. (94), (95), and (96)].

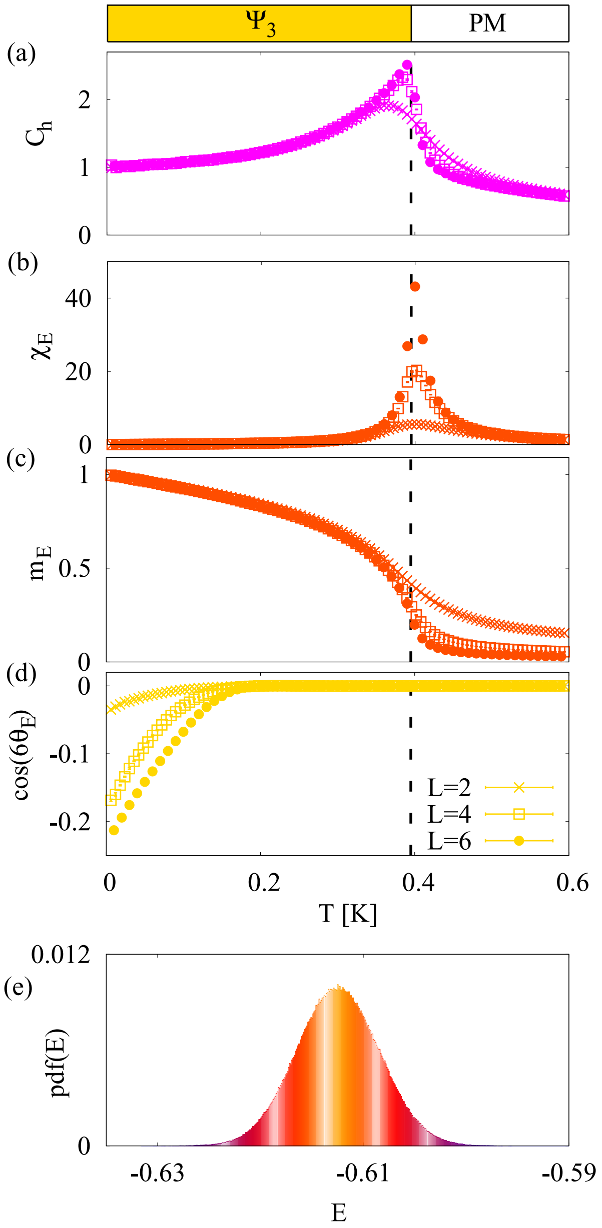

FIG. 19. Finite-temperature phase transition from the paramagnet into the coplanar antiferromagnet Ψ_3, as determined by classical Monte Carlo simulation of $\mathcal{H}_{\text{ex}}$ [Eq. (1)], for parameters $J_1 = 0$ meV, $J_2 = -0.3$ meV, $J_3 = -0.1$ meV, $J_4 = 0$ meV. (a) Temperature dependence of the specific heat $c_h(T)$. (b) Temperature dependence of the order-parameter susceptibility $\chi_{\mathsf{E}}(T)$. (c) Temperature dependence of the order parameter $|\mathbf{m}_{\mathsf{E}}(T)|$. (d) Temperature dependence of the secondary order parameter $\cos 6\theta_{\mathsf{E}}$. (e) Probability distribution of the energy E evaluated at the transition temperature for a system of size $L = 12$. The black dashed line indicates a continuous phase transition at $T_{\mathsf{E}} = 395 \pm 5$ mK. Simulations were performed for clusters of $N = 16L^3$ spins, with $L = 2,4,6,12$.

We have used the experimentally determined parameters for the g-tensor [93] $g_z = 1.77$, $g_{xy} = 4.18$ and exchange integrals [44] $J_1 = -0.09$ meV, $J_2 = -0.22$ meV, and $J_3 = -0.29$ meV, setting $J_4 \equiv 0$. The excellent, quantitative agreement between spin-wave theory and simulation demonstrates

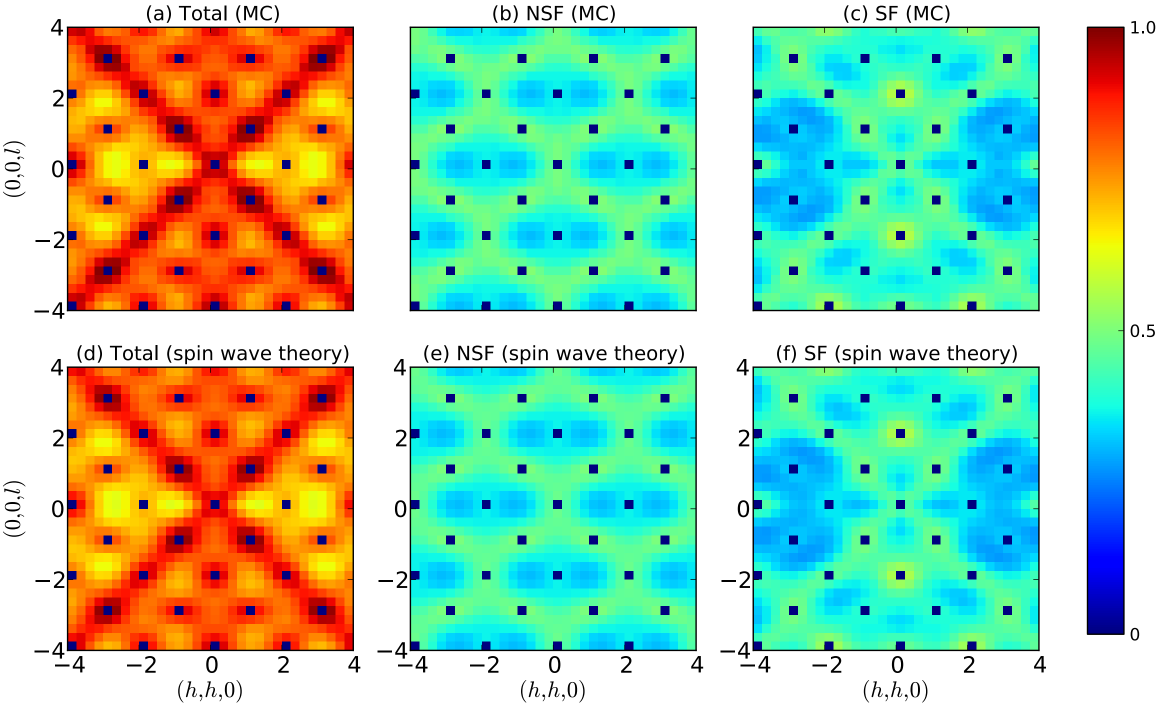

FIG. 20. Comparison between results for equal-time structure factor $S(\mathbf{q})$ obtained in classical Monte Carlo (MC) simulation and classical low-temperature expansion (spin-wave theory) for parameters appropriate to $Yb_2Ti_2O_7$ [44]. (a) Total scattering in the (h,h,l) plane within MC simulation. (b) Associated scattering in the non-spin-flip (NSF) channel. (c) Associated scattering in the spin-flip (SF) channel. (d) Total scattering in the (h,h,l) plane within a spin-wave expansion about the ferromagnetic ground state. (e) Associated scattering in the NSF channel. (f) Associated scattering in the SF channel. Rods of scattering in the (h,h,h) direction, associated with a low-energy spin-wave excitation (cf. Fig. 25), are visible in both SF and NSF channels. All results were obtained at $T = 0.05$ K, for exchange parameters $J_1 = -0.09$ meV, $J_2 = -0.22$ meV, $J_3 = -0.29$ meV, setting $J_4 = 0$. SF and NSF channels are defined with respect to a neutron with polarization in the $(1,-1,0)$ direction, as in Ref. [92]. $S(\mathbf{q})$ has been calculated using the experimentally measured g tensor for $Yb_2Ti_2O_7$ [44,93], with $g_z = 1.77, g_{xy} = 4.18$. In order to avoid saturating the color scale, the intensity associated with Bragg peaks at reciprocal lattice vectors has been subtracted.

the excellent equilibration of the simulations down to 0.05 K for the parameters of $Yb_2Ti_2O_7$.

$S(\mathbf{q})$ is also useful for studying the entropic ground-state selection within the one–dimensional manifold of state with E symmetry. For a given set of parameters we may compare the diffuse scattering calculated in spin-wave theory in expansions around the Ψ_3 and Ψ_2 phases with the diffuse scattering calculated in simulations.

Such a comparison is shown in Fig. 21, for exchange parameters appropriate to $Er_2Ti_2O_7$ ($J_1 = 0.11$ meV, $J_2 = -0.06$ meV, and $J_3 = -0.10$ meV, setting $J_4 \equiv 0$) and temperature $T = 0.36$ K. From the entropy calculations shown in Fig. 14 we expect the Ψ_2 state to be preferred for these values of the exchange parameters. Comparison of of the distribution of weight in the vicinity of the (1,1,1), (3,3,3), and (1,1,3) reciprocal lattice vectors between the Monte Carlo data and the spin-wave expansions around the Ψ_2 and Ψ_3 phases supports this conclusion.

Similarly, in Fig. 22 we show a comparison of the diffuse scattering between Monte Carlo simulations and spin-wave expansions around the Ψ_2 and Ψ_3 phases for exchange parameters approaching the noncollinear ferromagnetic phase ($J_1 = 0$, $J_2 = -1.0$ meV and $J_3 = -0.1$ meV, $J_4 = 0$), at $T = 0.4$ K. Calculations of the entropy within spin-wave theory show that the Ψ_3 state should be preferred by fluctuations for these parameters, and this is confirmed by the comparison of the structure factors, in particular by the presence of bright rods along the $\langle 111 \rangle$ directions.

VI. LIVING ON THE EDGE: THE INFLUENCE OF GROUND-STATE MANIFOLDS ON FINITE-TEMPERATURE PHASE TRANSITIONS

The major assertion of this article is that many of the interesting properties of pyrochlore magnets—for example the rods of scattering observed in $Yb_2Ti_2O_7$, and the order-by-disorder selection of a Ψ_2 ground state in $Er_2Ti_2O_7$, see Secs. VII and VIII—are the direct consequence of competition between different ordered phases, and in particular, of the high ground-state degeneracy where phases with different symmetry meet. While the arguments for enlarged ground-state manifolds at $T = 0$ are easy to understand, it is far less obvious that this degeneracy should make itself felt at finite temperature, especially where it is not protected by symmetry.

We can test the internal consistency of these ideas by using the probability distribution of the order parameter

$$\mathbf{m}_{\mathsf{E}} = m_{\mathsf{E}} (\cos\theta_{\mathsf{E}},\ \sin\theta_{\mathsf{E}})$$

[cf. Eq. (38)] to deconstruct the order-by-disorder selection of Ψ_2 and Ψ_3 ground states in finite-temperature simulations

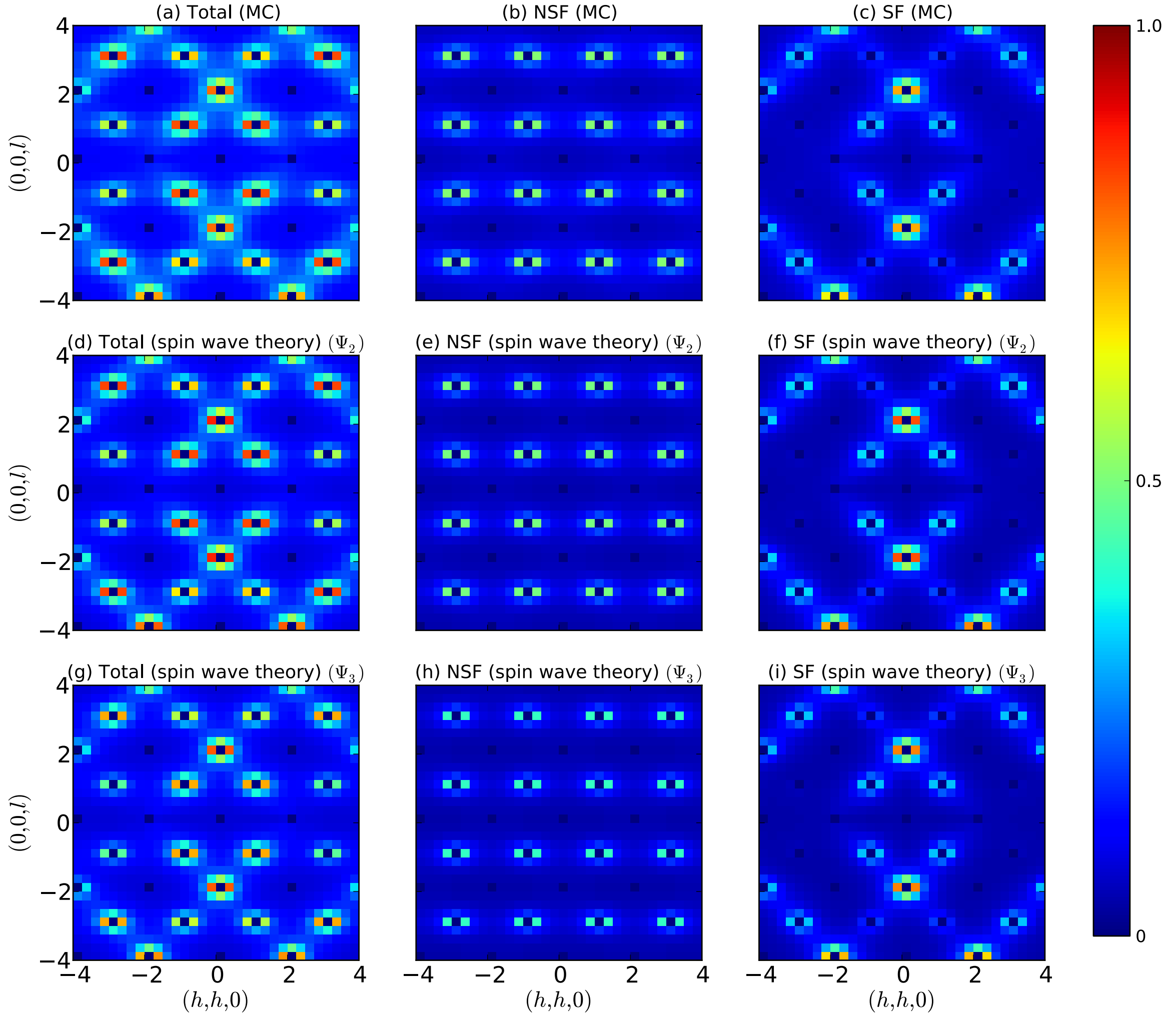

FIG. 21. Comparison between results for equal-time structure factor $S(\mathbf{q})$ obtained in classical Monte Carlo (MC) simulation and low-temperature expansion (classical spin-wave theory) for parameters appropriate to $Er_2Ti_2O_7$. (a) Total scattering in the (h,h,l) plane within MC simulation. (b) Associated scattering in the non-spin-flip (NSF) channel. (c) Associated scattering in the spin-flip (SF) channel. (d) Total scattering in the (h,h,l) plane within a spin-wave expansion about a Ψ_2 ground state. (e) Associated scattering in the NSF channel. (f) Associated scattering in the SF channel. (g) Total scattering in the (h,h,l) plane within a spin-wave expansion about a Ψ_3 ground state. (h) Associated scattering in the NSF channel. (i) Associated scattering in the SF channel. Careful comparison of the distribution of scattering in the vicinity of the $(1,1,1)$, $(3,3,3)$, and $(1,1,3)$ reciprocal lattice vectors supports the conclusion that the Ψ_2 state is preferred for these exchange parameters, in agreement with experiment and the calculations described in the text. All results were obtained at $T = 0.36$ K, for exchange parameters $J_1 = 0.11$ meV, $J_2 = -0.06$ meV, $J_3 = -0.10$ meV, setting $J_4 \equiv 0$ and g-tensor parameters $g_z = 2.45$ and $g_{xy} = 5.97$ [26]. For clarity, intensity associated with Bragg peaks at reciprocal lattice vectors has been subtracted.

of $\mathcal{H}_{\mathsf{ex}}$ [Eq. (4)]. The probability density function $P(\mathbf{m}_{\mathsf{E}})$ is sensitive both to the formation of a one-dimensional manifold of states with E symmetry—which manifests itself as a ring in $P(\mathbf{m}_{\mathsf{E}})$—and to the selection of an ordered ground state within this manifold—which will appear as six degenerate maxima within the ring.

$P(\mathbf{m}_{\mathsf{E}})$ also enables us to study the evolution of the ground-state manifolds at the boundaries between phases with competing symmetry—in this case either with T_2 or with $\mathsf{T}_{1,\mathsf{A}'}$. At these phase boundaries, $\mathbf{m}_{\mathsf{E}}$ takes on a new, constrained set of values, characteristic of the way in which different manifolds connect. For example Eqs. (53)–(55) predicts that, on the boundary with the Palmer-Chalker phase, the one-dimensional manifold of states with $|\mathbf{m}_{\mathsf{E}}| = 1$ acquires "spokes" in the directions

$$\theta_{\mathsf{E}} = \left\{0, \frac{\pi}{3}, \frac{2\pi}{3}, \pi, \frac{4\pi}{3}, \frac{5\pi}{3}\right\}$$

connecting $\mathbf{m}_{\mathsf{E}} = 0$ with the six Ψ_2 ground states. Observation of such a "spoked wheel" pattern in $P(\mathbf{m}_{\mathsf{E}})$ at finite temperature would therefore confirm that the zero-temperature degeneracies were still operative.

In an exactly parallel manner, we find that on the boundary with the ferromagnetic phase it is possible to deform the ground state continuously from Ψ_3 to a corresponding ferromagnetic state. For this reason Ψ_3 should be favored approaching the boundary with the ferromagnet (cf. Fig. 1).

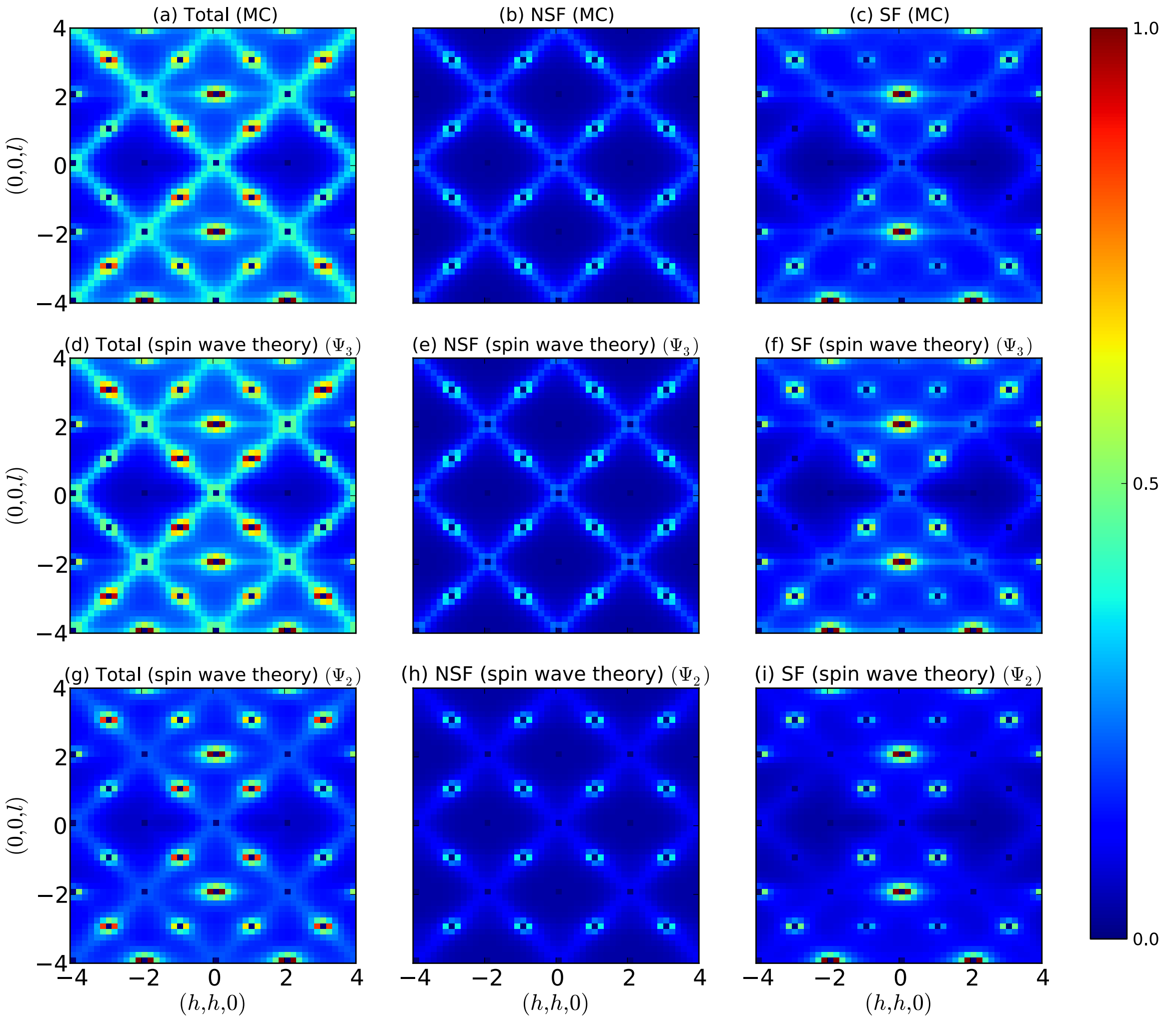

FIG. 22. Comparison between results for equal-time structure factor $S(\mathbf{q})$ obtained in classical Monte Carlo (MC) simulation and low-temperature expansion (classical spin-wave theory) in the ordered phase for parameters $J_1 = 0$, $J_2 = -1.0$ meV, $J_3 = -0.10$ meV, $J_4 \equiv 0$, approaching the noncollinear ferromagnet from within the E-symmetry phase. (a) Total scattering in the (h,h,l) plane within MC simulation showing strong rodlike features in [111] directions. (b) Associated scattering in the non-spin-flip (NSF) channel. (c) Associated scattering in the spin-flip (SF) channel. (d) Total scattering in the (h,h,l) plane within a classical spin-wave expansion about a Ψ_3 ground state, showing strong rodlike features in [111] directions. (e) Associated scattering in the NSF channel. (f) Associated scattering in the SF channel. (g) Total scattering in the (h,h,l) plane within a classical spin-wave expansion about a Ψ_2 ground state. (h) Associated scattering in the NSF channel. (i) Associated scattering in the SF channel. Comparison of the scattering supports the conclusion that the Ψ_3 ground state is found in simulation, in agreement with the results of the low-T expansion (cf. Fig. 14). An isotropic g-tensor $g_z = 1, g_{xy} = 1$ has been assumed. For clarity, intensity associated with Bragg peaks at reciprocal lattice vectors has been subtracted.

In Fig. 23 we present results for $P(\mathbf{m}_{\mathsf{E}})$ and $S(\mathbf{q})$ taken from simulations of $\mathcal{H}_{\mathsf{ex}}$ [Eq. (4)] for three sets of parameters:

$$\text{(A)} \quad (J_1,\ J_2,\ J_3,\ J_4) = (0,-0.3,-0.1,0) \quad \text{meV},$$

where we expect a Ψ_3 ground state, while approaching the border with the noncollinear FM [Figs. 23(a), 23(d), 23(g), and 23(j)]:

$$\text{(B)} \quad (J_1,\ J_2,\ J_3,\ J_4) = (0.11,0.06,-0.1,0) \quad \text{meV},$$

where we expect a Ψ_2 ground state, approaching the border with the Palmer-Chalker phase [Figs. 23(b), 23(e), 23(h), and 23(k)], and

$$\text{(C)} \quad (J_1,\ J_2,\ J_3,\ J_4) = (0.11,0.11,-0.1,0) \quad \text{meV}$$

exactly on the $T = 0$ border of the Palmer-Chalker phase [Figs. 23(c), 23(f), 23(i), and 23(l)].

The results for $S(\mathbf{q})$ shown in Figs. 23(a)–23(c), demonstrate the diffuse structure expected in the paramagnet in each case: (A) Fig. 23(a)—rods of scattering, reminiscent of those observed in $\mathrm{Yb_2Ti_2O_7}$ [20–24]; (B) Fig. 23(b)—a diffuse web of rings, reminiscent to that observed in experiments on $\mathrm{Er_2Ti_2O_7}$ [see Figs. 24(a)–24(d) for more details], also ordering in Ψ_2; (C) Fig. 23(c)—"bow-tie" patterns reminiscent of the pinch points observed in the Heisenberg antiferromagnet on a pyrochlore lattice [45]. Indeed, the Heisenberg antiferromagnet corresponds to the parameters of Fig. 23(c) with $J_3 = 0$.

The results for $P(\mathbf{m}_{\mathsf{E}})$ strongly validate our understanding of the problem in terms of degenerate ground-state manifolds,

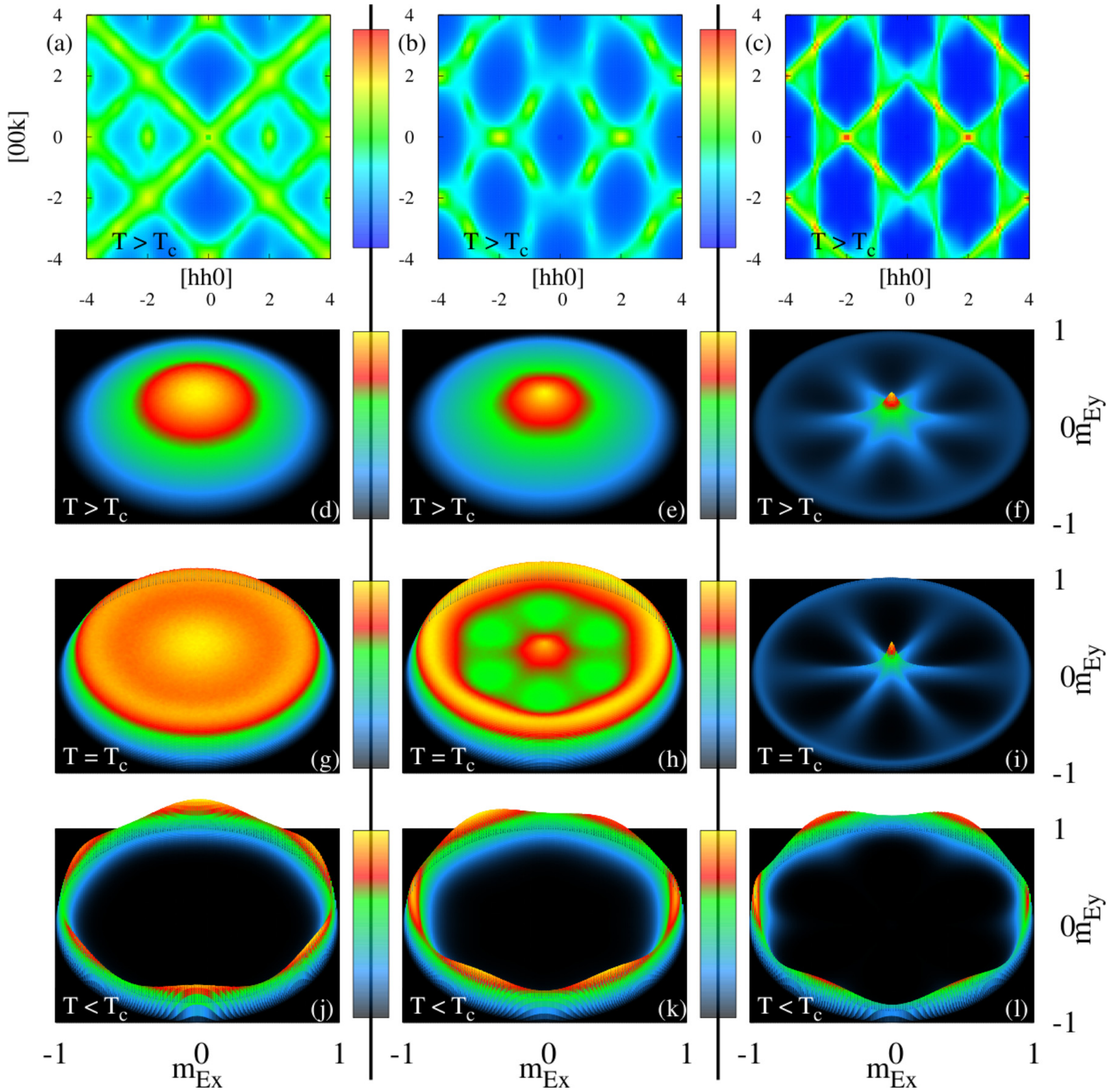

FIG. 23. Influence of ground-state degeneracy on finite-temperature phase transitions, as revealed by the probability distribution of the order parameter $\mathbf{m}_{\mathsf{E}} = m_{\mathsf{E}}\,(\cos\theta_{\mathsf{E}},\ \sin\theta_{\mathsf{E}})$ [Eq. (38)]. Results are taken from simulation of $\mathcal{H}_{\mathsf{ex}}$ [Eq. (4)], with three different sets of exchange parameters, which we label as parameter sets (A), (B), and (C). Parameter set (A), used to calculate (a), (d), (g), and (j), corresponds to a Ψ_3 ground state, approaching the noncollinear FM with $T_c = 0.39$ K. Parameter set (B), used to calculate (b), (e), (h), and (k), corresponds to a Ψ_2 ground state, with $T_c = 0.26$ K. Parameter set (C), used to calculate (c), (f), (i), and (l), corresponds to a Ψ_2 ground state, on the border of the Palmer-Chalker phase with $T_c = 0.065$ K. (a)–(c) Quasielastic scattering $S(\mathbf{q})$ in the paramagnetic phase $T > T_c$. (d)–(f) Corresponding results for the probability density function $\mathsf{P}(\mathbf{m}_{\mathsf{E}})$. (g)–(i) $\mathsf{P}(\mathbf{m}_{\mathsf{E}})$ at the transition temperature $T = T_c$. (j)–(l) $\mathsf{P}(\mathbf{m}_{\mathsf{E}})$ in the ordered phase $T < T_c$. Parameter set (A): For a finite-size system, the onset of Ψ_3 occurs progressively, through (g) the emergence of a one-dimensional manifold of states with finite $|\mathbf{m}_{\mathsf{E}}|$, and then (j) the entropic selection of θ_{E} corresponding to one of six distinct Ψ_3 ground states. (a) The connection with the noncollinear FM is evident in $S(\mathbf{q})$, with rods of scattering strongly reminiscent of those seen in $Yb_2Ti_2O_7$. Parameter set (B): The same process occurs, but in this case $\mathsf{P}(\mathbf{m}_{\mathsf{E}})$ shows that Ψ_2 ground states are favored at low temperatures (k) and even at the transition (h). Parameter set (C): On the boundary of the Palmer-Chalker phase, the ground-state manifold includes additional manifolds of states which mix $\mathbf{m}_{\mathsf{E}}$ and $\mathbf{m}_{\mathsf{T}_2}$. These are evident (f) and (i) in the spoked wheel seen in $\mathsf{P}(\mathbf{m}_{\mathsf{E}})$ at $T \geqslant T_c$, and drive the entropic selection of the Ψ_2 ground state. (c) The high degeneracy at this phase boundary is also evident in the bow-tie structure in $S(\mathbf{q})$. Further details of simulations and the parameters corresponding to (A), (B), and (C) are given in the text.

even at finite temperatures. On the border of the Palmer-Chalker phase (C) $P(\mathbf{m}_{\mathsf{E}})$ shows a diffuse spoked wheel both above T_c [Fig. 23(f)] and at T_c [Fig. 23(i)], confirming that the connection implied by the $T = 0$ ground-state manifold survives even for temperatures above the phase transition. The remnant of this spoked wheel pattern is even seen at T_c when we tune away from the phase boundary [parameter set (B)] [Fig. 23(h)]. This spoked wheel pattern in $P(\mathbf{m}_{\mathsf{E}})$ is strong evidence that the manifolds continue to be operative at T_c and play a role in ordered state selection. This perspective is consistent with the Ginzburg-Landau theory presented in Ref. [81]. And it gives new insight into *how* the terms in the Ginzburg-Landau

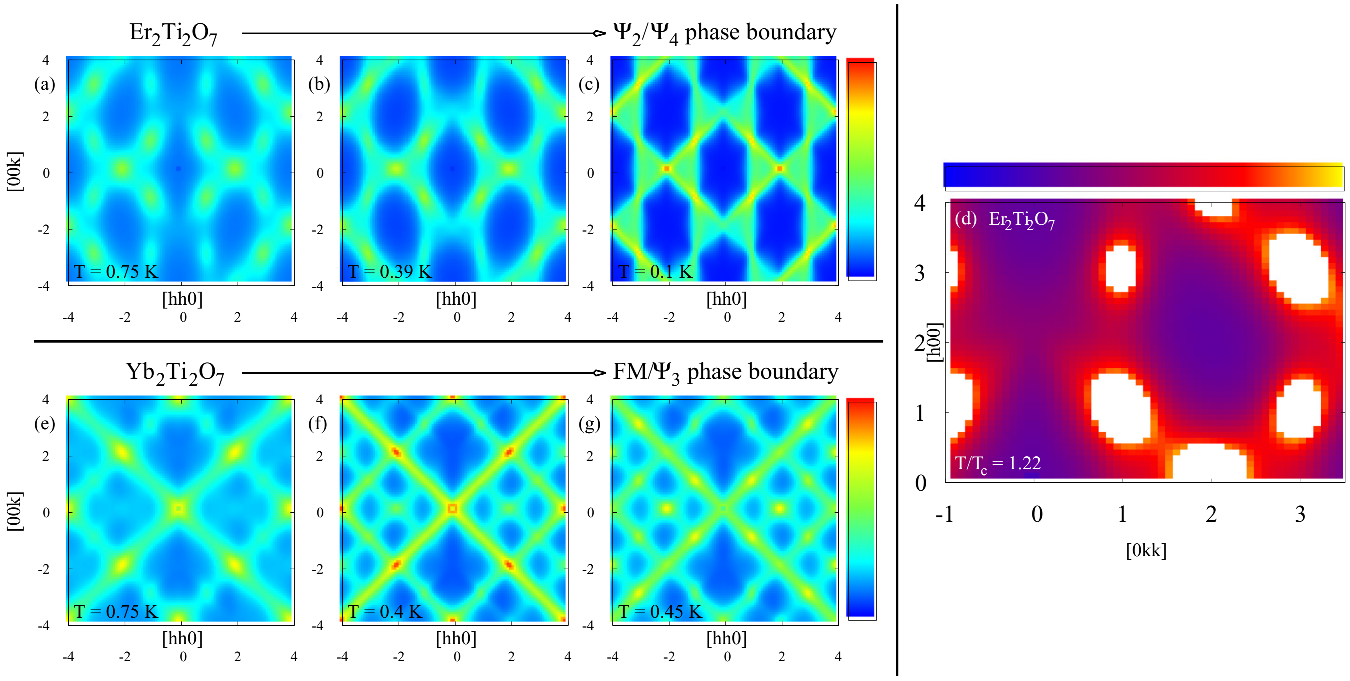

FIG. 24. Correlations in the high-temperature paramagnetic phase, as revealed by the quasielastic structure factor $S(\mathbf{q})$. (a)–(c) Results for parameters interpolating from (a) $Er_2Ti_2O_7$ [26] to (c) the boundary of the Palmer-Chalker phase (Ψ_4). The diffuse scattering characteristics of the Ψ_2 phase evolve into sharp features reminiscent of pinch points when bordering the Ψ_4 phase. Results are taken from classical Monte Carlo simulations carried out for (a) $J_2 = -0.06$ meV, $T = 750$ mK; (b) $J_2 = 0.06$ meV, $T = 390$ mK; and (c) $J_2 = 0.11$ meV, $T = 100$ mK. In all cases, $J_1 = -0.11$ meV, $J_3 = -0.1$ meV, $J_4 \equiv 0$, and $S(\mathbf{q})$ has been calculated using g-tensor parameters appropriate to $Er_2Ti_2O_7$ [26]. (d) Detail of $S(\mathbf{q})$ for parameters appropriate to $Er_2Ti_2O_7$ at $T = 616$ mK, plotted with a color scale chosen to match Fig. 14 of [94] and with the same temperature ratio $T/T_c = 1.22$ ($T_c = 505$ mK in simulations). (e)–(g) Results for parameters interpolating from $Yb_2Ti_2O_7$ [cf. Ref. ([44])], to the border of the Ψ_3 phase. The rods of scattering along [111] directions, interpreted as evidence of dimensional reduction in $Yb_2Ti_2O_7$ [22], evolve into weakly dispersing, low-energy excitations in the neighboring Ψ_3 phase. Results are taken from classical Monte Carlo simulations of $\mathcal{H}_{\rm ex}$ [Eq. (1)] for (e) $J_1 = -0.09$ meV, $T = 750$ mK; (f) $J_1 = -0.04$ meV, $T = 400$ mK; and (g) $J_1 = -0.0288$ meV, $T = 450$ mK. In all cases, $J_2 = -0.22$ meV, $J_3 = -0.29$ meV, $J_4 \equiv 0$, and $S(\mathbf{q})$ has been calculated using g-tensor parameters appropriate to $Yb_2Ti_2O_7$ [93].

theory which lift the $U(1)$ degeneracy are generated—namely by fluctuations into these low-energy manifolds.

The reason why we see the spoked wheel pattern at $T_c = 0.26$ K for parameter set (B) and not at $T_c = 0.39$ K for parameter set (A) is probably a consequence of the strong finite size dependence of the entropic selection between Ψ_2 and Ψ_3.

To conclude, we should add that where these two phase boundaries approach one another, the soft modes associated with the two different sets of manifolds compete. This leads to the complicated, reentrant behavior seen in Fig. 1, and studied for quantum spins in [46].

VII. APPLICATION TO $Er_2Ti_2O_7$

Early heat capacity measurement of $Er_2Ti_2O_7$ revealed a phase transition at $T_c = 1.25$ K, releasing an entropy $\Delta s \approx 0.97 k_B \ln 2$ per spin, consistent with the ordering of the ground-state doublet of Er [18]. Later, neutron scattering studies revealed the nature of the low temperature order, finding it to correspond to the Ψ_2 configurations illustrated in Fig. 10 [25,26,65].

The selection of the Ψ_2 states in $Er_2Ti_2O_7$ out of the 1D manifold of states transforming with E symmetry has been identified as a textbook example of order-by-disorder [25], with quantum zero-point fluctuations [26,27,46], low-temperature classical thermal fluctuations [82], and thermal fluctuations near the ordering temperature [28,77] all favoring Ψ_2 order. A corollary of this conclusion is that there should be a small, fluctuation induced, gap at $\mathbf{q} = 0$ in the spin-wave spectrum. And such a gap has now been observed in inelastic neutron scattering [95]. We note that an alternative scenario has been proposed in which the selection of Ψ_2 comes instead from virtual fluctuations into higher crystal field levels [29,43,96]. Thus it may in fact be that the selection of Ψ_2 has multiple contributions, both from harmonic fluctuations of the ground-state order and from virtual crystal field fluctuations.

Here, using the exchange parameters for $Er_2Ti_2O_7$ taken from [26], we confirm that thermal fluctuations of classical Heisenberg spins select a Ψ_2 phase at finite temperature. Estimates from our Monte Carlo simulations give $T_c \approx 500$ mK (Fig. 18), somewhat lower than both experiments and those obtained in a high temperature series expansion of the quantum spin model [28]. But within the paramagnetic phase, our simulations of the spin structure factor $S(\mathbf{q})$ are in excellent agreement with neutron scattering measurements [94] showing the build-up of long-range order, as can be seen from the comparison between Fig. 24(d) of this work and Fig. 14 of Ref. [94].

A question which remains is *why* fluctuations should favor Ψ_2 in the case of $Er_2Ti_2O_7$ and more generally why they should favor either Ψ_2 or Ψ_3 for a given set of exchange parameters $\{J_i\}$. Our work provides the answer to this question and, in so doing, underlines how the properties of a frustrated magnet are strongly influenced by competing phases.

The mechanism by which the Ψ_2 states are selected is inherited from the phase boundary with the neighboring Palmer-Chalker phase. At this boundary three additional continuous sets of ground states appear connecting the six Palmer-Chalker ground states, to the 1D manifold of E symmetry states (Fig. 13). The points in configuration space at which these sets of ground states meet are none other than the Ψ_2 configurations. Due to their favored position at the junctions of the ground-state manifold the Ψ_2 states gain additional soft modes and are selected by fluctuations in the region approaching the boundary with the Palmer-Chalker phase. The consequences of these connected manifolds are visible even in finite temperature simulations as shown in Fig. 23.

It is worth noting that an exactly parallel mechanism selects the Ψ_3 states for parameters proximate to the ferromagnetic phase. In the region proximate to both Palmer-Chalker and ferromagnetic phases, a complicated reentrant behavior is observed [46] (Fig. 1).

Our work shows that the preference of fluctuations for Ψ_2 ordering in $Er_2Ti_2O_7$ is a property inherited from a nearby phase boundary where the Ψ_2 states sit at the junctions of a connected ground-state manifold. In the context of this result it is interesting to ask how the spin correlations evolve as the exchange parameters are tuned from those appropriate to $Er_2Ti_2O_7$ to the boundary of the Palmer-Chalker phase. This is illustrated using Monte Carlo simulations of the spin structure factor $S(\mathbf{q})$ in Figs. 24(a)–24(c). For the parameters appropriate to $Er_2Ti_2O_7$, our simulations reproduce the smooth features observed in experiment. As the phase boundary is approached these smooth features evolve into sharp, pinch-point-like features, associated with the large ground-state manifold on the phase boundary. In the limit $J_3 \to 0$ these pinch-point-like features become the pinch points associated with the Coulomb phase of the $O(3)$ Heisenberg model on the pyrochlore lattice [45].

Our study of the ground-state selection in $Er_2Ti_2O_7$ emphasises that the properties of frustrated magnets can be strongly influenced by the soft modes appearing on nearby boundaries. This same essential insight also manifests itself—in rather different ways—in the study of $Yb_2Ti_2O_7$ and $Er_2Sn_2O_7$, to which we now turn.

VIII. APPLICATION TO $Yb_2Ti_2O_7$

Like its sister compound $Er_2Ti_2O_7$, $Yb_2Ti_2O_7$ was first identified as undergoing a finite temperature ordering transition in the heat capacity study by Blöte *et al.*, nearly 50 years ago [18]. That study revealed a sharp anomaly in the heat capacity at $T_c = 0.214$ K, with a corresponding release of entropy of $\Delta s = 0.97 k_B \ln 2$ per spin. Since then, the presence of this phase transition in stoichiometric $Yb_2Ti_2O_7$ has been debated in the literature, with different groups, with different samples, reporting differing results for the presence or absence of magnetic order. Nevertheless, it is now widely accepted that stoichiometric $Yb_2Ti_2O_7$ undergoes a thermodynamic phase transition into a state with finite magnetization at a temperature $T_c \sim 0.2$ K [24,66,68,69,71–74,97,98].

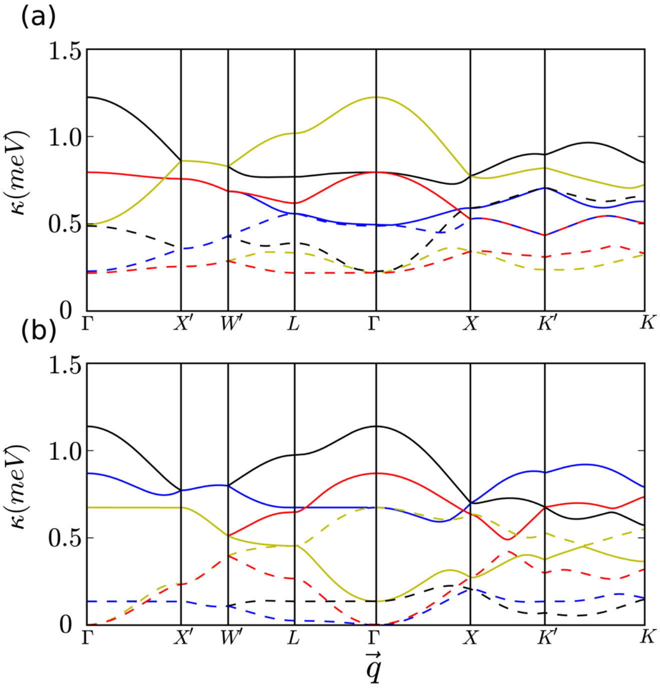

FIG. 25. Spin-wave dispersion calculated within a classical, low-temperature expansion, showing dimensional reduction of a subset of excitations. (a) Excitations of the FM ground state, for exchange parameters appropriate to $Yb_2Ti_2O_7$, i.e., $J_1 = -0.09$ meV, $J_2 = -0.22$ meV, $J_3 = -0.29$ meV, setting $J_4 = 0$. The ferromagnet possesses a flat band in the (h,h,h) $(\Gamma \to L)$ direction at energy $\Delta \approx 0.22$ meV, which gives rise to rods in the equal time structure factor (cf. Fig. 20). (b) Excitations of the Ψ_3 ground state, for exchange parameters on the boundary between the Ψ_3 and FM phases, i.e., $J_1 = -0.029$ meV, $J_2 = -0.22$ meV, $J_3 = -0.29$ meV with $J_4 = 0$. The Ψ_3 phase, on the phase boundary, also possesses a quasiflat band along (h,h,h), which in this case is gapless at the Γ point of the Brillouin zone. This leads us to suggest that the low-energy rodlike features observed in the paramagnetic phase of $Yb_2Ti_2O_7$ arise from its proximity in parameter space to the Ψ_3 phase and the low-energy modes which are present on the phase boundary (see discussion in Sec. VIII).

For the parameters given by Ross *et al.* [44], the theory developed in Sec. III predicts that $Yb_2Ti_2O_7$ has a $\mathbf{q} = 0$ ground state, with noncollinear order ferromagnetic order. This "splayed ferromagnet" is consistent with the interpretation of neutron scattering experiments given in [68,71–73]. An ordered ground state of this type would normally be expected to support coherent, dispersing spin-wave excitations, with a finite gap coming from the anisotropy of exchange interactions, as illustrated in Figs. 25 and 26.

Curiously, however, gapped, coherent spin waves have yet to be observed in $Yb_2Ti_2O_7$, with a succession of experiments reporting a broad, gapless continuum at low temperatures [21,71–73]. The origin of this gapless continuum remains a puzzle, although the presence of competing classical ordered phases must ultimately impact on quantum excitations [70]. It

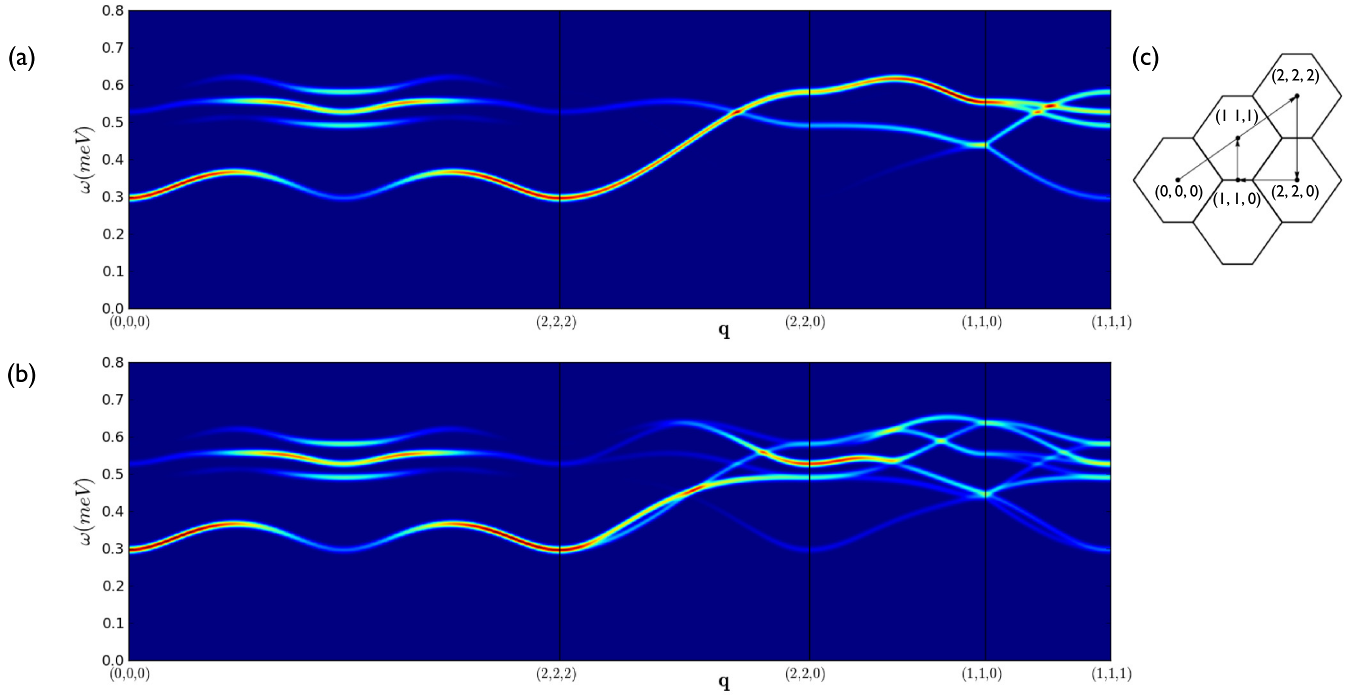

FIG. 26. Prediction for the spin-wave excitations of the ferromagnetically ordered ground state of $Yb_2Ti_2O_7$, calculated within linear spin-wave theory for the parameters given by Ross *et al.* [44]. (a) Spin-wave dispersion for a single ferromagnetic domain with magnetization parallel to [100], showing a minimum gap to excitations $\Delta \sim 0.3$ meV, occurring in the zone center. (b) Spin-wave dispersion averaged over the six possible ferromagnetic domains. (c) Path in reciprocal space used in making plots. Calculations were carried out for the anisotropic exchange model $\mathcal{H}_{\textsf{ex}}$ [Eq. (1)], with results convoluted with a Gaussian of full width at half maximum 0.014 meV to mimic finite experimental resolution. The relative intensity of scattering is shown in false color. Details of calculations are given in Sec. IV C and Appendix B.

is also important to recall that the ordered ground state breaks only the point-group symmetries of the anisotropic exchange model $\mathcal{H}_{\textsf{ex}}$ [Eq. (1)], and so spin waves cannot be interpreted as Goldstone modes. It follows that interaction effects may play an important role, even at low orders in $1/S$. And it is interesting to note that the broad continuum observed in experiment has more in common with semiclassical simulations of the spin excitations of the paramagnetic phase of $Yb_2Ti_2O_7$ [73,99], than with the linear spin-wave excitations of the ground state, as shown in Fig. 26. This point will be discussed further elsewhere [99].

While the nature of the ground state of $Yb_2Ti_2O_7$ has proved controversial, and the associated excitations remain to be understood, all neutron-scattering experiments agree about the signature feature of its paramagnetic phase—striking "rodlike" structures along the $\langle 111 \rangle$ directions of reciprocal space. First observed more than ten years ago [20], these rods of scattering have since been interpreted as evidence of dimensional reduction [21,22] and, in the context of $\mathcal{H}_{\textsf{ex}}$ [Eq. (1)], as evidence of significant anisotropic exchange interactions [23,44,50]. They are a robust feature of $S(\mathbf{q})$, as calculated from $\mathcal{H}_{\textsf{ex}}$ [Eq. (1)] within both the (semiclassical) random phase approximation [23,24], and classical Monte Carlo simulations [70] (Fig. 24). However, despite their ubiquity, the origin of these rods of scattering remains mysterious.

To understand the origin of the rods of scattering we must once again look to the influence of the phase boundaries. The classical ground states of $\mathcal{H}_{\textsf{ex}}$ reduce to a set of independent kagome planes on the boundary between FM and Palmer-Chalker phases, and to a set of independent chains on the boundary between the Ψ_2 and Palmer-Chalker phases. However the rods of scattering seen in $Yb_2Ti_2O_7$ occur for parameters where the ground state of $\mathcal{H}_{\textsf{ex}}$ is expected to be ordered and fully three dimensional [44]. Indeed, our classical Monte Carlo simulations predict that $Yb_2Ti_2O_7$ orders at 450 mK (cf. Fig. 17), a little higher than the $T_c \approx 200$ mK found in experiment.

Within the scenario of multiple-phase competition, rods of scattering can be traced back to dimensionally reduced excitations, due to quasidegenerate lines of low-lying spin-wave excitations, which evolve into low-lying excitations of Ψ_3 on the boundary between the FM and the Ψ_3 phases (cf. Fig. 25). This progression is also clear in the evolution of $S(\mathbf{q})$ from parameters appropriate to $Yb_2Ti_2O_7$ [Fig. 24(e)] to the border of the Ψ_3 phase [Fig. 24(g)], also shown in Ref. [70].

Seen in this light, the observation of rods of scattering in $Yb_2Ti_2O_7$ is a consequence of the proximity of competing ordered states—in this case the Ψ_2 and Ψ_3 states. The importance of these competing ground states in driving the unusual physics of $Yb_2Ti_2O_7$ has been underlined in recent work [70,73]. In Ref. [70] it was shown that both quantum and thermal fluctuations bring the phase boundary between ferromagnetic and $\textsf{E}$ symmetry phases closer to the parameter regime appropriate to $Yb_2Ti_2O_7$. In this sense, $Yb_2Ti_2O_7$ really is a material "living on the edge" between differing magnetic orders, and the rods of scattering are a manifestation of this.

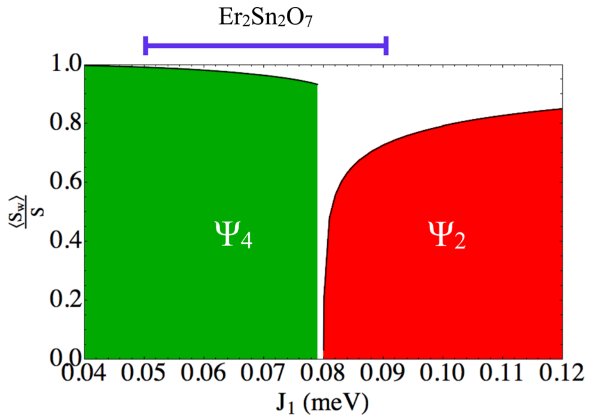

FIG. 27. Ordered moment in the region of parameter space relevant to $Er_2Sn_2O_7$, as calculated in linear spin-wave theory. On the Palmer-Chalker (Ψ_4) side of the phase boundary, the quantum correction to the ordered moment is small. However, the correction diverges on the approach the phase boundary from the noncoplanar antiferromagnet (Ψ_2), indicating the possibility of a region of quantum disorder between these two phases. Experimental estimates of exchange parameters in $Er_2Sn_2O_7$ [34] place it close to this phase boundary, making it a good candidate for the observation of quantum spin-liquid physics. Calculations were carried out for the anisotropic exchange model $\mathcal{H}_{\mathrm{ex}}$ [Eq. (1)], as described in Sec. IV C and Appendix B, with parameters $J_2 = 0.08$ meV, $J_3 = -0.11$ meV taken from [34], setting the Dzyaloshinskii-Moriya interaction $J_4 = 0$. The error bars on the estimated value of J_1 are taken from Ref. [34].

IX. APPLICATION TO $Er_2Sn_2O_7$

Like $Er_2Ti_2O_7$ and $Yb_2Ti_2O_7$, the magnetic ions in $Er_2Sn_2O_7$ have a Kramers doublet ground state [30,100], and their interactions are believed to be well described by $\mathcal{H}_{\mathrm{ex}}$ [Eq. (1)] [34]. Correlations reminiscent of the Palmer-Chalker phase have been observed in neutron scattering [34], and magnetization measurements show some evidence of spin freezing at low temperatures [34]. Nonetheless, $Er_2Sn_2O_7$ shows no evidence of magnetic order, in thermodynamic measurements [33,34], μSR [31], or neutron scattering [33,34], down to a temperature of 20 mK [31].

The exchange parameters determined for $Er_2Sn_2O_7$ in Ref. [34] would place it extremely close to the phase boundary between the Palmer-Chalker and Ψ_2 states (Fig. 1). Classical Monte Carlo simulations with this parameter set predict a phase transition into the Palmer-Chalker state at $T_c \approx 200$ mK. However, we can once more gain further insight by looking at the behavior of the model $\mathcal{H}_{\mathrm{ex}}$ approaching the phase boundary.

As the phase boundary is approached, the ground-state value of the ordered moment, as calculated in linear spin-wave theory, is reduced by quantum fluctuations. This is illustrated in Fig. 27. Approaching the boundary from the Palmer-Chalker side, this quantum correction is small. However, approaching the boundary from the Ψ_2 side, the correction is logarithmically divergent. Since spin-wave theory typically underestimates quantum effects, this divergence is a likely indicator of a region of quantum disorder between the Palmer-Chalker and Ψ_2 region of the phase diagram (cf. Fig. 2). The placement of $Er_2Sn_2O_7$ immediately adjacent to this classical phase boundary thus makes it a prime candidate for the observation of quantum spin-liquid physics.

We can see therefore that the competition between Palmer-Chalker and Ψ_2 ordering in $Er_2Sn_2O_7$ enhances quantum fluctuations in that material and may even stabilize a quantum disordered state. Such a scenario would be consistent with the lack of observed magnetic order in $Er_2Sn_2O_7$ and would make $Er_2Sn_2O_7$ the first example of a pyrochlore spin liquid with dominantly XY-like interactions. While the recent years have seen considerable theoretical advances in the understanding of quantum spin-liquid states occurring close to the Ising (spin-ice) limits of $\mathcal{H}_{\mathrm{ex}}$ [5–11], the limit of dominant XY interactions has been much less explored for quantum spins. A deeper understanding of $Er_2Sn_2O_7$ calls for further work in this direction.

X. OTHER PYROCHLORE MAGNETS

The family of rare-earth pyrochlore oxides $R_2M_2O_7$ is very diverse [17], and it is becoming even more so, with high-pressure synthesis techniques allowing for many new combinations of rare-earth R and transition metal M to be realized [101]. In this section we briefly explore the properties of further examples of pyrochlore magnets. We will mostly restrict our comments to materials based on the Kramers ions such as Er^{3+}, Yb^{3+}, where the model $\mathcal{H}_{\mathrm{ex}}$ [Eq. (1)], with couplings of the form of $\mathbf{J}_{01}$ [Eq. (6)], offers a completely a completely general description of nearest-neighbor interactions on the pyrochlore lattice. That said, many of the same physical phenomena arise in pyrochlore magnets based on non-Kramers ions and, where these have a doublet ground state, interactions may also be described using $\mathcal{H}_{\mathrm{ex}}$ [8,52]. With this in mind, we also make a few brief comments about materials based on the non-Kramers ions Tb^{3+} and Pr^{3+}.

$Yb_2Sn_2O_7$ [35,36,102] and $Yb_2Pt_2O_7$ [39] have both been identified as having ferromagnetic ground states, and may therefore be placed in the noncollinear ferromagnet (T_1) region of our phase diagram. Meanwhile, the ground state of another Yb based system, $Yb_2Ge_2O_7$ has been shown in neutron scattering experiments to belong to the manifold of E symmetry states, although any ground-state selection between Ψ_2 and Ψ_3 configurations has yet to be determined [103,104]. The progression, as a function of decreasing transition metal ionic radius Sn → Pt → Ti → Ge for the $Yb_2M_2O_7$ compounds thus tunes across the phase boundary between the ferromagnetic and Ψ_2/Ψ_3 regions in Fig. 1 [70,103]. The spin excitations above these ordered states remain a puzzle, however, with a recent systematic study of the Sn, Ti, and Ge compounds showing an absence of coherent spin waves in all three materials, and a continuity of the inelastic neutron scattering spectrum across the finite temperature ordering transition in each case [72].

Amongst Er based pyrochlores, $Er_2Ge_2O_7$ has been observed to order antiferromagnetically at $T_N = 1.41$ K [38]. Neutron scattering experiments reveal this to belong to the Ψ_2/Ψ_3 region of the phase diagram in Fig. 1. The behavior of the intensity of the magnetic Bragg peaks under external magnetic field suggests that fluctuations select a Ψ_3 ground state out of the E symmetry manifold for $Er_2Ge_2O_7$ [38].

$Er_2Pt_2O_7$ also orders antiferromagnetically at $T_N = 0.3$ K. If the variation of exchange constants with the size of the transition metal ion M is montonic, then it would be expected for this material to lie near the boundary between the Ψ_2 and Palmer-Chalker regions of the phase diagram in Fig. 1. However, this assumption could fail in the case of $Er_2Pt_2O_7$ since Pt^{4+} ion differs from $\{Ti^{4+}, Sn^{4+}, Ge^{4+}\}$ in that it possesses a partially filled d shell [39,105].

The Gd based pyrochlores $Gd_2M_2O_7$ have attracted significant research interest over a period of nearly two decades [17,106]. The physics of these pyrochlores is somewhat different from, e.g., Yb and Er based systems, because the Gd^{3+} ions have vanishing orbital angular momentum $L = 0$. The interactions of the $S = 7/2$ Gd spins are thus quite isotropic, and the nearest-neighbor anisotropic exchange which is the focus of this article is a less important consideration than further neighbor interactions—including dipole-dipole interactions. Nevertheless, combining the effect of nearest-neighbor antiferromagnetic exchange and the nearest-neighbor part of the dipole-dipole interaction our theory does predict a Palmer-Chalker ground state which is consistent with observations on $Gd_2Sn_2O_7$ [107,108].

In $Gd_2Ti_2O_7$ further neighbor interactions drive a complex phenomenology involving multiple phase transitions and “partially ordered” states [109–112]. The precise nature of the magnetic ground state remains a matter of discussion in the literature [113], and is beyond the scope of the present study. Recently, another Gd pyrochlore, $Gd_2Pb_2O_7$ has been synthesised presenting an antiferromagnetic ordering transition at $T = 0.81$ K into an as yet unidentified ground state [114].

Nd based pyrochlores have attracted considerable recent attention and provide examples of all-in, all-out ordering on the pyrochlore lattice [84,115–117]. In particular, it has recently come to light that $Nd_2Zr_2O_7$ exhibits the novel phenomenon of “moment fragmentation” in which the spin correlations simultaneously show the pinch points of a Coulomb phase and the Bragg peaks of an ordered state [118–120]. However, we note that the ground doublet of the Nd ions is of the dipolar-octupolar type [84,117]. In this case, the anisotropic exchange interactions would have a different form to Eq. (6) [53]. Recently, a Ce based pyrochlore $Ce_2Sn_2O_7$, also believed to belong to the group of dipolar-octupolar pyrochlores, has been synthesized which appears to show an absence of magnetic order down to $T = 0.02$ K [40], suggesting it as a promising candidate spin-liquid system.

There are also many pyrochlore systems where the rare-earth ion R is a non-Kramers ion, such as Tb^{3+} or Pr^{3+} [17]. Many of these systems also exhibit twofold degenerate crystal field ground states, and a pseudospin-1/2 description of the magnetic degrees of freedom may be appropriate [52,121,122] (although in the Tb^{3+} systems the picture is complicated by the relatively small gap to crystal field excitations [123–125]). In this case the nearest-neighbor bilinear exchange Hamiltonian for these pseudospins takes the form of Eq. (8), with the constraint that $\mathsf{J}_{z\pm} = 0$ [8,52]—cf. Table II. The pseudospin $\mathbf{S}$ must also be interpreted differently in this case with the part of the pseudospin perpendicular to the local [111] directions corresponding to a quadrupolar degree of freedom. Thus, an “easy plane” order of the pseudospins (as occurs in the E and T_2 regions of our phase diagram) actually corresponds to quadrupolar order for non-Kramers ions.

Among the Tb pyrochlores, $Tb_2Sn_2O_7$ is known to exhibit ferromagnetic order [75,76,126] and therefore belongs to the T_1 region of the phase diagram. $Tb_2Ti_2O_7$, meanwhile, has been studied for a long time as a candidate spin liquid [127,128] exhibiting power-law spin correlations [129,130]. The apparent spin-liquid behavior has been linked with quantum spin-ice physics [55], but it has recently been proposed that an alternative form of spin-liquid physics may be at work [48]. Recent studies have also revealed the presence of competing ordered states, with quadrupolar order (corresponding to a Palmer-Chalker-like configuration of the pseudospins [131,132]) and antiferromagnetic $\mathbf{q} = (1/2,1/2,1/2)$ order [133,134] observed depending on the sample details and the experimental cooling protocol. $Tb_2Ge_2O_7$ has recently come to light as another system of interest for spin-liquid physics, with no long-range order observed down to 20 mK and short-range ferromagnetic correlations [135]. This may suggest that $Tb_2Ge_2O_7$ lives in a region of disorder, proximate to the ferromagnetic (T_1) phase, such as that proposed in Ref. [48].

At the same time, the Pr based pyrochlores $Pr_2M_2O_7$ (M = Sn, Zr, Hf, Pb) have emerged as promising candidates for quantum spin-ice physics, exhibiting an absence of magnetic order and dynamic, spin-ice-like correlations [114,136–138].

XI. CONCLUSION

Rare-earth pyrochlore oxides offer a veritable treasure trove of novel physical phenomena, ranging from classical and quantum spin liquids, to dimensional reduction, and phases governed by order-by-disorder effects. In this article we have established a general theory of multiple-phase competition in materials with anisotropic exchange interactions on the pyrochlore lattice, and shown how it can be can be applied to three specific materials: $Er_2Ti_2O_7$, $Yb_2Ti_2O_7$, and $Er_2Sn_2O_7$. The recurring theme throughout this analysis is of materials living on the edge, in the sense of having properties which are dictated by the competition between neighboring forms of magnetic order.

Starting from a very general model of interactions between nearest-neighbor spins on the pyrochlore lattice $\mathcal{H}_{\mathsf{ex}}$ [Eq. (1)], we have used an analysis based on point-group symmetry to establish the exact, classical, ground-state phase diagram (Secs. II and III). As a by-product, we provide a complete classification of possible 4-sublattice ordered states, according to the way they lift the symmetry of a single tetrahedron. Moreover, using the Lego-brick rules developed in Sec. II E, we are able to identify the conditions under which the classical ground-state manifold undergoes a dimensional reduction into independent planes or chains of spins, opening the door to new physical phenomena.

We have given particularly careful consideration to the ground-state manifolds in the limit where the symmetric off-diagonal exchange $J_3 < 0$ and the Dzyaloshinskii-Moriya interaction $J_4 = 0$ (Sec. III). Based on the experimental parametrizations of exchange interactions for Kramers pyrochlores [26,34,44], this limit is of particular experimental relevance. We have elucidated the nature of the expanded ground-state manifolds which occur at the phase boundaries of this model, and it is these which drive much of the physics of the surrounding regions of parameter space.

Stepping out of the ground-state manifold, we have given, in Sec. IV, calculations of the spin-wave excitations in the ordered phases. Among other things, this allows us to determine the ground-state selection by both quantum and thermal fluctuation and to identify regions of the phase diagram where classical order will be melted by quantum fluctuations.

We have also studied the finite-temperature properties of the anisotropic exchange model [Eq. (1)] using classical Monte Carlo simulations, presented in Secs. V and VI. These simulations make it possible to determine the finite temperature phase diagram (Fig. 3) and to show how the expanded ground-state manifolds on the phase boundaries manifest themselves at finite temperature (Fig. 23).

The implications of our theory for three specific pyrochlore materials—$Er_2Ti_2O_7$, $Yb_2Ti_2O_7$, and $Er_2Sn_2O_7$—are expounded in Secs. VII, VIII, and IX. We find that the influence of nearby phase boundaries accounts for the ground-state selection by fluctuations in $Er_2Ti_2O_7$, the apparent dimensional reduction in the paramagnetic phase of $Yb_2Ti_2O_7$, and the suppression of magnetic order in $Er_2Sn_2O_7$. The unusual properties of these three materials can be understood as living on the edge—having properties controlled by the competition between different ground states.

As discussed in Sec. X, the family of rare-earth pyrochlore magnets is a large one, extending well beyond the three materials covered in Secs. VII to IX. In particular, recent work has seen the synthesis of rare-earth pyrochlores $R_2M_2O_7$ with M = Ge, Pt, Pb, Os, Zr, Hf [38,39,114,138–140]. This work suggests the possibility to move around the phase diagram shown in Figs. 1 and 2, using chemical or physical pressure. This would be particularly interesting in cases where systems related by a change of transition metal ion M live on opposite sides of a classical phase boundary. One might then hope to tune through a region of strong quantum fluctuations using substitution of the transition metal ion. Such an opportunity would seem to present itself for $Er_2M_2O_7$ with M = Sn, Ti, and $Yb_2M_2O_7$ with M = Ge, Ti [70].

Our analysis may also be useful in the study of related systems, such as the rare-earth spinel $CdEr_2Se_4$ [141], where the Er ions also form a pyrochlore lattice. Looking further afield, a modification of our theory could be used in the understanding of "breathing" pyrochlore compounds, where the tetrahedra of the pyrochlore lattice alternate in size [142–145]. It is also interesting to note recent neutron scattering experiments on $NaCaCo_2F_7$, a pyrochlore material with quenched exchange disorder [146]. The observed diffuse scattering in that material is rather similar to that predicted by our Monte Carlo simulations in Fig. 24(b). This may spring from a connection between the low-energy configurations found in the clean limit of the anisotropic exchange model, studied in this article, and the low-energy configurations of the disordered system.

From a theoretical perspective, our work also highlights the importance of large, classical, ground-state degeneracies which are *not* related to the well-studied examples of spin ice, or of the Heisenberg antiferromagnet on a pyrochlore lattice. These degeneracies, which emerge in a number of different limits of $\mathcal{H}_{\text{ex}}$ [Eq. (1)], could lead to novel forms of classical or quantum spin liquid, as well as entirely new forms of classical and quantum order [49]. One such case, where fluctuations lead to a spin liquid described by a rank-2 tensor field with a continuous gauge symmetry, has been developed in Ref. [48]. However, there are many other regions of parameter space where strong fluctuations persist to low temperature [147], and the majority of these have yet to be fully explored. It seems that the study of rare-earth pyrochlore magnets with anisotropic exchange interactions may have many more surprises yet in store.

ACKNOWLEDGMENTS

The authors are pleased to acknowledge helpful conversations with Bruce Gaulin, Michel Gingras, Alannah Hallas, Edwin Kermarrec, Isabelle Mirebeau, Sylvain Petit, Karlo Penc, and Kate Ross, and a critical reading of the manuscript by Mathieu Taillefumier. This work was supported by the Theory of Quantum Matter Unit of the Okinawa Institute of Science and Technology Graduate University.

APPENDIX A: *g* TENSOR IN LOCAL AND GLOBAL COORDINATE FRAMES

The local crystal-electric field (CEF), acting on a given magnetic ion, affects both the character of its ground state, and the nature of its exchange interactions with other magnetic ions. For this reason, it is often convenient chose a coordinate frame

$$\{\mathbf{x}_i^{\text{local}},\mathbf{y}_i^{\text{local}},\mathbf{z}_i^{\text{local}}\},$$

which is tied to the local CEF on site i. We can accomplish this by choosing $\mathbf{z}_i^{\text{local}}$ to be parallel with the [111] axis on site i, i.e., the local axis with C_3 symmetry

For the tetrahedron shown in Fig. 5, the magnetic ions labeled S_0, S_1, S_2, and S_3 occupy positions

$$\mathbf{r}_0 = \frac{a}{8}(1,1,1), \quad \mathbf{r}_1 = \frac{a}{8}(1,-1,-1),$$
$$\mathbf{r}_2 = \frac{a}{8}(-1,1,-1), \quad \mathbf{r}_3 = \frac{a}{8}(-1,-1,1), \tag{A1}$$

relative to the center of the tetrahedron, in units such that the cubic, 16-site unit cell of the pyrochlore lattice occupies a volume $V = a^3$. The local [111] axes on these sites are given by

$$\mathbf{z}_0^{\text{local}} = \frac{1}{\sqrt{3}}(1,1,1), \quad \mathbf{z}_1^{\text{local}} = \frac{1}{\sqrt{3}}(1,-1,-1),$$
$$\mathbf{z}_2^{\text{local}} = \frac{1}{\sqrt{3}}(-1,1,-1), \quad \mathbf{z}_3^{\text{local}} = \frac{1}{\sqrt{3}}(-1,-1,1). \tag{A2}$$

In defining $(\mathbf{x}_i^{\text{local}},\mathbf{y}_i^{\text{local}})$ we follow the conventions of Ross *et al.* [44], and make the convenient choice

$$\mathbf{x}_0^{\text{local}} = \frac{1}{\sqrt{6}}(-2,1,1), \quad \mathbf{x}_1^{\text{local}} = \frac{1}{\sqrt{6}}(-2,-1,-1),$$
$$\mathbf{x}_2^{\text{local}} = \frac{1}{\sqrt{6}}(2,1,-1), \quad \mathbf{x}_3^{\text{local}} = \frac{1}{\sqrt{6}}(2,-1,1), \tag{A3}$$

TABLE VI. Estimates of the components of the g tensor in the local frame $\mathbf{g}_{\mathsf{local}}$ [Eq. (A6)], taken from experiment on $Yb_2Ti_2O_7$ [93], $Er_2Ti_2O_7$ [26], and $Er_2Sn_2O_7$ [34].

	$Yb_2Ti_2O_7$	$Er_2Ti_2O_7$	$Er_2Sn_2O_7$
g_{xy}	4.18	5.97	7.52
g_z	1.77	2.45	0.05

such that all $\mathbf{y}_i^{\mathsf{local}}$ lie in a common plane

$$\mathbf{y}_0^{\mathsf{local}} = \frac{1}{\sqrt{2}}(0,-1,1), \quad \mathbf{y}_1^{\mathsf{local}} = \frac{1}{\sqrt{2}}(0,1,-1),$$
$$\mathbf{y}_2^{\mathsf{local}} = \frac{1}{\sqrt{2}}(0,-1,-1), \quad \mathbf{y}_3^{\mathsf{local}} = \frac{1}{\sqrt{2}}(0,1,1). \tag{A4}$$

In this local coordinate frame, the magnetic moment

$$m_i^\alpha = \sum_{\beta=1}^{3} g_{\mathsf{local}}^{\alpha\beta} \mathsf{S}_i^\beta \tag{A5}$$

is connected to the (pseudo)spin-1/2 operator S_i^α [Eq. (7)], through a g tensor with a diagonal simple form

$$\mathbf{g}_{\mathsf{local}} = \begin{pmatrix} g_{xy} & 0 & 0 \\ 0 & g_{xy} & 0 \\ 0 & 0 & g_z \end{pmatrix}, \tag{A6}$$

where α, $\beta = \{\mathbf{x}_i^{\mathsf{local}},\mathbf{y}_i^{\mathsf{local}},\mathbf{z}_i^{\mathsf{local}}\}$, and $\mathbf{g}_{\mathsf{local}}$ is independent of the site considered. Estimates of g_{xy} and g_z, taken from experiment on $Yb_2Ti_2O_7$ [93], $Er_2Ti_2O_7$ [26], and $Er_2Sn_2O_7$ [34], are shown in Table VI. For rare-earth ions with Ising character, such as Dy^{3+} in $Dy_2Ti_2O_7$, $g_z > g_{xy}$, while for the rare-earth ions considered in this paper with easy-plane character, $g_z < g_{xy}$.

The g tensor in the coordinate frame of the crystal axes $\mathbf{g}_i$ [Eq. (3)] can be found by rotating $\mathbf{g}_{\mathsf{local}}$ [Eq. (A6)] back into the global coordinate frame μ, $\nu = \{\mathbf{x},\mathbf{y},\mathbf{z}\}$. Since the required rotation depends on the lattice site, the resulting g tensor is sublattice dependent

$$\mathbf{g}_0 = \begin{pmatrix} g_1 & g_2 & g_2 \\ g_2 & g_1 & g_2 \\ g_2 & g_2 & g_1 \end{pmatrix}, \quad \mathbf{g}_1 = \begin{pmatrix} g_1 & -g_2 & -g_2 \\ -g_2 & g_1 & g_2 \\ -g_2 & g_2 & g_1 \end{pmatrix},$$
$$\mathbf{g}_2 = \begin{pmatrix} g_1 & -g_2 & g_2 \\ -g_2 & g_1 & -g_2 \\ g_2 & -g_2 & g_1 \end{pmatrix}, \quad \mathbf{g}_3 = \begin{pmatrix} g_1 & g_2 & -g_2 \\ g_2 & g_1 & -g_2 \\ -g_2 & -g_2 & g_1 \end{pmatrix}, \tag{A7}$$

where

$$g_1 = \tfrac{2}{3}g_{xy} + \tfrac{1}{3}g_z, \quad g_2 = -\tfrac{1}{3}g_{xy} + \tfrac{1}{3}g_z. \tag{A8}$$

APPENDIX B: LINEAR SPIN-WAVE THEORY FOR A GENERAL 4-SUBLATTICE GROUND STATE

A general framework for linear spin-wave theory on the pyrochlore lattice is set out in [44], following the pattern that can be found in [148]. For completeness here we reproduce the technical steps needed to apply such a theory to the 4-sublattice, $\mathbf{q} = 0$ classical ground states discussed in Sec. III.

As with the classical spin-wave theory developed in Sec. IV A, it is convenient to work in a local basis, in which spins are quantized such that their local z axis is aligned with the classical ground state. Following Eq. (68), we label these local axes

$$\{\mathbf{u}_i,\mathbf{v}_i,\mathbf{w}_i\}$$

and quantize fluctuations about the classical ground state by introducing Holstein-Primakoff bosons

$$S_i^w = S - a_i^\dagger a_i, \tag{B1}$$

$$S_i^+ = S_i^u + iS_i^v = (2S - a_i^\dagger a_i)^{1/2} a_i \approx \sqrt{2S} a_i, \tag{B2}$$

$$S_i^- = S_i^u - iS_i^v = a_i^\dagger (2S - a_i^\dagger a_i)^{1/2} \approx \sqrt{2S} a_i^\dagger, \tag{B3}$$

where $[a_i, a_j^\dagger] = \delta_{ij}$.

Substituting these expressions in $\mathcal{H}_{\mathsf{ex}}$ [Eq. (4)] and Fourier transforming them, we obtain

$$\mathcal{H}_{\mathsf{ex}} \approx \mathcal{E}_0 + \mathcal{H}_{\mathsf{ex}}^{\mathsf{LSW}} + \cdots, \tag{B4}$$

where $\mathcal{E}_0$ is the classical ground-state energy defined in Eq. (70), and

$$\mathcal{H}_{\mathsf{ex}}^{\mathsf{LSW}} = \frac{1}{2}\sum_{\mathbf{q}} \tilde{A}^\dagger(\mathbf{q}) \cdot \mathbf{X}(\mathbf{q}) \cdot \tilde{A}(\mathbf{q}) \tag{B5}$$

describes quantum fluctuations at the level of linear spin-wave theory. Here $\tilde{A}^\dagger(\mathbf{q}),\tilde{A}(\mathbf{q})$ are eight-component vectors of operators

$$\tilde{A}^\dagger(\mathbf{q}) = [a_0^\dagger(\mathbf{q}),a_1^\dagger(\mathbf{q}),a_2^\dagger(\mathbf{q}),a_3^\dagger(\mathbf{q}),$$
$$a_0(-\mathbf{q}),a_1(-\mathbf{q}),a_2(-\mathbf{q}),a_3(-\mathbf{q})] \tag{B6}$$

and $X(\mathbf{q})$ is an 8×8 matrix written in block form as

$$\mathbf{X}(\mathbf{q}) = 2S\begin{pmatrix} \mathbf{X}^{11}(\mathbf{q}) & \mathbf{X}^{12}(\mathbf{q}) \\ \mathbf{X}^{21}(\mathbf{q}) & \mathbf{X}^{22}(\mathbf{q}) \end{pmatrix}, \tag{B7}$$

$$\mathbf{X}_{ij}^{11}(\mathbf{q}) = \cos(\mathbf{q}\cdot\mathbf{r}_{ij})\left(\mathbf{c}_i \cdot \mathbf{J}^{ij} \cdot \mathbf{c}_j^* - \delta_{ij}\sum_l \mathbf{w}_l \cdot \mathbf{J}^{lj} \cdot \mathbf{w}_j\right), \tag{B8}$$

$$\mathbf{X}_{ij}^{12}(\mathbf{q}) = \mathbf{X}_{ji}^{21*} = \cos(\mathbf{q}\cdot\mathbf{r}_{ij})(\mathbf{c}_i \cdot \mathbf{J}^{ij} \cdot \mathbf{c}_j), \tag{B9}$$

$$\mathbf{X}_{ij}^{22}(\mathbf{q}) = \cos(\mathbf{q}\cdot\mathbf{r}_{ij})\left(\mathbf{c}_i^* \cdot \mathbf{J}^{ij} \cdot \mathbf{c}_j - \delta_{ij}\sum_l \mathbf{w}_l \cdot \mathbf{J}^{lj} \cdot \mathbf{w}_j\right), \tag{B10}$$

where

$$\mathbf{c}_i = \frac{1}{\sqrt{2}}(\mathbf{u}_i + i\mathbf{v}_i). \tag{B11}$$

The spin-wave Hamiltonian $\mathcal{H}_{\rm ex}^{\rm LSW}$ [Eq. (B5)] can be diagonalized by a suitable Bogoliubov transformation. We accomplish this following the method outlined in Ref. [149] by introducing new Bose operators $[b_i, b_j^\dagger] = \delta_{ij}$, such that

$$\begin{aligned} B^\dagger(\mathbf{q}) &= [b_0^\dagger(\mathbf{q}), b_1^\dagger(\mathbf{q}), b_2^\dagger(\mathbf{q}), b_3^\dagger(\mathbf{q}), \\ &\quad b_0(-\mathbf{q}), b_1(-\mathbf{q}), b_2(-\mathbf{q}), b_3(-\mathbf{q})] \\ &= \tilde{A}^\dagger(\mathbf{q}) \cdot \mathbf{U}^\dagger(\mathbf{q}). \end{aligned} \tag{B12}$$

The condition that these operators are Bosonic may be written as

$$[B_i(\mathbf{q}), B_j^\dagger(\mathbf{q}')] = \sigma_{ij}\delta_{\mathbf{q}\mathbf{q}'}, \tag{B13}$$

where

$$\hat{\sigma} = \begin{pmatrix} \mathbf{1} & \mathbf{0} \\ \mathbf{0} & -\mathbf{1} \end{pmatrix} \tag{B14}$$

is an 8×8 matrix (written in block form) and leads to a pseudo-unitary condition on $\mathbf{U}(\mathbf{q})$:

$$\mathbf{U}^{-1}(\mathbf{q}) = \hat{\sigma} \cdot \mathbf{U}^\dagger(\mathbf{q}) \cdot \hat{\sigma}. \tag{B15}$$

Substituting in Eq. (B5), we obtain

$$\begin{aligned} \mathcal{H}_{\rm ex}^{\rm LSW} &= \frac{1}{2}\sum_{\mathbf{q}} B^\dagger(\mathbf{q}) \cdot \mathbf{U}^{-1\dagger}(\mathbf{q}) \cdot \mathbf{X}(\mathbf{q}) \cdot \mathbf{U}^{-1}(\mathbf{q}) \cdot B\ (\mathbf{q}) \\ &= \frac{1}{2}\sum_{\mathbf{q}} B^\dagger(\mathbf{q}) \cdot \hat{\sigma} \cdot \mathbf{U}(\mathbf{q}) \cdot \hat{\sigma} \cdot \mathbf{X}(\mathbf{q}) \cdot \mathbf{U}^{-1}(\mathbf{q}) \cdot B\ (\mathbf{q}). \end{aligned} \tag{B16}$$

The object $\mathbf{U}(\mathbf{q}) \cdot \hat{\sigma} \cdot \mathbf{X}(\mathbf{q}) \cdot \mathbf{U}^{-1}(\mathbf{q})$ is a similarity transformation on the matrix $\hat{\sigma} \cdot \mathbf{X}(\mathbf{q})$, and for correctly chosen $\mathbf{U}(\mathbf{q})$, will be a diagonal matrix containing the eigenvalues of $\hat{\sigma} \cdot \mathbf{X}(\mathbf{q})$. We then arrive at

$$\mathcal{H}_{\rm ex}^{\rm LSW} = \frac{1}{2}\sum_{\mathbf{q}} B^\dagger(\mathbf{q}) \cdot \hat{\sigma} \cdot \begin{pmatrix} \omega_\nu(\mathbf{q}) & 0 \\ 0 & -\omega_\nu(\mathbf{q}) \end{pmatrix} \cdot B\ (\mathbf{q}). \tag{B17}$$

Collecting all terms, reordering operators, and inserting into Eq. (B4) we obtain the result quoted in Sec. IV C,

$$\begin{aligned} \mathcal{H}_{\rm ex} &\approx \mathcal{E}_0\left(1 + \frac{1}{S}\right) + \sum_{\mathbf{q}}\sum_{\nu=0}^{3} \omega_\nu(\mathbf{q}) \\ &\quad \times \left(b_\nu^\dagger(\mathbf{q}) b_\nu(\mathbf{q}) + \frac{1}{2}\right) + \cdots. \end{aligned} \tag{B18}$$

The dispersion $\omega_\nu(\mathbf{q})$ of the four branches of spin waves can be found by numerical diagonalization of $\hat{\sigma} \cdot \tilde{X}(\mathbf{q})$.

APPENDIX C: CLASSICAL MONTE CARLO SIMULATION

The Monte Carlo simulations described in this paper are based on the Metropolis algorithm with parallel tempering [150,151] and over-relaxation [152]. The spins are modeled as classical vectors of length $|S_i| = 1/2$ and locally updated using the standard Marsaglia method [153]. We consider cubic clusters of linear dimension L, based on the 16-site cubic unit cell of the pyrochlore lattice, and containing $N = 16L^3$ sites. A Monte Carlo step (MCs) is defined as N attempts to locally update a randomly chosen spin, and $t_{\rm max}$ (measured in MCs) is the total Monte Carlo time over which data are collected.

Equilibration is performed for each temperature in two successive steps. First the system is slowly cooled down from high temperature (random initial spin configuration) to the temperature of measurement T during $t_{\rm max}/10$ MCs. Then, the system is equilibrated at temperature T during additional $t_{\rm max}/10$ MCs. After equilibration, Monte Carlo time is set to zero and measurements start and go on for $t_{\rm max} \sim 10^5$–10^7 MCs.

All thermodynamical observables have been averaged over Monte Carlo time every 10 MCs, except for calculations of the equal-time structure factor $S(\mathbf{q})$, where data points were taken every 100 MCs for efficiency. The parallel tempering method implies simultaneously simulating a large number of replicas of the system in parallel, with each replica held at a different temperature. The program then regularly attempts to swap the spin configurations of replicas with neighboring temperatures, in such a way as to maintain detailed balance [150,151]. Simulating ∼120 replicas, with swaps attempted every 100 MCs appears to offer a good compromise between efficiency and decorrelation for $L = 6$.

In the case of the over-relaxation method, after each Monte Carlo step, two further sweeps are made of the entire lattice. Each spin feels an effective field due to the interaction with its six nearest neighbors; any rotation around this axis conserves the energy and is thus an acceptable move respecting detailed balance. To avoid rotating successive neighboring spins, we first update all spins of sublattice 0, then sublattice 1, 2, and finally 3. The first iteration of all N spins is deterministic, i.e., we rotate them by the maximum allowed angle; while for the second iteration, a random angle of rotation is chosen for each spin. The generation of so many random numbers is of course time consuming but is recommended for better equilibration [154]. We note that convergence of the specific heat $c_h \to 1$ for $T \to 0$ is a good indication of the equilibration of ordered phases at low temperatures.

The main results of Monte Carlo simulations are summarized in the finite-temperature phase diagram Fig. 3, which spans all four of the ordered phases discussed in the article. This phase diagram was determined from simulations for 64 different parameter sets, equally spaced on the circle defined by $\sqrt{J_1^2 + J_2^2} = 3\,|J_3|$ illustrated by the white circle in Fig. 1, with $J_3 = -0.1$ meV and $J_4 = 0$. Transition temperatures for each phase were extracted from the relevant order-parameter susceptibilities, as described in Sec. V.

Simulations were performed for a cluster of $N = 3456$ spins ($L = 6$), and data averaged over ten independent runs during $t_{\rm max} = 10^6$ MCs. Parallel tempering was used, typically with 121 replicas, at temperatures equally spaced from 0 to 1.2 K. However, close to the boundaries between phases with different symmetries, the large number of competing ground states makes simulations difficult to equilibrate. Here additional data points with better statistics were sometimes necessary, typically with 201 temperatures on a smaller temperature window, with $t_{\rm max} = 10^7$ MCs and $N = 8192$ (i.e., $L = 8$).

[1] L. Balents, Spin liquids in frustrated magnets, Nature (London) **464**, 199 (2010).

[2] C. Castelnovo, R. Moessner, and S. L. Sondhi, Spin ice, fractionalization, and topological order, Annu. Rev. Condens. Matter Phys. **3**, 35 (2012).

[3] M. Hermele, M. P. A. Fisher, and L. Balents, Pyrochlore photons: The $U(1)$ spin liquid in a $S = 1/2$ three-dimensional frustrated magnet, Phys. Rev. B **69**, 064404 (2004).

[4] A. Banerjee, S. V. Isakov, K. Damle, and Y.-B. Kim, Unusual Liquid State of Hard-Core Bosons on the Pyrochlore Lattice, Phys. Rev. Lett. **100**, 047208 (2008).

[5] L. Savary and L. Balents, Coulombic Quantum Liquids in Spin-1/2 Pyrochlores, Phys. Rev. Lett. **108**, 037202 (2012).

[6] N. Shannon, O. Sikora, F. Pollmann, K. Penc, and P. Fulde, Quantum Ice: A Quantum Monte Carlo Study, Phys. Rev. Lett. **108**, 067204 (2012).

[7] O. Benton, O. Sikora, and N. Shannon, Seeing the light: Experimental signatures of emergent electromagnetism in a quantum spin ice, Phys. Rev. B **86**, 075154 (2012).

[8] S.-B. Lee, S. Onoda, and L. Balents, Generic quantum spin ice, Phys. Rev. B **86**, 104412 (2012).

[9] L. Savary and L. Balents, Spin liquid regimes at nonzero temperature in quantum spin ice, Phys. Rev. B **87**, 205130 (2013).

[10] M. J. P. Gingras and P. A. McClarty, Quantum spin ice: A search for gapless quantum spin liquids in pyrochlore magnets, Rep. Prog. Phys. **77**, 056501 (2014).

[11] Z. Hao, A. G. R. Day, and M. J. P. Gingras, Bosonic many-body theory of quantum spin ice, Phys. Rev. B **90**, 214430 (2014).

[12] L. D. Pan, S. K. Kim, A. Ghosh, C. M. Morris, K. A. Ross, E. Kermarrec, B. D. Gaulin, S. M. Koohpayeh, O. Tchernyshyov, and N. P. Armitage, Low-energy electrodynamics of novel spin excitations in the quantum spin ice $Yb_2Ti_2O_7$, Nat. Commun. **5**, 4970 (2014).

[13] L. D. Pan, N. J. Laurita, K. A. Ross, B. D. Gaulin, and N. P. Armitage, A measure of monopole inertia in the quantum spin ice $Yb_2Ti_2O_7$, Nat. Phys. **12**, 361 (2016).

[14] Y. Tokiwa, T. Yamashita, M. Udagawa, S. Kittaka, T. Sakakibara, D. Terazawa, Y. Shimoyama, T. Terashima, Y. Yasui, T. Shibauchi, and Y. Matsuda, Possible observation of highly itinerant quantum magnetic monopoles in the frustrated pyrochlore $Yb_2Ti_2O_7$, Nat. Commun. **7**, 10807 (2016).

[15] M. J. Harris, S. T. Bramwell, D. F. McMorrow, T. Zeiske, and K. W. Godfrey, Geometrical Frustration in the Ferromagnetic Pyrochlore $Ho_2Ti_2O_7$, Phys. Rev. Lett. **79**, 2554 (1997).

[16] R. Moessner, Relief and generation of frustration in pyrochlore magnets by single-ion anisotropy, Phys. Rev. B **57**, R5587(R) (1998).

[17] J. S. Gardner, M. J. P. Gingras, and J. E. Greedan, Magnetic pyrochlore oxides, Rev. Mod. Phys. **82**, 53 (2010).

[18] H. W. J. Blöte, R. F. Wielinga, and W. J. Huiskamp, Heat capacity measurements on rare-earth double oxides $R_2M_2O_7$, Physica **43**, 549 (1969).

[19] G. W. Chern, Novel Magnetic Orders and ice phases in frustrated Kondo–lattice models, Spin **5**, 1540006 (2015).

[20] P. Bonville, J. A. Hodges, E. Bertin, J.-P. Bouchaud, P. Dalmas de Reotier, L.-P. Regnault, H. M. Ronnow, J.-P. Sanchez, S. Sosin, and A. Yaouanc, Transitions and spin dynamics at very low temperature in the pyrochlores $Yb_2Ti_2O_7$ and $Gd_2Sn_2O_7$, Hyperfine Interact. **156/157**, 103 (2004).

[21] K. A. Ross, J. P. C. Ruff, C. P. Adams, J. S. Gardner, H. A. Dabkowska, Y. Qiu, J. R. D. Copley, and B. D. Gaulin, Two-Dimensional Kagome Correlations and Field Induced Order in the Ferromagnetic XY Pyrochlore $Yb_2Ti_2O_7$, Phys. Rev. Lett. **103**, 227202 (2009).

[22] K. A. Ross, L. R. Yaraskavitch, M. Laver, J. S. Gardner, J. A. Quilliam, S. Meng, J. B. Kycia, D. K. Singh, T. Proffen, H. A. Dabkowska, and B. D. Gaulin, Dimensional evolution of spin correlations in the magnetic pyrochlore $Yb_2Ti_2O_7$, Phys. Rev. B **84**, 174442 (2011).

[23] J. D. Thompson, P. A. McClarty, H. M. Ronnow, L. P. Regnault, A. Sorge, and M. J. P. Gingras, Rods of Neutron Scattering Intensity in $Yb_2Ti_2O_7$: Compelling Evidence for Significant Anisotropic Exchange in a Magnetic Pyrochlore Oxide, Phys. Rev. Lett. **106**, 187202 (2011).

[24] L.-J. Chang, S. Onoda, Y. Su, Y.-J. Kao, K.-D. Tsuei, Y. Yasui, K. Kakurai, and M. R. Lees, Higgs transition from a magnetic Coulomb liquid to a ferromagnet in $Yb_2Ti_2O_7$, Nat. Commun. **3**, 992 (2012).

[25] J. D. M. Champion, M. J. Harris, P. C. W. Holdsworth, A. S. Wills, G. Balakrishnan, S. T. Bramwell, E. Cizmar, T. Fennell, J. S. Gardner, J. Lago, D. F. McMorrow, M. Orendac, A. Orendacova, D. McK. Paul, R. I. Smith, M. T. F. Telling, and A. Wildes, $Er_2Ti_2O_7$: Evidence of quantum order by disorder in a frustrated antiferromagnet, Phys. Rev. B **68**, 020401(R) (2003).

[26] L. Savary, K. A. Ross, B. D. Gaulin, J. P. C. Ruff, and L. Balents, Order by Quantum Disorder in $Er_2Ti_2O_7$, Phys. Rev. Lett. **109**, 167201 (2012).

[27] M. E. Zhitomirsky, M. V. Gvozdikova, P. C. W. Holdsworth, and R. Moessner, Quantum Order by Disorder and Accidental Soft Mode in $Er_2Ti_2O_7$, Phys. Rev. Lett. **109**, 077204 (2012).

[28] J. Oitmaa, R. R. P. Singh, B. Javanparast, A. G. R. Day, B. V. Bagheri, and M. J. P. Gingras, Phase transition and thermal order-by-disorder in the pyrochlore antiferromagnet $Er_2Ti_2O_7$: A high-temperature series expansion study, Phys. Rev. B **88**, 220404(R) (2013).

[29] J. G. Rau, S. Petit, and M. J. P. Gingras, Order by virtual crystal field fluctuations in pyrochlore XY antiferromagnets, Phys. Rev. B **93**, 184408 (2016).

[30] K. Matsuhira, Y. Hinatsu, K. Tenya, H. Amitsuka, and T. Sakakibara, Low-temperature magnetic properties of pyrochlore stannates, J. Phys. Soc. Jpn. **71**, 1576 (2002).

[31] J. Lago, T. Lancaster, S. J. Blundell, S. T. Bramwell, F. L. Pratt, M. Shirai, and C. Baines, Magnetic ordering and dynamics in the XY pyrochlore antiferromagnet: A muon-spin relaxation study of $Er_2Ti_2O_7$ and $Er_2Sn_2O_7$, J. Phys.: Condens. Matter **17**, 979 (2005).

[32] M. Shirai, Experimental investigations of frustrated magnets, Ph.D. Thesis, University of London, 2007.

[33] P. M. Sarte, H. J. Silverstein, B. T. K. van Wyk, J. S. Gardner, Y. Qiu, H. D. Zhou, and C. R. Wiebe, Absence of long-range magnetic ordering in the pyrochlore compound $Er_2Sn_2O_7$, J. Phys.: Condens. Matter **23**, 382201 (2011).

[34] S. Guitteny, S. Petit, E. Lhotel, J. Robert, P. Bonville, A. Forget, and I. Mirebeau, Palmer-Chalker correlations in the XY pyrochlore antiferromagnet $Er_2Sn_2O_7$, Phys. Rev. B **88**, 134408 (2013).

[35] Z. L. Dun, E. S. Choi, H. D. Zhou, A. M. Hallas, H. J. Silverstein, Y. Qiu, J. R. D. Copley, J. S. Gardner, and C. R.

Wiebe, $Yb_2Sn_2O_7$: A magnetic Coulomb liquid at a quantum critical point, Phys. Rev. B **87**, 134408 (2013).

[36] A. Yaouanc, P. Dalmas de Réotier, P. Bonville, J. A. Hodges, V. Glazkov, L. Keller, V. Sikolenko, M. Bartkowiak, A. Amato, C. Baines, P. J. C. King, P. C. M. Gubbens, and A. Forget, Dynamical Splayed Ferromagnetic Ground State in the Quantum Spin Ice $Yb_2Sn_2O_7$, Phys. Rev. Lett. **110**, 127207 (2013).

[37] X. Li, W. M. Li, K. Matsubayashi, Y. Sato, C. Q. Jin, Y. Uwatoko, T. Kawae, A. M. Hallas, C. R. Wiebe, A. M. Arevalo-Lopez, J. P. Attfield, J. S. Gardner, R. S. Freitas, H. D. Zhou, and J.-G. Cheng, Long-range antiferromagnetic order in the frustrated XY pyrochlore antiferromagnet $Er_2Ge_2O_7$, Phys. Rev. B **89**, 064409 (2014).

[38] Z. L. Dun, X. Li, R. S. Freitas, E. Arrighi, C. R. Dela Cruz, M. Lee, E. S. Choi, H. B. Cao, H. J. Silverstein, C. R. Wiebe, J. G. Cheng, and H. D. Zhou, Antiferromagnetic order in the pyrochlores $R_2Ge_2O_7$ (R = Er, Yb), Phys. Rev. B **92**, 140407(R) (2015).

[39] Y. Q. Cai, Q. Ciu, X. Li, Z. L. Dun, J. Ma, C. dela Cruz, Y. Y. Jiao, J. Liao, P. J. Sun, Y. Q. Li, J. S. Zhou, J. B. Goodenough, H. D. Zhou, and J.-G. Cheng, High-pressure synthesis and characterization of the effective pseudospin $S = 1/2$ XY pyrochlores $R_2Pt_2O_7$ (R = Er, Yb), Phys. Rev. B **93**, 014443 (2016).

[40] R. Sibille, E. Lhotel, V. Pomjakushkin, C. Baines, T. Fennell, and M. Kenzelmann, Candidate Quantum Spin Liquid in the Ce^{3+} Pyrochlore Stannate $Ce_2Sn_2O_7$, Phys. Rev. Lett. **115**, 097202 (2015).

[41] H. Yan, O. Benton, L. D. C. Jaubert, and N. Shannon, Living on the edge: Ground-state selection in quantum spin-ice pyrochlores, arXiv:1311.3501.

[42] S. H. Curnoe, Quantum spin configurations in $Tb_2Ti_2O_7$, Phys. Rev. B **75**, 212404 (2007); **76**, 139903(E) (2007).

[43] P. A. McClarty, S. H. Curnoe, and M. J. P. Gingras, Energetic selection of ordered states in a model of the $Er_2Ti_2O_7$ frustrated pyrochlore XY antiferromagnet, J. Phys.: Conf. Ser. **145**, 012032 (2009).

[44] K. A. Ross, L. Savary, B. D. Gaulin, and L. Balents, Quantum Excitations in Quantum Spin Ice, Phys. Rev. X **1**, 021002 (2011).

[45] R. Moessner and J. T. Chalker, Low-temperature properties of classical geometrically frustrated antiferromagnets, Phys. Rev. B **58**, 12049 (1998).

[46] A. W. C. Wong, Z. Hao, and M. J. P. Gingras, Ground state phase diagram of generic XY pyrochlore magnets with quantum fluctuations, Phys. Rev. B **88**, 144402 (2013).

[47] S. E. Palmer and J. T. Chalker, Order induced by dipolar interactions in a geometrically frustrated antiferromagnet, Phys. Rev. B **62**, 488 (2000).

[48] O. Benton, L. D. C. Jaubert, H. Yan, and N. Shannon, A spin-liquid with pinch-line singularities on the pyrochlore lattice, Nat. Commun. **7**, 11572 (2016).

[49] O. Benton, Classical and quantum spin liquids on the pyrochlore lattice, Ph.D. Thesis, University of Bristol, 2014.

[50] H. Cao, A. Gukasov, I. Mirebeau, P. Bonville, C. Decorse, and G. Dhalenne, Ising versus XY Anisotropy in Frustrated $R_2Ti_2O_7$ Compounds as "Seen" by Polarized Neutrons, Phys. Rev. Lett. **103**, 056402 (2009).

[51] J. G. Rau and M. J. P. Gingras, Magnitude of quantum effects in classical spin ices, Phys. Rev. B **92**, 144417 (2015).

[52] S. Onoda and Y. Tanaka, Quantum fluctuations in the effective pseudospin-1/2 model for magnetic pyrochlore oxides, Phys. Rev. B **83**, 094411 (2011).

[53] Y.-P. Huang, G. Chen, and M. Hermele, Quantum Spin Ices and Topological Phases from Dipolar-Octupolar Doublets on the Pyrochlore Lattice, Phys. Rev. Lett. **112**, 167203 (2014).

[54] Y.-D. Li and G. Chen, Symmetry enriched $U(1)$ topological orders for dipole-octupole doublets on a pyrochlore lattice, Phys. Rev. B **95**, 041106(R) (2017).

[55] H. R. Molavian, M. J. P. Gingras, and B. Canals, Dynamically Induced Frustration as a Route to a Quantum Spin Ice State in $Tb_2Ti_2O_7$ via Virtual Crystal Field Excitations and Quantum Many-Body Effects, Phys. Rev. Lett. **98**, 157204 (2007).

[56] R. Applegate, N. R. Hayre, R. R. P. Singh, T. Lin, A. G. R. Day, and M. J. P. Gingras, Vindication of $Yb_2Ti_2O_7$ as a Model Exchange Quantum Spin Ice, Phys. Rev. Lett. **109**, 097205 (2012).

[57] N. R. Hayre, K. A. Ross, R. Applegate, T. Lin, R. R. P. Singh, B. D. Gaulin, and M. J. P. Gingras, Thermodynamic properties of $Yb_2Ti_2O_7$ pyrochlore as a function of temperature and magnetic field: Validation of a quantum spin ice exchange Hamiltonian, Phys. Rev. B **87**, 184423 (2013).

[58] P. Bonville, S. Petit, I. Mirebeau, J. Robert, E. Lhotel, and C. Paulsen, Magnetization process in $Er_2Ti_2O_7$ at very low temperature, J. Phys.: Condens. Matter **25**, 275601 (2013).

[59] J. G. Rau, L. S. Wu, A. F. May, L. Poudel, B. Winn, V. O. Garlea, A. Huq, P. Whitfield, A. E. Taylor, M. D. Lumsden, M. J. P. Gingras, and A. D. Christianson, Anisotropic Exchange within Decoupled Tetrahedra in the Quantum Breathing Pyrochlore $Ba_3Yb_2Zn_5O_{11}$, Phys. Rev. Lett. **116**, 257204 (2016).

[60] In contrast, it has recently been found that Dzyaloshinskii-Moriya interactions in the "breathing-pyrochlore" material $Ba_3Yb_2Zn_5O_{11}$ are rather large [59,61].

[61] T. Haku, K. Kimura, Y. Matsumoto, M. Soda, M. Sera, D. Yu, R. A. Mole, T. Takeuchi, S. Nakatsuji, Y. Kono, T. Sakakibara, L. J. Chang, and T. Masuda, Low-energy excitations and ground-state selection in the quantum breathing pyrochlore antiferromagnet $Ba_3Yb_2Zn_5O_{11}$, Phys. Rev. B **93**, 220407(R) (2016).

[62] L. Pauling, The structure and entropy of ice and of other crystals with some randomness of atomic arrangement, J. Am. Chem. Soc. **57**, 2680 (1935).

[63] O. V. Kovalev, *Representations of the Crystallographic Space Groups*, 2nd ed. (Gordon and Breach, Switzerland, 1993).

[64] M. S. Dresselhaus, G. Dresselhaus, and A. Jorio, *Group Theory: Application to the Physics of Condensed Matter* (Springer, Berlin, 2010).

[65] A. Poole, A. S. Wills, and E. Lelièvre-Berna, Magnetic ordering in the XY pyrochlore antiferromagnet $Er_2Ti_2O_7$: A spherical neutron polarimetry study, J. Phys.: Condens. Matter **19**, 452201 (2007).

[66] Y. Yasui, M. Soda, S. Iikubo, M. Ito, M. Sato, N. Hamaguchi, T. Matsuhshita, N. Wada, T. Takeuchi, N. Aso, and K. Kakurai, Ferromagnetic transition of pyrochlore compound $Yb_2Ti_2O_7$, J. Phys. Soc. Jpn. **72**, 3014 (2003).

[67] The first line of Eq. (24) is a quadratic invariant of T_d, while the next three form a basis for the T_1 irreducible representation.

[68] L.-J. Chang, M. R. Lees, I. Watanabe, A. D. Hillier, Y. Yasui, and S. Onoda, Static magnetic moments revealed by muon spin relaxation and thermodynamic measurements in the quantum spin ice $Yb_2Ti_2O_7$, Phys. Rev. B **89**, 184416 (2014).

[69] E. Lhotel, S. R. Giblin, M. R. Lees, G. Balakrishnan, L.-J. Chang, and Y. Yasui, First-order magnetic transition in $Yb_2Ti_2O_7$, Phys. Rev. B **89**, 224419 (2014).

[70] L. D. C. Jaubert, O. Benton, J. G. Rau, J. Oitmaa, R. R. P. Singh, N. Shannon, and M. J. P. Gingras, Are Multiphase Competition and Order by Disorder the Keys to Understanding $Yb_2Ti_2O_7$? Phys. Rev. Lett. **115**, 267208 (2015).

[71] J. Gaudet, K. A. Ross, E. Kermarrec, N. P. Butch, G. Ehlers, H. A. Dabkowska, and B. D. Gaulin, Gapless quantum excitations from an ice-like splayed ferromagnetic ground state in stoichiometric $Yb_2Ti_2O_7$, Phys. Rev. B **93**, 064406 (2016).

[72] A. M. Hallas, J. Gaudet, N. P. Butch, M. Tachibana, R. S. Freitas, G. M. Luke, C. R. Wiebe, and B. D. Gaulin, Universal dynamic magnetism in Yb-pyrochlores with disparate ground states, Phys. Rev. B **93**, 100403(R) (2016).

[73] J. Robert, E. Lhotel, G. Remenyi, S. Sahling, I. Mirebeau, C. Decorse, B. Canals, and S. Petit, Spin dynamics in the presence of competing ferromagnetic and antiferromagnetic correlations in $Yb_2Ti_2O_7$, Phys. Rev. B **92**, 064425 (2015).

[74] A. Yaouanc, P. Dalmas de Réotier, L. Keller, B. Roessli, and A. Forget, A novel type of splayed ferromagnetic order observed in $Yb_2Ti_2O_7$, J. Phys.: Condens. Matter **28**, 426002 (2016).

[75] I. Mirebeau, A. Apetrei, J. Rodriguez-Carvajal, P. Bonville, A. Forget, D. Colson, V. Glazkov, J. P. Sanches, O. Isnard, and E. Suard, Ordered Spin Ice State and Magnetic Fluctuations in $Tb_2Sn_2O_7$, Phys. Rev. Lett. **94**, 246402 (2005).

[76] S. Petit, P. Bonville, I. Mirebeau, H. Mutka, and J. Robert, Spin dynamics in the ordered spin ice $Tb_2Sn_2O_7$, Phys. Rev. B **85**, 054428 (2012).

[77] M. E. Zhitomirsky, P. C. W. Holdsworth, and R. Moessner, Nature of finite-temperature transition in anisotropic pyrochlore $Er_2Ti_2O_7$, Phys. Rev. B **89**, 140403(R) (2014).

[78] V. S. Maryasin and M. E. Zhitomirsky, Order from structural disorder in the XY pyrochlore antiferromagnet $Er_2Ti_2O_7$, Phys. Rev. B **90**, 094412 (2014).

[79] A. Andreanov and P. A. McClarty, Order induced by dilution in pyrochlore XY antiferromagnets, Phys. Rev. B **91**, 064401 (2015).

[80] G.-W. Chern, Pyrochlore antiferromagnet with antisymmetric exchange interactions: Critical behavior and order from disorder, arXiv:1008.3038.

[81] B. Javanparast, A. G. R. Day, Z. Hao, and M. J. P. Gingras, Order-by-disorder near criticality in XY pyrochlore magnets, Phys. Rev. B **91**, 174424 (2015).

[82] P. A. McClarty, P. Stasiak, and M. J. P. Gingras, Order-by-disorder in the XY pyrochlore antiferromagnet, Phys. Rev. B **89**, 024425 (2014).

[83] B. Canals, M. Elhajal, and C. Lacroix, Ising-like order by disorder in the pyrochlore antiferromagnet with Dzyaloshinskii-Moriya interactions, Phys. Rev. B **78**, 214431 (2008).

[84] E. Lhotel, S. Petit, S. Guitteny, O. Florea, M. Ciomaga Hatnean, C. Colin, E. Ressouche, M. R. Lees, and G. Balakrishnan, Fluctuations and All-In-All-Out Ordering in Dipole-Octupole $Nd_2Zr_2O_7$, Phys. Rev. Lett. **115**, 197202 (2015).

[85] L. Seabra, P. Sindzingre, T. Momoi, and N. Shannon, Novel phases in a square-lattice frustrated ferromagnet: Magnetization plateau, helicoidal spin liquid, and vortex crystal, Phys. Rev. B **93**, 085132 (2016).

[86] N. Shannon, K. Penc, and Y. Motome, Nematic, vector-multipole, and plateau-liquid states in the classical O(3) pyrochlore antiferromagnet with biquadratic interactions in applied magnetic field, Phys. Rev. B **81**, 184409 (2010).

[87] J. D. M. Champion and P. C. W. Holdsworth, Soft modes in the easy plane pyrochlore antiferromagnet, J. Phys.: Condens. Matter **16**, S665 (2004).

[88] P. Chandra and B. Doucot, Possible spin liquid state at large S for the frustrated square Heisenberg lattice, Phys. Rev. B **38**, 9335 (1988).

[89] H. J. Schulz, T. A. L. Ziman, and D. Poilblanc, Magnetic order and disorder in the frustrated quantum Heisenberg antiferromagnet in two dimensions, J. Phys. I France **6**, 675 (1996).

[90] N. Shannon, B. Schmidt, K. Penc, and P. Thalmeier, Finite temperature properties and frustrated ferromagnetism in a square lattice Heisenberg model, Eur. Phys. J B **38**, 599 (2004).

[91] N. Shannon, T. Momoi, and P. Sindzingre, Nematic Order in Square Lattice Frustrated Ferromagnets, Phys. Rev. Lett. **96**, 027213 (2006).

[92] T. Fennell, P. P. Deen, A. R. Wildes, K. Schmalzl, D. Prabhakaran, A. T. Boothroyd, R. J. Aldus, D. F. McMorrow, and S. T. Bramwell, Magnetic Coulomb phase in the spin ice $Ho_2Ti_2O_7$, Science **326**, 411 (2009).

[93] J. A. Hodges, P. Bonville, A. Forget, M. Rams, K. Krolas, and G. Dhalenne, The crystal field and exchange interactions in $Yb_2Ti_2O_7$, J. Phys.: Condens. Matter **13**, 9301 (2001).

[94] P. Dalmas de Réotier, A. Yaouanc, Y. Chapuis, S. H. Curnoe, B. Grenier, E. Ressouche, C. Marin, J. Lago, C. Baines, and S. R. Giblin, Magnetic order, magnetic correlations, and spin dynamics in the pyrochlore antiferromagnet $Er_2Ti_2O_7$, Phys. Rev. B **86**, 104424 (2012).

[95] K. A. Ross, Y. Qiu, J. R. D. Copley, H. A. Dabkowska, and B. D. Gaulin, Order by Disorder Spin Wave Gap in the XY Pyrochlore Magnet $Er_2Ti_2O_7$, Phys. Rev. Lett. **112**, 057201 (2014).

[96] S. Petit, J. Robert, S. Guitteny, P. Bonville, C. Decorse, J. Ollivier, H. Mutka, M. J. P. Gingras, and I. Mirebeau, Order by disorder or energetic selection of the ground state in the XY pyrochlore antiferromagnet $Er_2Ti_2O_7$: An inelastic neutron scattering study, Phys. Rev. B **90**, 060410(R) (2014).

[97] J. A. Hodges, P. Bonville, A. Forget, A. Yaouanc, P. Dalmas de Réotier, G. André, M. Rams, K. Królas, C. Ritter, P. C. M. Gubbens, C. T. Kaiser, P. J. C. King, and C. Baines, First-Order Transition in the Spin Dynamics of Geometrically Frustrated $Yb_2Ti_2O_7$, Phys. Rev. Lett. **88**, 077204 (2002).

[98] S. Bhattacharjee, S. Erfanifam, E. L. Green, M. Naumann, Z. Wang, S. Granovsky, M. Doerr, J. Wosnitza, A. A. Zyvagin, R. Moessner, A. Maljuk, S. Wurmehl, B. Büchner, and S. Zherlitsyn, Acoustic signatures of the phases and phase transitions in $Yb_2Ti_2O_7$, Phys. Rev. B **93**, 144412 (2016).

[99] M. Taillefumier (unpublished).

[100] J. Alam, Y. M. Jana, and A. Ali Biswas, Magnetic ground-state of strongly frustrated pyrochlore anti-ferromagnet $Er_2Sn_2O_7$, J. Magn. Magn. Mater. **361**, 175 (2014).

[101] C. Wiebe and A. Hallas, Frustration under pressure: Exotic magnetism in new pyrochlore oxides, APL Mater. **3**, 041519 (2015).

[102] J. Lago, I. Zivkovic, J. O. Piatek, P. Alvarez, D. Hüvonen, F. L. Pratt, M. Diaz, and T. Rojo, Glassy dynamics in the low-temperature inhomogeneous ferromagnetic phase of the quantum spin ice $Yb_2Sn_2O_7$, Phys. Rev. B **89**, 024421 (2014).

[103] Z. L. Dun, M. Lee, E. S. Choi, A. M. Hallas, C. R. Wiebe, J. S. Gardner, E. Arrighi, R. S. Freitas, A. M. Arevalo-Lopez, J. P. Attfield, H. D. Zhou, and J. G. Cheng, Chemical pressure effects on magnetism in the quantum spin liquid candidates, $Yb_2X_2O_7$ (X = Sn, Ti, Ge), Phys. Rev. B **89**, 064401 (2014).

[104] A. M. Hallas, J. Gaudet, M. N. Wilson, T. J. Munsie, A. A. Aczel, M. B. Stone, R. S. Freitas, A. M. Arevalo-Lopez, J. P. Attfield, M. Tachibana, C. R. Wiebe, G. M. Luke, and B. D. Gaulin, XY antiferromagnetic ground state in the effective $S = 1/2$ pyrochlore $Yb_2Ge_2O_7$, Phys. Rev. B **93**, 104405 (2016).

[105] A. M. Hallas, A. Z. Sharma, Y. Cai, T. J. Munsie, M. N. Wilson, M. Tachibana, C. R. Wiebe, and G. M. Luke, Relief of frustration in the Heisenberg pyrochlore antiferromagnet $Gd_2Pt_2O_7$, Phys. Rev. B **94**, 134417 (2016).

[106] N. P. Raju, M. Dion, M. J. P. Gingras, T. E. Mason, and J. E. Greedan, Transition to long-range magnetic order in the highly frustrated insulating pyrochlore antiferromagnet $Gd_2Ti_2O_7$, Phys. Rev. B **59**, 14489 (1999).

[107] A. S. Wills, M. E. Zhitomirsky, B. Canals, J. P. Sanchez, P. Bonville, P. Dalmas de Réotier, and A. Yaouanc, Magnetic ordering in $Gd_2Sn_2O_7$: The archetypal Heisenberg pyrochlore antiferromagnet, J. Phys.: Condens. Matter **18**, L37 (2006).

[108] J. A. Quilliam, K. A. Ross, A. G. Del Maestro, M. J. P. Gingras, L. R. Corruccini, and J. B. Kycia, Evidence for Gapped Spin-Wave Excitations in the Frustrated $Gd_2Sn_2O_7$ Pyrochlore Antiferromagnet from Low-Temperature Specific Heat Measurements, Phys. Rev. Lett. **99**, 097201 (2007).

[109] J. D. M. Champion, A. S. Wills, T. Fennell, S. T. Bramwell, J. S. Gardner, and M. A. Green, Order in the Heisenberg pyrochlore: The magnetic structure of $Gd_2Ti_2O_7$, Phys. Rev. B **64**, 140407 (2001).

[110] P. Bonville, J. A. Hodges, M. Ocio, J. P. Sanchez, P. Vulliet, S. Sosin, and D. Brathwaite, Low temperature magnetic properties of geometrically frustrated $Gd_2Sn_2O_7$ and $Gd_2Ti_2O_7$, J. Phys.: Condens. Matter **15**, 7777 (2003).

[111] J. R. Stewart, G. Ehlers, A. S. Wills, S. T. Bramwell, and J. S. Gardner, Phase transitions, partial disorder and multi-k structures in $Gd_2Ti_2O_7$, J. Phys.: Condens. Matter **16**, L321 (2004).

[112] B. Javanparast, Z. Hao, M. Enjalran, and M. J. P. Gingras, Fluctuation-Driven Selection at Criticality in a Frustrated Magnetic System: The Case of Multiple-k Partial Order on the Pyrochlore Lattice, Phys. Rev. Lett. **114**, 130601 (2015).

[113] J. A. M. Paddison, A. B. Cairns, D. D. Khalyavin, P. Manuel, A. Daoud-Aladine, G. Ehlers, O. A. Petrenko, J. S. Gardner, H. D. Zhou, A. L. Goodwin, and J. R. Stewart, Nature of partial magnetic order in the frustrated antiferromagnet $Gd_2Ti_2O_7$, arXiv:1506.05045.

[114] A. M. Hallas, A. M. Arevalo-Lopez, A. Z. Sharma, T. Munsie, J. P. Attfield, C. R. Wiebe, and G. M. Luke, Magnetic frustration in lead pyrochlores, Phys. Rev. B **91**, 104417 (2015).

[115] M. Ciomaga-Hatnean, M. R. Lees, O. A. Petrenko, D. S. Keeble, and G. Balakrishnan, Structural and magnetic investigations of single-crystalline neodymium zirconate pyrochlore $Nd_2Zr_2O_7$, Phys. Rev. B **91**, 174416 (2015).

[116] A. Bertin, P. Dalmas de Réotier, B. Fåk, C. Marin, A. Yaouanc, A. Forget, D. Sheptyakov, B. Frick, C. Ritter, A. Amato, C. Baines, and P. J. C. King, $Nd_2Sn_2O_7$: An all-in-all-out pyrochlore magnet with no divergence-free field and anomalously slow paramagnetic spin dynamics, Phys. Rev. B **92**, 144423 (2015).

[117] J. Xu, V. K. Anand, A. K. Bera, M. Frontzek, D. L. Abernathy, N. Casati, K. Siemensmeyer, and B. Lake, Magnetic structure and crystal-field states of the pyrochlore antiferromagnet $Nd_2Zr_2O_7$, Phys. Rev. B **92**, 224430 (2015).

[118] M. E. Brooks-Bartlett, S. T. Banks, L. D. C. Jaubert, A. Harman-Clarke, and P. C. W. Holdsworth, Magnetic-Moment Fragmentation and Monopole Crystallization, Phys. Rev. X **4**, 011007 (2014).

[119] S. Petit, E. Lhotel, B. Canals, M. Ciomaga Hatnean, J. Ollivier, H. Muttka, E. Ressouche, A. R. Wildes, M. R. Lees, and G. Balakrishnan, Observation of magnetic fragmentation in spin ice, Nat. Phys. **12**, 746 (2016).

[120] O. Benton, Quantum origins of magnetic moment fragmentation in $Nd_2Zr_2O_7$, Phys. Rev. B **94**, 104430 (2016).

[121] S. H. Curnoe, Efffective spin-1/2 exchange model for $Tb_2Ti_2O_7$, Phys. Rev. B **88**, 014429 (2013).

[122] S. P. Mukherjee and S. H. Curnoe, Efffective spin-1/2 exchange interactions in $Tb_2Ti_2O_7$, Phys. Rev. B **90**, 214404 (2014).

[123] M. J. P. Gingras, B. C. den Hertog, M. Faucher, J. S. Gardner, S. R. Dunsiger, L. J. Chang, B. D. Gaulin, N. P. Raju, and J. E. Greedan, Thermodynamic and single-ion properties of Tb^{3+} within the collective paramagnetic-spin liquid state of the frustrated pyrochlore antiferromagnet $Tb_2Ti_2O_7$, Phys. Rev. B **62**, 6496 (2000).

[124] I. Mirebeau, P. Bonville, and M. Hennion, Magnetic excitations in $Tb_2Sn_2O_7$ and $Tb_2Ti_2O_7$ as measured by inelastic neutron scattering, Phys. Rev. B **76**, 184436 (2007).

[125] J. Zhang, K. Fritsch, Z. Hao, B. V. Bagheri, G. E. Granoth, P. Jiramongkolchai, R. J. Cava, and B. D. Gaulin, Neutron spectroscopic study of crystal field excitations $Tb_2Ti_2O_7$ and $Tb_2Sn_2O_7$, Phys. Rev. B **89**, 134410 (2014).

[126] P. A. McClarty, P. Stasiak, and M. J. P. Gingras, Soft dipolar spin ice physics and the ordered phase of the frustrated $Tb_2Sn_2O_7$ pyrochlore magnet, arXiv:1011.6346.

[127] J. S. Gardner, S. R. Dunsiger, B. D. Gaulin, M. J. P. Gingras, J. E. Greedan, R. F. Kiefl, M. D. Lumsden, W. A. MacFarlane, N. P. Raju, J. E. Sonier, I. Swainson, and Z. Tun, Cooperative Paramagnetism in the Geometrically Frustrated Pyrochlore Antiferromagnet $Tb_2Ti_2O_7$, Phys. Rev. Lett. **82**, 1012 (1999).

[128] J. S. Gardner, B. D. Gaulin, A. J. Berlinsky, P. Waldron, S. R. Dunsiger, N. P. Raju, and J. E. Greedan, Neutron scattering studies of the cooperative paramagnet pyrochlore $Tb_2Ti_2O_7$, Phys. Rev. B **64**, 224416 (2001).

[129] T. Fennell, M. Kenzelmann, B. Roessli, M. K. Haas, and R. J. Cava, Power-Law Correlations in the Pyrochlore Antiferromagnet, Phys. Rev. Lett. **109**, 017201 (2012).

[130] S. Petit, P. Bonville, J. Robert, C. Decorse, and I. Mirebeau, Spin liquid correlations anisotropic exchange and symmetry breaking $Tb_2Ti_2O_7$, Phys. Rev. B **86**, 174403 (2012).

[131] T. Taniguchi, H. Kadowaki, H. Takatsu, B. Fåk, J. Ollivier, T. Yamazaki, T. J. Sato, H. Yoshizawa, Y. Shimura, T. Sakakibara, K. Goto, L. R. Yaraskavitch, and J. B. Kycia, Long-range order and spin-liquid states in the frustrated pyrochlore $Tb_{2+x}Ti_{2-x}O_{7+y}$, Phys. Rev. B **87**, 060408 (2013).
[132] H. Takatsu, S. Onoda, S. Kittaka, A. Kasahara, Y. Kono, T. Sakakibara, Y. Kato, B. Fåk, J. Ollivier, J. W. Lynn, T. Taniguchi, M. Wakita, and H. Kadowaki, Quadrupole Order in the Frustrated Pyrochlore $Tb_{2+x}Ti_{2-x}O_{7+y}$, Phys. Rev. Lett. **116**, 217201 (2016).
[133] K. Fritsch, K. A. Ross, Y. Qiu, J. R. D. Copley, T. Guidi, R. I. Bewley, H. A. Dabkowska, and B. D. Gaulin, Antiferromagnetic spin ice correlations at $(1/2, 1/2, 1/2)$ in the ground state of the pyrochlore magnet $Tb_2Ti_2O_7$, Phys. Rev. B **87**, 094410 (2013).
[134] E. Kermarrec, D. D. Maharaj, J. Gaudet, K. Fritsch, D. Pomaranski, J. B. Kycia, Y. Qiu, J. R. D. Copley, M. M. P. Couchmann, A. O. R. Morningstar, H. A. Dabkowska, and B. D. Gaulin, Gapped and gapless short-range-ordered magnetic systems with $(1/2,1/2,1/2)$ wave vectors in the pyrochlore magnet $Tb_2Ti_2O_7$, Phys. Rev. B **92**, 245114 (2015).
[135] A. M. Hallas, J. G. Cheng, A. M. Arevalo-Lopez, H. J. Silverstein, Y. Su, P. M. Sarte, H. D. Zhou, E. S. Choi, J. P. Attfield, G. M. Luke, and C. R. Wiebe, Incipient Ferromagnetism in $Tb_2Ge_2O_7$: Application of Chemical Pressure to the Enigmatic Spin-Liquid Compound $Tb_2Ti_2O_7$, Phys. Rev. Lett. **113**, 267205 (2014).
[136] H. D. Zhou, C. R. Wiebe, J. A. Janik, L. Balicas, Y. J. Yo, Y. Qiu, J. R. D. Copley, and J. S. Gardner, Dynamic Spin Ice: $Pr_2Sn_2O_7$, Phys. Rev. Lett. **101**, 227204 (2008).
[137] K. Kimura, S. Nakatsuji, J.-J. Wen, C. Broholm, M. B. Stone, E. Nishibori, and H. Sawa, Quantum fluctuations in spin-ice-like $Pr_2Zr_2O_7$, Nat. Commun. **4**, 1934 (2013).
[138] R. Sibille, E. Lhotel, M. Ciomaga Hatnean, G. Balakrishnan, B. Fåk, N. Gauthier, T. Fennell, and M. Kenzelmann, Candidate quantum spin ice in the pyrochlore $Pr_2Hf_2O_7$, Phys. Rev. B **94**, 024436 (2016).
[139] Z. Y. Zhao, S. Calder, A. A. Aczel, M. A. McGuire, B. C. Sales, D. G. Mandrus, G. Chen, N. Trivedi, H. D. Zhou, and J.-Q. Yan, Fragile singlet ground state magnetism in pyrochlore osmates $R_2Os_2O_7$ ($R = Y$ and Ho), Phys. Rev. B **93**, 134428 (2016).
[140] M. Ciomaga Hatnean, M. R. Lees, and G. Balakrishnan, Growth of single-crystals of rare-earth zirconate pyrochlores, with ($Ln = La$, Nd, Sm and Gd) by the floating zone technique, J. Cryst. Growth **418**, 1 (2015).
[141] J. Lago, I. Zivkovic, B. Z. Malkin, J. Rodriguez Fernandez, P. Ghigna, P. Dalmas de Réotier, A. Yaouanc, and T. Rojo, $CdEr_2Se_4$: A New Erbium Spin Ice System in a Spinel Structure, Phys. Rev. Lett. **104**, 247203 (2010).
[142] Y. Okamoto, G. J. Nilsen, J. P. Attfield, and Z. Hiroi, Breathing Pyrochlore Lattice Realized in A-Site Ordered Spinel Oxides $LiGaCr_4O_8$ and $LiInCr_4O_8$, Phys. Rev. Lett. **110**, 097203 (2013).
[143] Y. Tanaka, M. Yoshida, M. Takigawa, Y. Okamoto, and Z. Hiroi, Novel Phase Transitions in the Breathing Pyrochlore Lattice: ^{7}Li-NMR on $LiInCr_4O_8$ and $LiGaCr_4O_8$, Phys. Rev. Lett. **113**, 227204 (2014).
[144] K. Kimura, S. Nakatsuji, and T. Kimura, Experimental realization of a quantum breathing pyrochlore antiferromagnet, Phys. Rev. B **90**, 060414(R) (2014).
[145] O. Benton and N. Shannon, Ground state selection and spin-liquid behaviour in the classical Heisenberg model on the breathing pyrochlore lattice, J. Phys. Soc. Jpn. **84**, 104710 (2015).
[146] K. A. Ross, J. W. Krizan, J. A. Rodriguez-Rivera, R. J. Cava, and C. L. Broholm, Static and dynamic XY-like short-range order in a frustrated magnet with exchange disorder, Phys. Rev. B **93**, 014433 (2016).
[147] L. Jaubert (unpublished).
[148] P. Fazekas, *Lecture Notes on Electron Correlation and Magnetism* (World Scientific, Singapore, 1999).
[149] M. Roger, J. H. Hetherington, and J. M. Delrieu, Magnetism in solid He-3, Rev. Mod. Phys. **55**, 1 (1983).
[150] R. H. Swendsen and J.-S. Wang, Replica Monte Carlo Simulation of Spin Glasses, Phys. Rev. Lett. **57**, 2607 (1986).
[151] C. J. Geyer, in *Computing Science and Statistics, Proceedings of the 23rd Symposium on the Interface*, edited by E. M. Keramidas (Interface Foundation, Fairfax Station, 1991), p. 156.
[152] M. Creutz, Overrelaxation and Monte Carlo simulation, Phys. Rev. D **36**, 515 (1987).
[153] G. Marsaglia, Choosing a point from the surface of a sphere, Ann. Math. Stat. **43**, 645 (1972).
[154] K. Kanki, D. Loison, and K. Schotte, Efficiency of the microcanonical over-relaxation algorithm for vector spins analyzing first and second order transitions, Eur. Phys. J. B **44**, 309 (2005).